MgB$_2$ hot-electron bolometer mixers for sub-mm wave astronomy

EVGENII NOVOSELOV

CHALMERS

MgB$_2$ hot-electron bolometer mixers for sub-mm wave astronomy

Evgenii Novoselov

Cover:
Left: HPCVD system deposition chamber. Center upper left: SEM image of spiral antenna coupled MgB$_2$ HEB. Center upper right: TEM image of 5 nm thick HPCVD grown MgB$_2$ film on SiC substrate. Center: Cold plate of LHe cryostat. Center lower left: SEM image of HPCVD grown MgB$_2$ film on Al$_2$O$_3$ substrate. Center lower right: 3D CAD image of MgB$_2$ HEB. Upper right: Chamber view during MgB$_2$ film deposition. Lower right: mixer block with Si lens. Designed by Niia Silaeva.

Per aspera ad astra

Abstract

Spectroscopy and photometry in the terahertz (THz) range of remote space objects allows for a study of their chemical composition, because this range covers rotational lines from simple molecules and electron transition lines from atoms and ions. Due to high spectral resolution, THz heterodyne receivers allow for studying dynamical properties of space objects manifested in doppler-shifted emission lines. Niobium nitride (NbN) hot-electron bolometer (HEB) mixers currently used at frequencies >1 THz, provide a typical gain bandwidth (GBW) of 3 GHz, and consequently, a noise bandwidth (NBW) of 4 GHz. This property severely limits the functionality of astronomical instruments. Moreover, the low critical temperature ($T_c = 8$–11 K) of NbN ultrathin films necessitates usage of liquid helium (LHe) for device cooling, which reduces lifetime of spaceborne missions.

In this thesis, a study of HEB mixers dedicated for sub-mm wave astronomy applications made from magnesium diboride (MgB_2) ultrathin films is presented. It is shown that MgB_2 HEB mixers reach a unique combination of low noise, wide noise bandwidth, and high operation temperature when 8 nm thick MgB_2 films ($T_c = 30$ K) are used. The hybrid physical chemical vapour deposition (HPCVD) technique allows for reproducible deposition of such thin films. The high T_c of MgB_2 (39 K), and consequently, short (3 ps) electron-phonon interaction time result in a GBW of up to 10 GHz and possibility of operation at temperatures >20 K, where compact cryocoolers are available. The GBW was observed to be almost independent on both bias voltage and bath temperature. A NBW of 11 GHz with a minimum double sideband (DSB) receiver noise temperature of 930 K is achieved at a 1.63 THz local oscillator (LO) and a 5 K bath temperature. At 15 K and 20 K, noise temperatures are 1100 K and 1600 K, respectively. From 0.69 THz to 1.63 THz noise increases by only 12%, and hence, low noise performance is expected even at higher frequencies. The minimum receiver noise temperature is achieved in a quite large range of both bias voltages (5–10 mV) and LO power. Compared to initial results, higher sensitivity and larger NBW are due to a larger HEB width (lower contact resistance), applied *in-situ* contact cleaning, and a smaller film thickness. The increase of noise temperature when operation temperature rises from 5 K to 20 K is due to a reduction of conversion gain by 2–4 dB caused be the reduced LO power absorbed in the HEB. The output noise of the HEB remains the same (120–220 K depending on the bias point).

Keywords: conversion gain, electron-phonon interaction, gain bandwidth, hot-electron bolometer, magnesium diboride, mixer, noise bandwidth, noise temperature, superconductor, thin film, THz detector.

List of Publications

Appended papers

This thesis is based on the following papers:

[A] S. Bevilacqua, **E. Novoselov**, S. Cherednichenko, H. Shibata, and Y. Tokura, "MgB$_2$ hot-electron bolometer mixers at terahertz frequencies," in *IEEE Transactions on Applied Superconductivity*, vol. 25, no. 3, June 2015, Art. no. 2301104.

[B] **E. Novoselov**, S. Bevilacqua, S. Cherednichenko, H. Shibata, and Y. Tokura, "Effect of the critical and operational temperatures on the sensitivity of MgB$_2$ HEB mixers," in *IEEE Transactions on Terahertz Science and Technology*, vol. 6, no. 2, pp. 238-244, March 2016.

[C] **E. Novoselov**, N. Zhang, and S. Cherednichenko, "Study of MgB$_2$ ultrathin films in submicron size bridges," in *IEEE Transactions on Applied Superconductivity*, vol. 27, no. 4, June 2017, Art. no. 7500605.

[D] **E. Novoselov**, N. Zhang, and S. Cherednichenko, "MgB$_2$ hot electron bolometer mixers for THz heterodyne instruments," in *Proceedings of SPIE*, vol. 9914, July 2016, Art. no. 99141N.

[E] **E. Novoselov**, N. Zhang, and S. Cherednichenko, "Wideband THz HEB mixers using HPCVD MgB$_2$ thin films," in Proceedings of *41st International Conference on Infrared, Millimeter and Terahertz Waves*, Copenhagen, Denmark, 25-30 September 2016.

[F] **E. Novoselov** and S. Cherednichenko, "Broadband MgB$_2$ hot-electron bolometer THz mixers operating up to 20 K," in *IEEE Transactions on Applied Superconductivity*, vol. 27, no. 4, June 2017, Art. no. 2300504.

[G] **E. Novoselov** and S. Cherednichenko, "Low noise terahertz MgB$_2$ hot-electron bolometer mixers with an 11 GHz bandwidth," in *Applied Physics Letters*, vol. 110, no. 3, January 2017, Art. no. 032601.

[H] **E. Novoselov** and S. Cherednichenko, "Gain and noise in THz MgB$_2$ hot-electron bolometer mixers with a 30 K critical temperature," submitted to *IEEE Transactions on Terahertz Science and Technology*, April 2017.

Other papers and publications

The following papers and publications are not appended to the thesis, either due to contents overlapping of that of appended papers, or due to contents not related to the thesis.

[a] **E. Novoselov**, N. Zhang, and S. Cherednichenko, "MgB$_2$ HEB mixers at operation temperatures above liquid helium temperature," in Proceedings of 27th *International Symposium on Space Terahertz Technology*, Nanjing, China, 12-15 April 2016.

[b] S. Bevilacqua, **E. Novoselov**, S. Cherednichenko, H. Shibata, and Y. Tokura, "Wideband MgB$_2$ hot-electron bolometer mixers: IF impedance characterisation and modeling," in *IEEE Transactions on Applied Superconductivity*, vol. 26, no. 3, April 2016, Art. no. 2300105.

[c] **E. Novoselov**, S. Bevilacqua, S. Cherednichenko, H. Shibata, and Y. Tokura, "THz low noise mixers for sub-mm astronomy," in Proceedings of 3rd *Swedish Microwave Days*, Linköping, Sweden, 15-16 March 2016, p. 50.

[d] S. Bevilacqua, **E. Novoselov**, S. Cherednichenko, H. Shibata, and Y. Tokura, "Characterisation and Modeling of MgB$_2$ HEBs IF impedance," in Proceedings of 3rd *Swedish Microwave Days*, Linköping, Sweden, 15-16 March 2016, p. 55.

[e] **E. Novoselov**, S. Bevilacqua, S. Cherednichenko, H. Shibata, and Y. Tokura, "Noise measurements of the low T$_c$ MgB$_2$ HEB mixer at 1.6 THz and 2.6 THz," in Proceedings of 26th *International Symposium on Space Terahertz Technology*, Cambridge, USA, 16-18 March 2015, Art. no. P-31.

[f] S. Cherednichenko, **E. Novoselov**, S. Bevilacqua, H. Shibata, and Y. Tokura, "Study of MgB$_2$ HEB mixers vs the LO frequency and the bath temperature," in Proceedings of 26th *International Symposium on Space Terahertz Technology*, Cambridge, USA, 16-18 March 2015, Art. no. M2-1.

[g] S. Cherednichenko, S. Bevilacqua, and **E. Novoselov**, "THz hot-electron bolometer mixers," in Proceedings of 39th *International Conference on Infrared, Millimeter and Terahertz Waves*, Tucson, USA, 14-19 September 2014.

[h] N. Balbekin, **E. Novoselov**, P. Pavlov, V. Bespalov, and N. Petrov, "Nondestructive monitoring of aircraft composites using terahertz radiation," in *Proceedings of SPIE*, vol. 9448, March 2015, Art. no. 94482D.

[i] V.G. Bespalov, A.A. Gorodetskii, Y.V. Grachev, S.A. Kozlov, and **E.V. Novoselov**, "Pulse terahertz reflectometer," in *Scientific and Technical Journal of Information Technologies, Mechanics, and Optics*, vol. 71, no. 1, pp. 19-23, January-February 2011, (in russian).

[j] **E.V. Novoselov** and V.G. Bespalov, "Design of the tunable mirror objective for pulse terahertz reflectometer spectrograph-intravisor," in *Scientific and Technical Journal of Information Technologies, Mechanics, and Optics*, vol. 70, no. 6, pp. 6-9, November-December 2010, (in russian).

[k] A.A. Andreev, V.G. Bespalov, A.A. Gorodetskii, S.A. Kozlov, V.N. Krylov, G.V. Lukomskii, **E.V. Novoselov**, N.V. Petrov, S.E. Putilin, and S.A. Stumpf, "Generation of ultrabroadband terahertz radiation under optical breakdown of air by two femtosecond pulses of different frequencies," in *Optics and Spectroscopy*, vol. 107, no. 4, pp. 538-544, October 2009.

Notations and abbreviations

Notations

2Δ	Superconducting energy gap
$2\Delta_{dirty}$	Dirty limit superconducting energy gap
$2\Delta_{\pi}$	Superconducting energy π-gap
$2\Delta_{\sigma}$	Superconducting energy σ-gap
$\hbar$	Dirac constant
α	Thermometer local sensitivity
β	Acoustic phonon transmission coefficient
γ	Electron specific heat coefficient
ΔT	Temperature change
ΔU_0	DC voltage response
ϵ	Permittivity
λ	Wavelength
λ_L	Penetration depth
μ_0	Permeability of vacuum
ξ	Coherence length
ρ_{295K}	Room temperature resistivity
θ	Electron temperature
τ	Bolometer time constant
τ_{θ}	Electron temperature relaxation time
τ_{θ}^*	Modified electron temperature relaxation time
τ_e	Effective bolometer time constant
τ_{ep}	Electron phonon interaction time
τ_{esc}	Phonon escape time
τ_{mix}	Mixer time constant
τ_{pe}	Phonon electron interaction time
Φ_0	Flux quantum
χ	Power exchange function
ω	Angular frequency
ω_i	Imaginary frequency
ω_{IF}	Intermediate angular frequency
ω_{LO}	Local oscillator angular frequency
ω_0	Response rate
ω_s	Signal angular frequency
B	Bandwidth

C	Heat capacitance
C'	Dimensionless self heating parameter
C_0	Self heating parameter
c_e	Electron specific heat
c_p	Phonon specific heat
d	Film thickness
f_g	Gain bandwidth frequency
f_{IF}	Intermediate frequency
f_n	Noise bandwidth frequency
G	Thermal conductance
G_d	Dynamic thermal conductance
G_e	Effective thermal conductance
G_{IF}	IF chain gain
G_m	Mixer conversion gain
G_{tot}	Receiver conversion gain
I	Current
I_0	Bias current
I_c	Critical current
J_c	Critical current density
J_d	Depairing current density
k_B	Boltzmann constant
L	Bolometer length
L_{opt}	Optical losses
n	Atomic density
N_{out}	Output noise power
P	Power
P_{cold}	Cold load intermediate frequency output power
P_{hot}	Hot load intermediate frequency output power
P_{IF}	Intermediate frequency signal power
P_{LO}	Local oscillator power
P_{out}	Intermediate frequency output power
P_s	Signal power
R	Resistance
R_0	Bolometer resistance
R_L	Load resistance
R_{ons}	Onset resistance
R_S	Sheet resistance
R_t	Thermometer resistance
R_v	Voltage responsivity
R_{295K}	Room temperature resistance
RRR	Residual resistance ratio
r	Etching rate
S/N	Signal to noise ratio
T	Temperature
t	Time
T_b	Bolometer temperature
T_{bath}	Reservoir temperature
T_c	Critical temperature
T_D	Debye temperature
T_{FL}	Thermal fluctuation noise

T_J	Johnson noise
T_{IF}	IF chain noise temperature
T_m	Mixer noise temperature
T_{opt}	Equivalent noise temperature of optical components
T_{out}	Mixer output noise temperature
T_p	Phonon temperature
T_{rec}	Receiver noise temperature
T_{REF}	Equivalent noise temperature at the reference state
u	Speed of sound
U	Voltage
U_0	Bias voltage
U_{LO}	Voltage amplitude of the local oscillator
U_s	Voltage amplitude of the signal
W	Bolometer width
Z	Bolometer impedance

Abbreviations

2-T	Two-temperature
3D	Three-dimensional
AFM	Atomic force microscope
Al_2O_3	Sapphire
Ar	Argon
Au	Gold
B	Boron
B_2H_6	Diborane
BCS	Bardeen-Cooper-Schrieffer
BH_3	Borane
BWO	Backward-wave oscillator
CAD	Computer-aided design
CH_2F_2	Difluoromethane
CH_2O_2	Formic acid
DC	Direct current
DSB	Double sideband
FIR	Far Infrared
GaAs	Gallium arsenide
GBW	Gain bandwidth
GHz	10^9 Hz
H_2	Hydrogen
HCl	Hydrogen chloride
HDPE	High-density polyethylene
HEB	Hot electron bolometer
HEMT	High-electron-mobility transistor
HPCVD	Hybrid physical chemical vapour deposition
IF	Intermediate frequency
IR	Infrared
InP	Indium phosphide
InSb	Indium antimonide
I-V	Current versus voltage
LHe	Liquid helium
LNA	Low noise amplifier
LO	Local oscillator
LSB	Lower sideband
MBE	Molecular beam epitaxy
Mg	Magnesium
MgO	Magnesium oxide
MgB_2	Magnesium diboride
N_2	Nitrogen
NbN	Niobium nitride
NbTiN	Niobium titanium nitride
NBW	Noise bandwidth
O_2	Oxygen
PLD	Pulsed laser deposition
RF	Radio frequency
R-T	Resistance versus temperature
SEM	Scanning electron microscope

SD	Schottky diode
Si	Silicon
SiC	Silicon carbide
SiN_x	Silicon nitride
SiO_2	Silicon dioxide
SIS	Superconductor-insulator-superconductor tunnel junction
SSPD	Superconducting single-photon detector
SQUID	Superconducting quantum interference device
TEM	Transmission electron microscope
THz	10^{12} Hz
Ti	Titamium
USB	Upper sideband
UV	Ultraviolet
XRD	X-ray diffractometer
YIG	Yttrium iron garnet

Contents

Chapter 1

Introduction

The 0.1–10 THz part of electromagnetic spectrum between the microwave and infrared (IR) bands is referred to as terahertz (THz) range [1, 2]. Despite technological difficulties (the THz gap), this region has proven to be of great interest for medical [3] and security [4] sensing, communication [5], and Earth and Space science [6]. The THz range covers rotational lines from simple molecules and the ground state fine-structure emission lines from atoms and ions [7]. This is of great interest for astronomy [8], because of the possibility to study physics, dynamics, and chemistry of galaxies, star-formation regions, the interstellar medium, comets, asteroids, outer planet atmospheres, etc.

In order to resolve fine structure of molecular emission lines, heterodyne receivers with a high spectral resolution ($\lambda/\Delta\lambda \approx 10^6$–$10^7$) are required [9,10]. For such applications several types of devices have been used as a mixer element for a heterodyne receiver, e.g. Schottky diodes (SD) [11], superconductor-insulator-superconductor tunnel junctions (SIS) [12], hot-electron bolometers (HEB) [13]. At frequencies above 1 THz HEBs are devices of choice (see Figure 1.1). Superconducting HEB mixers were introduced in Ref. [14] after the discovery of the electron-heating effect in superconducting films [15]. Until recently, the state-of-the-art phonon-cooled HEBs were fabricated using niobium nitride (NbN) and niobium titanium nitride (NbTiN) ultrathin films. HEB mixers are highly sensitive THz detectors providing a low receiver noise temperature from 300 K at 1.3 THz local oscillator (LO) [16] to 1150 K at 5.25 THz LO [17]. They were employed in many receivers for astronomical and atmospheric science observation programs launched in recent years, e.g. RLT [18], APEX [19, 20], the Herschel Space Observatory [21, 22], TELIS [23, 24], STO/STO-2 [25–29], and SOFIA [30–32]. They were also chosen for a number of current programs and programs under development, such as ASTE [33,34], DATE5 [16,35], SMILES-2 [36,37], GUSSTO [38], Millimetron [39,40], FIRSPEX [41], and OST [42].

NbN HEB mixers typically have a gain bandwidth (GBW) of ≈ 3 GHz (NbTiN HEB mixers have even smaller GBW of ≈ 2 GHz). As a result, the receiver noise temperature increases towards higher intermediate frequencies (IF) and doubles already at an IF of ≈ 4 GHz. Therefore, the number of scientific tasks in sub-mm wave astronomy which can be performed with HEB mixers is limited [43].
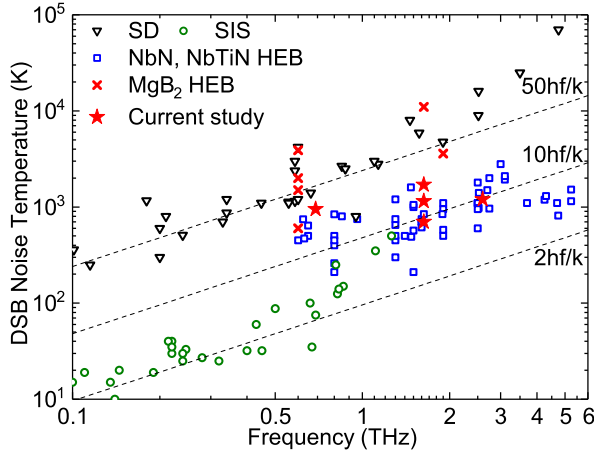
Fig. 1.1: State-of-the-art noise temperature versus LO frequency for different THz mixer technologies: SD [44–69]; SIS [70–90]; NbN, NbTiN HEB [16, 17, 19, 31–35, 91–121]; and MgB_2 HEB [122–126].

Figure 1.2(a) demonstrates a mapping of Galaxy M82 by the HIFI instrument of the Hershel Space Observatory [43]. The high spectral resolution and sensitivity of the HIFI instrument allowed for observation of very weak ($<5\,$K) frequency-shifted emissions from the two arms of the galaxy. Measured spectra at $0.57\,$THz (CO line) and $1.9\,$THz (CII line) are shown in Figure 1.2(b). One arm of the galaxy is moving towards us and the other from us, which results in the existence of two main velocity components: the blue-shifted and the red-shifted emission lobes, which are clearly seen on the left spectrum in Figure 1.2(b). The large difference between relative to the Earth velocities of the Galaxy M82 arms of $400\,$km/s resulted in the rather broad $1.9\,$THz CII spectral line ($2.5\,$GHz). The nominal IF bandwidth of the used receivers ($2.4\,$GHz) was just enough to fit this spectral line, but it did not allow to get the baseline of the signal properly. At the same time, the observation at higher frequencies might be interesting due to the smaller beam size. For example, the beam at $1.9\,$THz was almost four times smaller than at $0.57\,$THz (red bars on Figure 1.2(a)). Moreover, emission lines for some molecules exist only at higher frequencies. At $4.7\,$THz such velocity difference will result in $\approx 6\,$GHz broad lines, which is well above a typical NbN HEB mixer bandwidth. On the other hand, a superconducting critical temperature (T_c) of 8–11 K limits NbN HEB mixer operation to liquid helium (LHe) temperatures ($<6\,$K). The lack of 4K cryocoolers qualified for space application necessitates of LHe utilization that leads to very limited spaceborne mission lifetimes. In order to improve the functionality of HEB mixers, other superconducting materials must be used, e.g. magnesium diboride (MgB_2).

The discovery of superconductivity in MgB_2 [127] with the highest T_c among intermetallic compounds (bulk $T_c = 39\,$K) and fast progress in thin film deposition techniques [128–130] opened new opportunities in HEB development. For the first time heterodyne mixing using a MgB_2 HEB with a T_c of $22\,$K made from a molecular beam epitaxy (MBE) grown [130] $20\,$nm thick
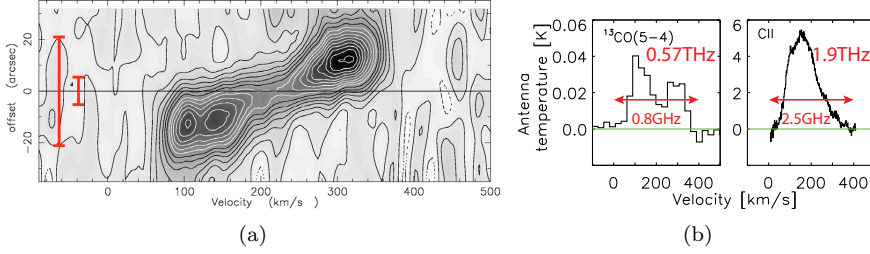
Fig. 1.2: Observation of Galaxy M82 by the Hershel Space Observatory (a) Position-velocity diagram of the Nucleus of M82. The two red bars show the largest (44" at 0.57 THz) and the smallest (12" at 1.9 THz) beams in observations. (b) Observed spectra of Galaxy M82: CO line at 0.57 THz by SIS mixers (left) and CII line at 1.9 THz by HEB mixers (right). The same velocity range corresponds to about three times wider signal bandwidth at 1.9 THz than at 0.57 THz. Illustrations from Ref. [43].

film on a silicon (Si) substrate was reported in 2007 [122]. The device had a rather high receiver noise temperature of 11 000 K at 1.6 THz but the GBW was already 2.3 GHz at 0.6 THz despite such a thick film.

In subsequent works by *Bevilacqua et al.* [123, 124, 131] the GBW of MgB_2 HEB mixers made from MBE grown films on c-cut sapphire (Al_2O_3) substrates was studied the most. The large dimensions of initial HEBs (100–500 μm^2) and consequently high LO power requirements forced the utilization of low frequency (0.35–0.6 THz) sources providing more output power for device characterisation. Therefore, a large superconducting energy gap necessitated the use of high bath temperatures of up to few degrees below the T_c in order to make the gap smaller than the energy of photons. The maximum GBW of 3.4 GHz was achieved with a 10 nm thick device with a T_c of 14 K [124]. And the possibility to increase the GBW up to 8–10 GHz using 3–5 nm thick MgB_2 HEB mixers with a T_c >30 K was suggested [123]. Fabrication of smaller devices (3–42 μm^2) that requires less LO power allowed for the study of MgB_2 HEB mixers sensitivity in a wide range of bath temperatures [123, 124]. The minimum noise temperature of 800 K at 0.6 THz was demonstrated with a device with a T_c of 8.5 K [123]. A HEB mixer with a T_c of 15 K had a higher noise temperature of 1500 K, but it was also shown that the noise temperature remains constant at bath temperatures ranging from 4.2 K up to 10.5 K [124]. The need for fabrication of submicron size MgB_2 HEB mixers for operation at higher LO frequencies was highlighted [124].

In parallel work on MgB_2 HEB mixers by *Cunnane et al.* [125, 126, 132] devices made from hybrid physical-chemical vapour deposition (HPCVD) grown [133] films on silicon carbide (SiC) substrates were studied. A GBW greater than 8 GHz was demonstrated with a 15 nm thick HEB mixer with a T_c of 33 K. The best noise performance achieved for HEB mixers made from HPCVD grown films was 2000 K at 0.6 THz [126]. This device had a noise bandwidth (NBW) of 6.5 GHz and the noise temperature had a minimal dependance on a bath temperature up to 20 K. At 1.9 THz, the noise temperature of such device increased to 3600 K.

The research presented in this thesis addresses the problem of limited bandwidth and low operation temperature of THz HEB mixers. The increase of bandwidth and operation temperature is required without sacrificing the low noise performance. The low noise temperature and the large bandwidth were shown for MgB_2 HEB mixers separately, but devices simultaneously demonstrating both of these features were not achieved. **The achievement of sensitivity and bandwidth superior to NbN HEB mixers and operation at bath temperatures above the LHe temperature by fabrication of submicron size MgB_2 HEB mixers was the main goal of this work.**

- The performance of HEB mixer is mainly affected by the quality of superconducting thin film used for device fabrication. **The primary goal** was to develop the process for growth of MgB_2 ultrathin (5-10 nm thick) films with a T_c above 30 K, low roughness, high homogeneity, and applicable for fabrication of submicron size structures.

- **The second goal** was the development of HEB fabrication process capable for submicron size device fabrication, preserving superconducting film quality, and providing a high yield and a high robustness.

- **Third,** the fabricated HEB mixers should be tested at THz frequencies. The dependance of their intrinsic parameters on LO frequency and power, a T_c, and a bath temperature should be studied in order to find the way for further MgB_2 HEB mixers improvement and their optimization for specific tasks.

The thesis is structured in 6 chapters. **Chapter 2** contains an overview of: bolometer detection principles, heterodyne mixing, HEB modeling, and design of heterodyne receivers utilizing HEB mixers. **Chapter 3** describes the HPCVD technique used for MgB_2 ultrathin film deposition and the study of achieved films. The electron beam (e-beam) and ultraviolet (UV) lithography HEB fabrication processes are presented in **Chapter 4**. **Chapter 5** provides the detailed description of the measurement setup and techniques used for device characterization at THz frequencies. The summary of THz characterization results is given in **Chapter 6**. Finally, **Chapter 7** summarises the results of this work and provides the future outlook.

Chapter 2

Background

This chapter provides an overview of: bolometer operation principles and main characteristics which determine the bolometer performance. Total power and frequency selective detection regimes of bolometer operation are described and discussed. The lumped HEB mixer model and the two-temperature (2-T) model of electron-phonon relaxation are presented as well as an overview of heterodyne receivers designs.

2.1 Bolometric receiver

A simple bolometer consists of three parts. Figure 2.1(a) represents these parts: an absorber where an incident power is absorbed and thermalized; a perfectly coupled thermometer which measures changes of the absorber temperature; and a weak thermal link connecting the absorber and a heat sink to return the absorber into the initial state in an absence of incident power. The absorber is characterised by a heat capacity C, the thermal link by a thermal conductivity G and the heat sink by a temperature T_{bath}.

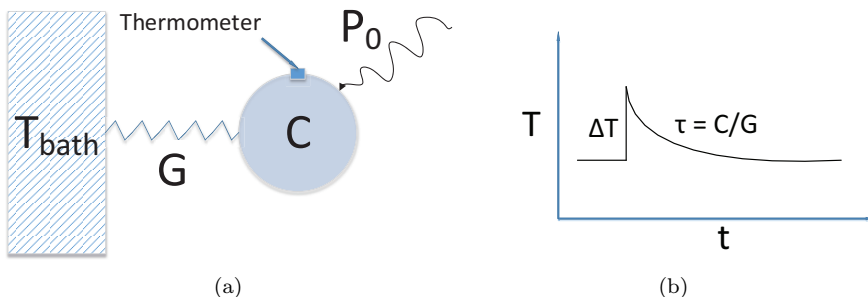

(a)   (b)

Fig. 2.1: (a) Schematic of simple bolometer consisting of an absorber with a heat C, a thermometer and a weak link with a thermal conductivity G connecting the absorber to a heat sink with a temperature T_{bath}. (b) Schematic representation of bolometer working principle. An incoming radiation with a total power P_0 increases bolometer temperature by $\Delta T = P_0/G$. After the incoming radiation is removed the bolometer temperature decays back with a time constant $\tau = C/G$.

Fig. 2.2: Schematic of total power detection.

This device can be used to measure a steady power input P_0 which gives a temperature increase of $\Delta T = P_0/G$ with an assumption of uniform heating of the bolometer. In case of a variable power $P(t)$ the dynamics of the bolometer temperature T_b can be described by a heat balance equation:

$$C\frac{dT_b}{dt} + G(T_b - T_{bath}) = P(t) \qquad (2.1)$$

When the bolometer is no longer irradiated, i.e. $P(t) = 0$, its temperature relaxes back to T_{bath}. Then Equation 2.1 can be solved as:

$$T_b(t) = T_{bath} + \Delta T e^{-\frac{t}{\tau}} \qquad (2.2)$$

where $\tau = C/G$ is a bolometer time constant.

2.1.1   Direct detection

Being irradiated by the input power P_0 the receiver produces a direct current (DC) voltage response ΔU_0 which is proportional to the power of incoming radiation (see Figure 2.2). In this case the receiver measures the total power of incoming radiation independently on frequency in the whole band where the receiver is sensitive. The total power detector is characterised by a voltage responsivity:

$$R_v = \frac{\Delta U_0}{P_0} \qquad (2.3)$$

An electrical resistance thermometer (thermistor) (see Figure 2.3) might be used to measure the temperature of bolometer. In the electrical resistance thermometer a change in temperature is converted into a change in resistance R_t, which is converted into voltage changes with a readout current. The temperature of such a bolometer irradiated by an incident signal (ω_s) with a power $P(t) = P_0 + P_1 e^{i\omega_s t}$ changes as $T_b = T_0 + T_1 e^{i\omega_s t}$. The voltage responsivity of bolometer with a thermistor biased with a constant current I_0 is [134]:

$$R_v = \frac{I_0 \frac{dR_t}{dT}}{G_d - I_0^2(\frac{dR_t}{dT}) + i\omega_s C} \qquad (2.4)$$

where $G_d = dP/dT$ is a dynamic thermal conductance at the temperature T_0. Equation 2.4 is valid if the load resistance $R_L \gg R_t$. The bolometer responsivity is influenced by the thermal feedback which can be expressed as the effective thermal conductance $G_e = G_d - I^2(dR_t/dT)$. The thermal feedback also modifies the measured bolometer time constant $\tau_e = C/G_e$. It is
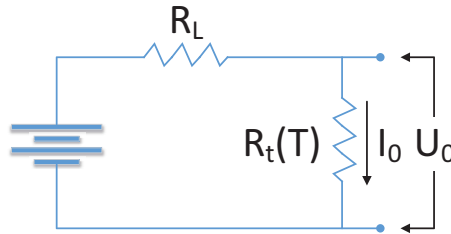
Fig. 2.3: Bias circuit of electrical resistance thermometer. I_0 is the bias current, U_0 the bias voltage, R_L the load resistance, $R_t(T)$ the temperature dependent thermometer resistance.
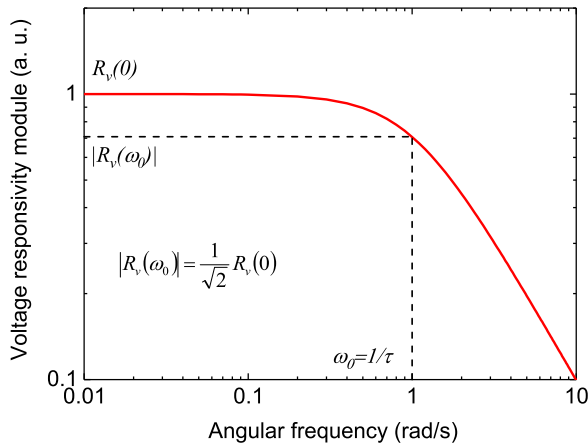

Fig. 2.4: Voltage responsivity versus frequency.

convenient to define a local sensitivity for the thermometer $\alpha = R_t^{-1}(dR_t/dT)$ evaluated at T_0. With new definitions the voltage responsivity becomes:

$$R_v = \frac{I_0 R_t \alpha}{G_e(1 + i\omega_s \tau_e)} \tag{2.5}$$

The module of voltage responsivity:

$$|R_v| = \frac{R_v(0)}{\sqrt{1 + \omega_s^2 \tau_e^2}} \tag{2.6}$$

where $R_v(0) = I_0 R_t \alpha / G_e$ is the zero frequency responsivity, is plotted in Figure 2.4. The bolometer time constant τ_e determines the bolometer response rate ($\omega_0 = 1/\tau_e$).

The absorber and thermistor could be combined in one structure as in case of microbolomter which is a thin film resistor with a high temperature coefficient of resistance. The microbolometers were realized in different geometries in order to reduce a thermal coupling of the microbolometer to the heat sink, e.g. placing on a thin membrane [135] or making free-standing bridge bolome-
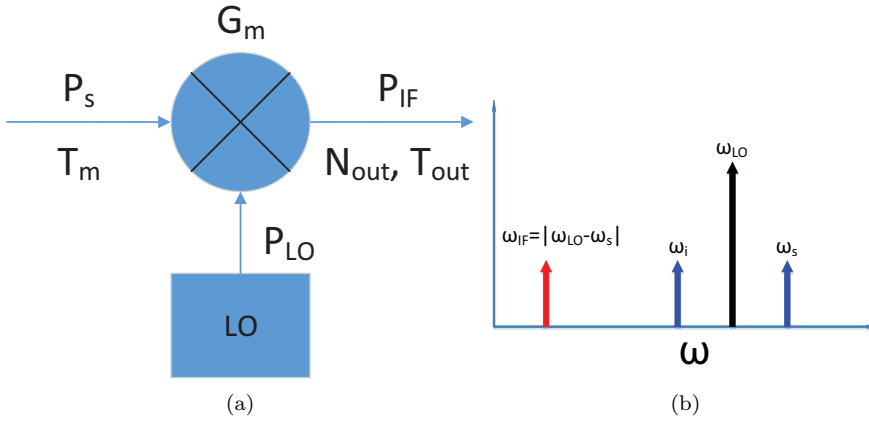
Fig. 2.5: (a) Schematic of down-converting mixer. (b) Schematic of down-conversion in a frequency domain.

ters [136]. A lower thermal coupling results in a higher voltage responsivity, but simultaneously the response rate is decreasing.

The total power detector may be a very efficient radiation detector but it does not provide any spectral information. In order to perform spectrometry a narrow band-pass filter is placed at the receiver input, e.g. an interferometer. However, the size of interferometer scales with its resolution. So the maximum practical spectral resolution which might be achieved in THz range using interferometer is $\approx 10^3$.

2.1.2   Frequency mixing

Heterodyne receivers have some advantages over direct detection receivers. First, both amplitude and phase information are preserved. Second, a high frequency narrow band-pass filter is not required at the receiver input in order to achieve a high spectral resolution. In heterodyne receivers a down-converting mixer mixes an incident signal (ω_s), which in a general case might be represented as a sum of frequency components, with a monochromatic radiation (ω_{LO}) from an LO (see Fig. 2.5). The total radio frequency (RF) voltage U(t) across the mixer is:

$$U(t) = U_s(cos(\omega_s t)) + U_{LO}(cos(\omega_{LO}t)) \tag{2.7}$$

where U_s and U_{LO} are amplitudes of signal and LO voltages, respectively. Bolometers with a thermistor could be used as mixing elements for heterodyne receivers. The total power dissipated in the bolometer is:

$$P(t) = \frac{U(t)^2}{2R_t} \tag{2.8}$$

Inserting Equation 2.7 into 2.8 and taking into account that the bolometer temperature can not follow high frequency terms $2\omega_s$, $2\omega_{LO}$ and $\omega_s + \omega_{LO}$ the

total dissipated power becomes:

$$P(t) = P_s + P_{LO} + 2\sqrt{P_s P_{LO}} cos(\omega_{IF} t) \qquad (2.9)$$

where $P_s = U_s^2/2R_t$, $P_{LO} = U_{LO}^2/2R_t$, and $\omega_{IF} = |\omega_s - \omega_{LO}|$ which should be less then $1/\tau_e$. As it follows from Equation 2.9 the IF output P_{IF} at a frequency ω_{IF} can be produced by either an Upper Sideband (USB) $\omega_s = \omega_{LO} + \omega_{IF}$ or a Lower Sideband (LSB) $\omega_i = \omega_{LO} - \omega_{IF}$ (see Figure 2.5(b)). Mixers sensitive to both USB and LSB are called Double Sideband (DSB). The performance of mixer is characterised by a mixer conversion gain:

$$G_m = \frac{P_{IF}}{P_s} \qquad (2.10)$$

Another important figure of merit for the mixer is noise. The mixer itself produces noise at the output with a power N_{out}. This noise might be represented with the output noise temperature T_{out} using the Johnson-Nyquist equation:

$$T_{out} = \frac{N_{out}}{k_B B} \qquad (2.11)$$

where k_B is the Boltzmann constant and B a bandwidth. Using the mixer conversion gain the output noise temperature T_{out} might be referred to the mixer input in case of DSB mixer as:

$$T_m = \frac{T_{out}}{2G_m} \qquad (2.12)$$

A factor "2" in Equation 2.12 comes from a DSB operation of HEB mixer and an assumption that a sideband ratio is one.

2.2 Superconducting HEB mixers

The term "hot electrons" is used to describe a non-equilibrium state of electrons inside the bolometer, i.e. an effective elevation of electron temperature. The first HEB mixer was realised using a doped semiconductor indium antimonide (InSb) [134]. Despite a good sensitivity, devices based on InSb had quite small bandwidth due to the time constants of the order of microseconds [137]. After the discovery of electron-heating effect in superconducting films [15] superconductors emerged as a material for HEB mixers [14]. The resistance of a superconductor is strongly affected by the electron temperature in a region close to a T_c, which explains the HEBs' high sensitivity. HEB mixers made from NbN films were successfully implemented [138] allowing for the achievement of a typical bandwidth of up to 4 GHz [139].

2.2.1 Photoresponse of phonon-cooled HEB mixers

Two types of superconducting HEB mixers differing by the dominating mechanism of electron cooling were reported: phonon-cooled [14] and diffusion-cooled [140]. In a phonon-cooled HEB a thin superconducting film deposited on a substrate acts as an absorber. The film cools down through the substrate,
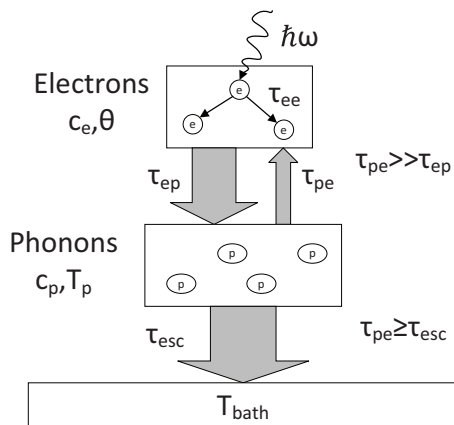
Fig. 2.6: Energy transfer and intrinsic relaxation times in a phonon-cooled HEB [141].

which plays a role of a heat sink. A thermal link between them is a thermal boundary resistance. The superconducting film acts also as a resistive thermometer. The thermalisation scheme of such a device is depicted in Figure 2.6.

In order to operate as a receiver the HEB is cooled down below its T_c where a thermal coupling between phonons and electrons is week and the electron-electron interaction is strong. The interaction time between electrons τ_{ee} is shorter than other characteristic time constants, which makes possible to present the HEB as a 2-T system. The first (electron) subsystem consists of quasiparticles and has a temperature θ and a specific heat c_e. The second (phonon) subsystem is formed by phonons in a superconducting film and has a temperature T_p and a specific heat c_p. The heat exchange between electron and phonon subsystems is done with characteristic time constants τ_{ep} and τ_{pe}. In an equilibrium state this interaction times relates as $\tau_{pe} = \tau_{ep}c_p/c_e$ and in order to achieve electron cooling τ_{ep} should be less than τ_{pe}. Then instead of one heat balance equation 2.1 a system of heat balance equations might be written as [142]:

$$c_e \frac{d\theta}{dt} = P(t) - c_e \frac{\theta - T_p}{\tau_{ep}} \tag{2.13}$$

$$c_p \frac{dT_p}{dt} = c_e \frac{\theta - T_p}{\tau_{ep}} - c_p \frac{T_p - T_{bath}}{\tau_{esc}} \tag{2.14}$$

where τ_{esc} is an escape time of phonons from the superconducting film into the substrate:

$$\tau_{esc} = \frac{4d}{\beta u} \tag{2.15}$$

where d is a superconductor thickness, u a speed of sound and β an acoustic phonon transmission coefficient. The phonon escape time τ_{esc} should be less then the electron-phonon interaction time τ_{ep} to prevent heat accumulation in the phonon subsystem. The reverse energy flow carried by the phonons from the substrate into the superconductor is neglected.

Close to the T_c the electron specific heat as a function of the electron temperature is:

$$c_e(\theta) = \gamma\theta \tag{2.16}$$

where γ is the electron specific heat coefficient. The phonon specific heat at an arbitrary phonon temperature in the Debye approximation is given by [143]:

$$c_p(T_p) = 9nk_B \left(\frac{T_p}{T_D}\right)^3 \int_0^{\frac{T_D}{T_p}} \frac{e^x x^4}{(e^x - 1)^2} dx \tag{2.17}$$

where n is an atomic density and T_D the Debye temperature. The phonon temperature T_p is $\approx 0.9 \times \theta$ and could be estimated from the heat balance equations (Equations 2.13 and 2.14) [144].

2.2.2 The lumped element HEB model

In order to analyse the HEB behavior, lumped element model previously developed for NbN HEBs [14] can be used. The model assumes that the electron temperature along the superconducting film is uniform and RF radiation and both DC power have the same effect on the HEB. However, this assumption was not completely true and development of the hot-spot models [145–147] was required. In the hot-spot models the electron temperature profile along the superconducting film was taken into account. Compared to the standard model, modifications of the heat balance equation were done. This modifications allowed for the correct modeling of HEB noise and current versus voltage (I-V) curves, while the standard model requires experimental curves for modeling.

2.2.2.1 Conversion gain

Using standard lumped element formalism expression for the HEB voltage responsivity might be written as [148]:

$$R_v(f_{IF}) = \frac{R_L I_0}{R_L + R_0} \frac{\frac{C_0}{\chi}}{1 - C_0 I_0^2 \frac{R_L - R_0}{R_L + R_0}} \frac{1}{1 + i\frac{f_{IF}}{f_g}} = R_v(0) \frac{1}{1 + i\frac{f_{IF}}{f_g}} \tag{2.18}$$

where R_0 is the HEB DC resistance at the bias point, f_g the HEB 3 dB gain roll-off frequency (GBW), and $C_0 = dR/dP$ (P is a sum of dissipated DC and LO powers). An assumption that the impedance of a HEB at the high-frequency limit $Z(\infty)$ is equal to R_0 was done. For Nb HEBs it was shown that a real part of $Z(f_{IF})$ goes to R_0 at frequencies $>1\,\text{GHz}$ [149]. For MgB$_2$ HEBs a similar investigation on the IF impedance was performed recently [150]. It was shown that a real part of HEB impedance approaches differential resistance dU/dI at low frequencies and R_0 at higher frequencies similar to NbN HEBs [151]. A power exchange function χ is introduced in a similar way as in [152]. It is defined as a ratio of the RF and DC power changes required to keep the device resistance constant. As a general rule a HEB resistance is more sensitive to a DC power then to an RF power, which results in conversion functions larger than one. It was demonstrated that χ typically takes values from 3 to 1 decaying moving to higher biases [146, 151].

The mixer conversion gain is given by [148]:

$$G_m(f_{IF}) = \frac{2P_{LO}R_v^2(f_{IF})}{R_L} \tag{2.19}$$

where P_{LO} is an absorbed LO power.

Inserting Equation 2.18 into 2.20 the mixer conversion gain predicted by the standard model is calculated as:

$$G_m(f_{IF}) = \frac{2P_{LO}R_LI_0^2}{(R_L+R_0)^2} \frac{(\frac{C_0}{\chi})^2}{(1-C_0I_0^2\frac{R_L-R_0}{R_L+R_0})^2} \frac{1}{1+(\frac{f_{IF}}{f_g})^2} = G_m(0)\frac{1}{1+(\frac{f_{IF}}{f_g})^2} \tag{2.20}$$

where $G_m(0)$ is a mixer conversion gain at zero IF.

Another assumption made in this theory is that the resistance of HEB depends on the electron temperature. Because the temperature is linearly proportional to the dissipated power, then $R = C_0P$. After some mathematical derivations it was shown that [149]:

$$C_0 = \frac{1}{I_0^2}\frac{\frac{dU}{dI}-R_0}{\frac{dU}{dI}+R_0} = \frac{C'}{I_0^2} \tag{2.21}$$

where C' is a dimensionless self-heating parameter.

2.2.2.2 Noise temperature

The main noise sources in a HEB mixer are Johnson noise and thermal fluctuation noise [14]. Output noise temperatures T_J and T_{FL} produced by each noise component might be calculated [153] according to the Mather's nonequilibrium theory of bolometer detector [154] as:

$$T_J(f_{IF}) = \frac{4R_LR_0\theta}{(R_L+R_0)^2(1-C_0I_0^2\frac{R_L-R_0}{R_L+R_0})^2} \tag{2.22}$$

$$T_{FL}(f_{IF}) = \frac{I_0^2R_L(\frac{\partial R}{\partial \theta})^2\frac{4\theta^2}{c_eV}\tau_\theta}{(R_L+R_0)^2(1-C_0I_0^2\frac{R_L-R_0}{R_L+R_0})^2}\frac{1}{1+(2\pi f_{IF}\tau_\theta^*)^2} \tag{2.23}$$

where V is the HEB volume and τ_θ^* the electron temperature relaxation time modified by the electro-thermal feedback:

$$\tau_\theta^* = \frac{\tau_\theta}{1-C_0I_0^2\frac{R_L-R_0}{R_L+R_0}} \tag{2.24}$$

The DSB mixer input noise temperature which also includes noise from the IF chain T_{IF} is [153]:

$$T_m(f_{IF}) = \frac{T_J+T_{FL}+T_{IF}}{2G_m(0)(1+(\frac{f_{IF}}{f_g})^2)^{-1}} \tag{2.25}$$

The thermal fluctuation noise depends on the IF as $(1+(2\pi f_{IF} \tau_\theta^*)^2)^{-1}$. Since τ_θ^* and a mixer time constant $\tau_{mix} = (2\pi f_g)^{-1}$ basically are equal, Equation 2.25 could be rewritten as:

$$T_m(f_{IF}) = \frac{T_{FL}(0)+(T_J+T_{IF})(1+(\frac{f_{IF}}{f_g})^2)}{2G_m(0)} \tag{2.26}$$
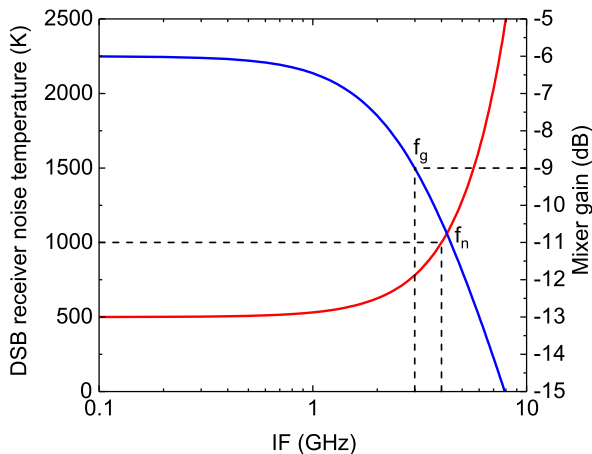
Fig. 2.7: HEB mixer noise temperature and conversion gain versus IF.

And then defining a new parameter f_n as a mixer NBW:

$$f_n = f_g \sqrt{\frac{T_{FL} + T_J + T_{LNA}}{T_J + T_{LNA}}} \tag{2.27}$$

the final equation becomes:

$$T_m(f_{IF}) = T_m(0)\ (1 + (\frac{f_{IF}}{f_n})^2) \tag{2.28}$$

where $T_m(0)$ is a mixer noise temperature at zero IF. It should be noted that according Equation 2.27 f_n is always larger then f_g, because the radicand is larger than 1 (see Figure 2.7).

2.2.3 Two-temperature model

In the low temperature limit when c_e is much larger then c_p the electron temperature relaxation could be described with a single time constant τ_θ [155]:

$$\tau_\theta = \tau_{ep} + \tau_{esc} \frac{c_e}{c_p} \tag{2.29}$$

while in a general case a relation between τ_θ, τ_{ep} and τ_{esc} is more complicated.

A two-temperature approach (2-T model) was used in order to describe the response of superconducting films to a modulated electro-magnetic radiation [142]. Taking into account the effect of self-heating electrothermal feedback [156] the HEB conversion gain as a function of IF is [124]:

$$G_m(f_{IF}) \propto |\frac{C'}{\xi(f_{IF}) - C' \frac{R_L - R_0}{R_L + R_0}}|^2 \tag{2.30}$$

where

$$\xi(\omega) = \frac{(1 + j\omega\tau_1)(1 + j\omega\tau_2)}{(1 + j\omega\tau_0)} \tag{2.31}$$

(a)   (b)

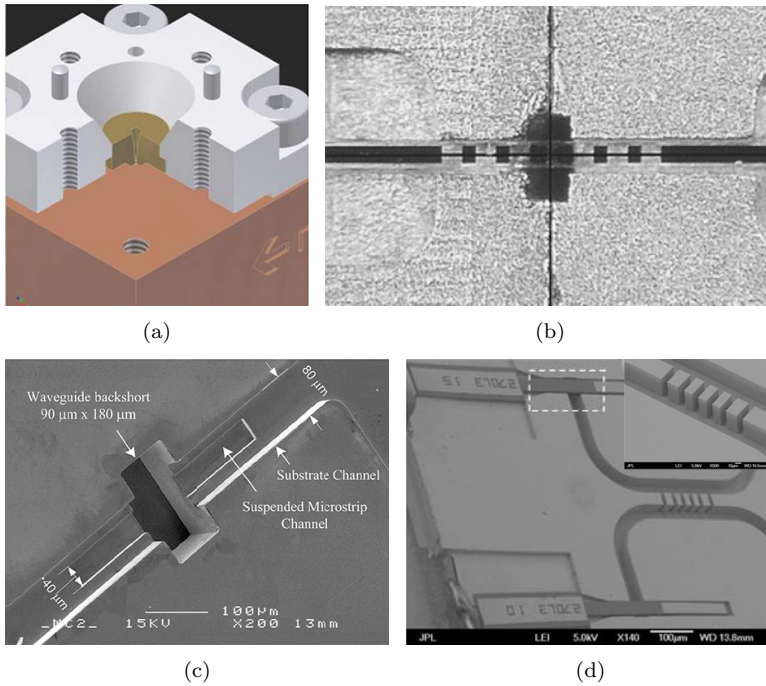(c)   (d)

Fig. 2.8: Waveguide HEB heterodyne receivers. (a) Three-dimensional (3D) computer-aided design (CAD) image: sectioned cut of a feed horn antenna. Illustration from [31]. (b) SEM image of a HEB mixer mounted on the waveguide mixer block. Illustration from [115]. (c) SEM image of a microchannel with a backshort. Illustration from [19]. (d) SEM image of a 90°hybrid coupler. Illustration from [111].

$$\tau_3^{-1} = \tau_{esc}^{-1} + \tau_{ep}^{-1}\frac{c_e}{c_p} \tag{2.32}$$

$$\tau_{1,2}^{-1} = \frac{\tau_3^{-1} + \tau_{eph}^{-1}}{2}\left[1 \pm \sqrt{\left(1 - 4\frac{(\tau_3^{-1} + \tau_{ep}^{-1})^{-2}}{\tau_{esc}\tau_{ep}}\right)}\right] \tag{2.33}$$

However, simplified Equation 2.29 gives a good understanding of a trade-off in HEB mixer development. As it is seen from Equation 2.15 it is required to reduce the film thickness to achieve the shorter phonon escape time. Unfortunately, reduction of film thickness leads to decrease of T_c, i.e. due to a large amount of defects in a film bottom layer. NbN with a bulk T_c of 16 K has only a 8–11 K T_c in 3–5 nm films. The reduction of T_c consequently leads to an increase of electron-phonon interaction time.

2.3   THz heterodyne receivers design

The HEB itself operates just as a mixing element. In order to use HEB in a heterodyne receiver the problem of effective signal and LO radiation coupling
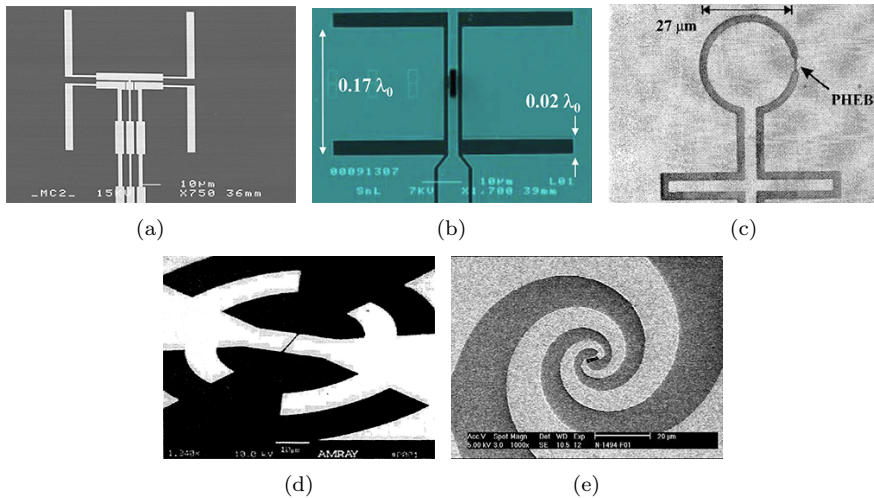
Fig. 2.9: Integrated planar antennas. (a) Double dipole antenna. Illustration from [157]. (b) Double slot antenna. Illustration from [98]. (c) Slot-ring antenna. Illustration from [158]. (d) Log-periodic antenna. Illustration from [159]. (e) Spiral antenna. Illustration from [97].

into device, DC biasing and IF signal redout should be solved. There are two main approaches for the receiver design that differ by the manner radiation is coupled into the device: waveguide coupling and quasi-optical coupling.

In the waveguide coupling approach a feed horn antenna (see Figure 2.8(a)) is used for radiation coupling from the free space into a machined waveguide with a mounted device (see Figure 2.8(b)). The HEBs integrated with a probe antenna are typically fabricated on thin substrates. The tunable element (backshort) could be used to maximize radiation coupling from the waveguide into the device (see Figure 2.8(c)). The optimal frequency range for radiation coupling for the waveguide receiver is defined by the antenna and waveguide geometry. The drawback of this receiver type is that the waveguide dimensions scale down for higher frequencies and fabrication becomes more challenging. High frequency operation also necessitates a reduction of substrate thickness due to increasing waveguide losses and substrate modes formation. However, waveguide HEB mixers have been successfully developed for frequencies up to 4.7 THz [19, 31, 33, 111, 115]. In waveguide receivers axial and lateral positions of the mixer beam are determined only by the feed horn antenna (i.e. by the machining tolerances only). However, the mixer chip mounting in the correct position for maximum coupling could be challenging. Using waveguide approach it is possible to avoid thin film beam splitter utilization for combining signal and LO radiation. The balanced scheme used to improve receiver stability could be realized easily using built in machined hybrid coupler as shown in Figure 2.8(d) [111].

In the quasi-optical coupling approach a lithographic planar antenna directly integrated with a HEB is used. Figure 2.9 demonstrates several types of integrated planar antennas used with HEB mixers, e.g. a double dipole an-
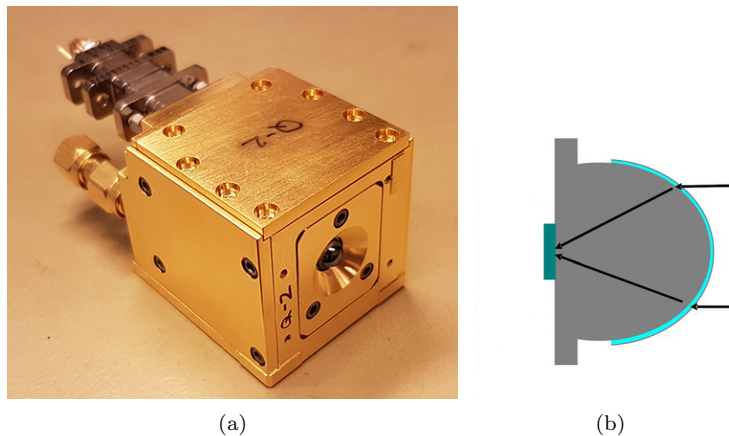
(a)   (b)

Fig. 2.10: (a) Quasi-optical mixer block used for HIFI instrument of The Hershel Space Observatory. (b) Elliptical dielectric lens with a planar antenna integrated HEB mixer attached. Illustration from [98].

tenna [157], a double slot antenna [98], a slot-ring antenna [158], a log-periodic antenna [159] and a spiral antenna [97]. The spiral antenna is a good choice for a laboratory study of devices at different LO frequencies, because it has a constant real impedance in a broad frequency range. The impedance of a HEB can be easily matched to the antenna impedance by choosing the right HEB geometry. Unfortunately, real spiral antennas have an elliptical polarization, while the radiation of LO source are typically linear polarized. That results in LO coupling losses (at least 50%) and complexity of loss estimation of a beam splitter used for combining signal and LO radiation.

For a planar antenna on a dielectric substrate coupling into the substrate is $\epsilon^{3/2}$ times (ϵ is the dielectric substrate permittivity) higher than into the air. The incoming radiation then should be fed from the substrate side. In this case the radiation propagating at the angles larger than the critical angle will be trapped in the substrate, so an additional beam handling is required. In order to avoid this problem, hyperhemispherical and elliptical dielectric lenses are typically used [160]. The planar antenna integrated HEB mixer is attached to the back side of the lens and packed in a mixer block (see Figure 2.10). The antenna gain in case of hyperhemispherical lens is increased by n_l^2 (n_l is the lens dielectric refractive index). In practice, hyperhemispherical and elliptical lenses can be realized approximately by using a hemispherical lens and a dielectric plate of required thickness placed between the hemisphere and the substrate. Use of lenses results in losses caused by the reflection of radiation at the lens/air interface. Reflection losses could be reduced by applying antireflection coating [161]. Application of Parylene C antireflection coating allows for reduction of the reflection loses from 1 dB to 0.2 dB [93].

Chapter 3

MgB$_2$ superconducting ultrathin films

In this chapter the detailed description of HPCVD method, the deposition system design, and the study of achieved films presented in [Paper C] and [Paper D] are summarized.

3.1 MgB$_2$ thin films

In order to increase operation temperature and to improve IF bandwidth of HEB mixers, superconducting materials with a higher T$_c$, which can provide a shorter electron-phonon interaction time are required. MgB$_2$ is one of these materials. Thinner films provide shorter phonon escape time from the film into the substrate, which is another important limitation for the HEB mixers IF bandwidth. Hence, both high T$_c$ and small thickness superconducting films are desirable. The superconductivity in MgB$_2$ was reported in 2001 [127]. MgB$_2$ is a conventional intermetallic compound superconductor with the highest T$_c$ for a traditional phonon mediated superconductor of 39 K reported so far. The crystalline structure of MgB$_2$ is shown in Figure 3.1. It consists of hexagonal magnesium (Mg) layers and honeycomb boron (B) layers in-between. The hexagonal unit cell has the following lattice parameters a = b = 3.086 Å, c = 3.524 Å [127]. Despite MgB$_2$ is a conventional Bardeen-Cooper-Schrieffer (BCS) superconductor, it exhibits a double superconducting gap structure with $2\Delta_\sigma \approx 4k_BT_c$ and $2\Delta_\pi \approx 1.3k_BT_c$ [162]. In the dirty limit, due to strong interband and intraband scattering two superconducting gaps merge into one energy gap $2\Delta_{dirty}$ whose temperature dependance deviates from curve predicted by BCS theory [163]. A penetration depth (λ_L) of 34.5 nm and coherence length (ξ) of 8 nm were reported for MgB$_2$ [164, 165]. Using the Ginzburg-Landau formula for the depairing current density J$_d$ = $\Phi_0/(\sqrt{3}\pi\mu_0\lambda_L^2\xi)$, where Φ_0 is the flux quantum and μ_0 the permeability of vacuum, it is estimated to be $\approx 3\times10^9$ A/cm^2.

The discovery of superconductivity in MgB$_2$ immediately brought a great interest to MgB$_2$ thin films [128, 166, 167]. Several techniques for *in-situ* thin film growth were proposed, e.g. pulsed laser deposition (PLD) [128], MBE
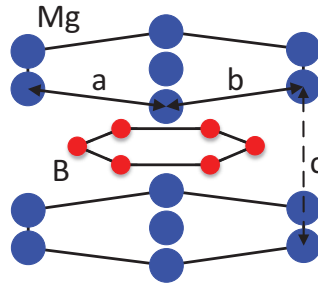
Fig. 3.1: MgB$_2$ crystal structure. Honeycomb boron layers are in between of hexagonal magnesium layers [127].
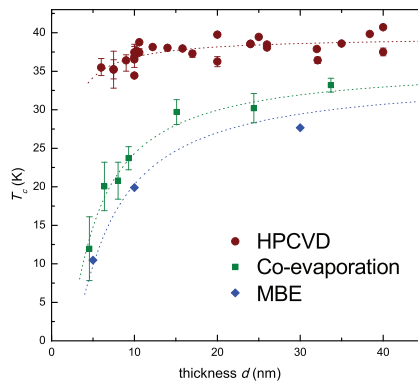

Fig. 3.2: Comparison of different MgB$_2$ thin film deposition techniques: MBE [174], co-evaporation [175], and HPCVD [172, 176, 177]. Illustration from Ref. [177].

[168], HPCVD [129], sputtering [169], e-beam and thermal co-evaporation [170]. The HPCVD grown MgB$_2$ films have a higher T$_c$ compared to films with the same thickness grown by other techniques (see Figure 3.2). Unfortunately, deposition systems utilizing HPCVD method are not commercially available.

The most suitable substrates for MgB$_2$ thin film deposition are Al$_2$O$_3$ and SiC with a lattice mismatch with MgB$_2$ of $\sim$11% (30° in-plane rotation) [171] and $\sim$0.42% [172], respectively. SiC is a more preferable substrate for MgB$_2$ thin film deposition due to a better film/substrate lattice match which results in a reduced number of defects in bottom layers of the film. This leads to a better phonon transparency of the film/substrate interface. It should be also noted, that both thermodynamic calculations [173] and experimental results [129] show that layers of magnesium oxide (MgO) form at the film/substrate interface, when Al$_2$O$_3$ substrates are used. More common substrates for microelectronics industry, such as Si and silicon dioxide (SiO$_2$), react with Mg to form silicides [173] and therefore require the use of appropriate buffer layers.

Significant progress in ultrathin MgB$_2$ film deposition allowed for fabri-
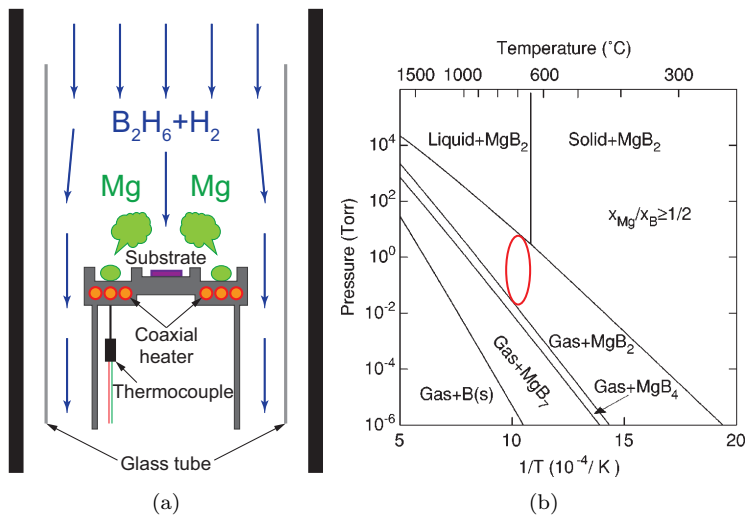
Fig. 3.3: (a) Schematic drawing of the HPCVD system's deposition chamber. (b) Pressure-temperature phase diagram for the Mg-B system. Illustration from Ref. [167].

cation of different types of superconducting electronic devices, e.g. HEB mixers [122], superconducting single-photon detectors (SSPD) [178], superconducting quantum interference devices (SQUID) [179]. MgB_2 thin films are of the great interest for HEB fabrication due to a potential possibility to achieve a wider IF bandwidth and higher operation temperatures compared to NbN HEB mixers. The shorter electron-phonon interaction time was measured in a thin MgB_2 film on a Si substrate (3 ps) [162] in comparison to NbN (12 ps) . The possibility to deposit very thin films (6–8 nm) with a high T_c of 34–37 K has been demonstrated [172, 180]. However, no HEBs made utilizing such thin films have been reported to date. The recently reported results on MgB_2 HEB mixers were achieved with devices fabricated from MBE grown films on Al_2O_3 [123, 124, 131] substrates and HPCVD grown films on SiC substrates [125, 126, 132].

3.2 Chalmers HPCVD system

Initial studies of MgB_2 HEB mixers were performed using MBE grown films on c-cut Al_2O_3 substrates provided by NTT Basic Research Laboratories [181]. Typically, the T_c of MBE grown films is much lower than for HPCVD grown films, but the film surface is smoother, which is essential for the device fabrication and performance. The film deposition process included co-evaporation of Mg and B in a high-vacuum chamber at 280°C and subsequent Ar atmosphere annealing in a rapid-annealing furnace. Films were covered *in-situ* with a 20 nm Au layer to reduce contact resistance between a MgB_2 film and metal layers deposited during device fabrication and to prevent film degradation during storage and initial device fabrication steps. A HPCVD method developed

for MgB$_2$ thin film growth can provide high quality ultrathin superconducting films that can maintain a high T$_c$ even when few nanometers thick. On the other hand, the availability of in-house source of thin films is of a great advantage for device development. Therefore, a custom made HPCVD system was constructed at Chalmers University of Technology for MgB$_2$ ultrathin film deposition as a part of the project on MgB$_2$ HEB mixers development.

3.2.1   System design

The HPCVD technique utilizing a combination of both physical and chemical vapor deposition was proposed specifically for MgB$_2$ thin film growth. The Mg source is an evaporative flux from solid Mg and the B source is a diborane (B$_2$H$_6$) gas. In brief, in this process both the Mg pellets and the substrate are placed on a heater (either resistive or inductive) while a mixture of hydrogen (H$_2$) and B$_2$H$_6$ gases is supplied into the chamber as shown in Figure 3.3(a). The B$_2$H$_6$ gas decomposes above the heated substrate into borane (BH$_3$) gas. The borane molecules are adsorbed on the substrate surface and react with evaporated Mg to form an MgB$_2$ film. The film growth usually occurs at temperatures ranging from 650°C to 760°C [129, 133, 172, 182], which is above the Mg melting point of 650°C (the area marked with a red oval in Figure 3.3(b)). As one can see, in order to form the correct crystalline phase (MgB$_2$) both the Mg partial pressure and the temperature should fall in a quite tight area in the phase diagram. This necessitate very fine tuning of deposition parameters.

The system photos are presented in Figure 3.4. H$_2$, B$_2$H$_6$ (5% diluted in H$_2$), and purging nitrogen (N$_2$) gases are supplied to the deposition chamber using a computer controlled gas panel consisting of pneumatic valves and mass-flow controllers (see Figure 3.4(a)). A pirani gauge is mounted on the deposition chamber to monitor the pressure during system pumping. A throttle valve operated through a controller with a capacitance manometer is used to set the desired process pressure. A kinetic trap (see Figure 3.4(c)) after the deposition chamber is installed in order to protect following system components from residuals of the deposited material carried by the gas flow. A fore-vacuum pump and a scrubber used for B$_2$H$_6$ disposal are placed behind a main cabinet in an utility room (see Figure 3.4(d)).

A schematic of the MgB$_2$ HPCVD system chamber is presented in Figure 3.3(a). A quartz tube prevents material deposition on water cooled chamber metal walls. Both the substrate and pieces of solid Mg are placed on a heater. A coaxial heating wire is clamped between an upper and a bottom parts of the heater under an area where magnesium is placed (see Figure 3.4(b)). In contrast to the previously presented resistive heater designs the coaxial wire itself is hidden inside the heater, which reduces contamination of the wire during depositions and increases the heater life time. Due to a temperature gradient the temperature of the central part where the substrate is placed is 50 K lower than under Mg pellets. A thermocouple is attached to the bottom part of the heater to monitor the temperature during the deposition process.

The MgB$_2$ thin film deposition procedure is following:

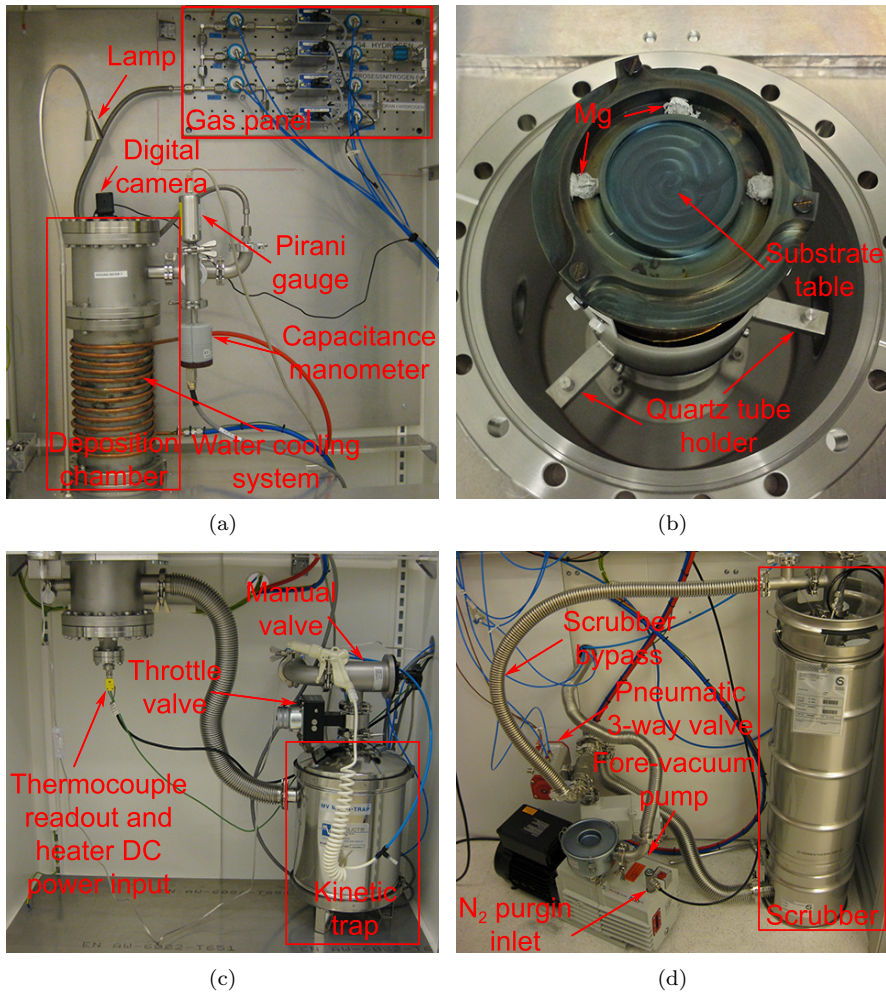1. The chamber is pumped to the base pressure (10^{-3} Torr).

Fig. 3.4: Chalmers in-house built MgB$_2$ HPCVD system. (a) Top part front view. (b) Deposition chamber inside view (c) Bottom part front view. (d) The utility room view.
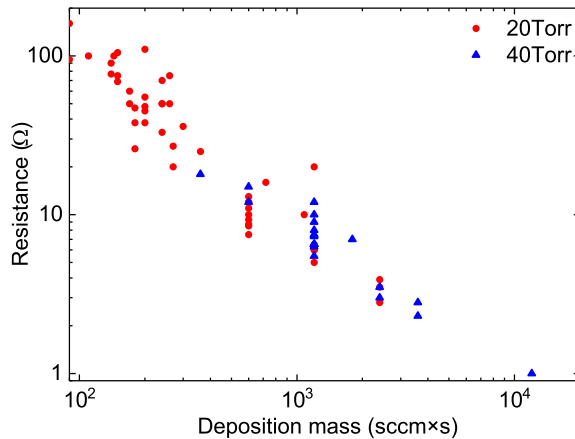
Fig. 3.5: MgB$_2$ film resistance measured on 5×5 mm^2 size test wafers (SiC) versus deposition mass. Films are deposited at either 20 Torr or 40 Torr.

2. The chamber is flushed with H$_2$ gas and pumped again to the base pressure.

3. The chamber is filled with H$_2$ gas (400 sccm) to the desired pressure (typically 20 Torr).

4. Solid Mg and the substrate are heated to about 700°C.

5. The B$_2$H$_6$ gas mixture is turned on for the desired time.

6. After the deposition is finished the heater is turned off and the substrate is cooled down.

7. The chamber is flushed several times with N$_2$ gas in order to remove possible remaining B$_2$H$_6$ gas.

3.2.2 Safety

During the HPCVD deposition system design and construction several safety issues had to be solved. The gases used in the system are dangerous for the personnel and laboratory environment. The gas panel, the deposition chamber, and other main system components are placed inside the ventilated cabinet. Furthermore, the gas panel is covered with a metal shield and has additional ventilation exhaust with a higher flow to form a negative pressure difference in case of a gas leakage. The cabinet doors have switches connected to an inter-lock system preventing process gases supply when doors are opened. The output of the pressure controller is also connected to the inter-lock system such as gas supply is possible only if the pressure inside the deposition chamber is below 300 Torr.

B$_2$H$_6$ is a pyrophoric gas and can self-inflame even at a room temperature. Moreover, B$_2$H$_6$ has a toxic effect primarily due to its irritant properties. In

Table 3.1: HPCVD MgB$_2$ HEB thickness (d), size (W×L), critical temperature (T$_c$), resistance at room temperature (R$_{295K}$), resistivity (ρ_{295K}), and critical current density (J$_c$)

Device	d(nm)	W×L (μm^2)	T$_c$(K)	R$_{295K}(\Omega)$	ρ_{295K} ($\mu\Omega \times cm$)	J$_c$ (10^7A/cm^2)
E2-1	30	1×1	39.6	39	117	8.8
E2-2	30	1×1	39.4	40	120	11.0
E3-2	20	0.5×0.5	38.6	25	50	10.5
E3-8	20	0.8×0.8	39.2	20	40	12.0
E6-4	12	1×1	33.5	44	53	2.0
E6-7	12	1×1.5	34.5	67	54	2.9
E8-2	10	0.3×0.3	34.0	52	52	2.5
E8-7	10	0.5×0.5	32.5	87	87	1.2
E10-7	8	1×1	30.0	196	157	0.9
E10-8	8	1×1	31.0	230	182	1.2
E15-7	5	1×1	32.5	130	65	2.8

order to avoid an exposure of laboratory environment to B$_2$H$_6$, which is highly undesirable, a remotely controlled bypass line with a B$_2$H$_6$ gas sensor was installed after the fore-vacuum pump (see Figure 3.4(d). After the completion of film deposition procedure the system exhaust is switched to the bypass to make sure there is no B$_2$H$_6$ gas left in the chamber. The inter-lock system prevents switching to the bypass during the deposition process.

H$_2$ is a flammable gas and can self-explode in a certain concentration with oxygen (O$_2$). H$_2$ gas cleaned from B$_2$H$_6$ is mixed at the scrubber exhaust with N$_2$ to prevent formation of explosive concentrations of the oxyhydrogen. Another N$_2$ gas line is connected to an oil return inlet of the fore-vacuum pump in order to avoid accumulation of H$_2$ in the pump oil. The pump N$_2$ gas line has a lower flow and is always turned on, while the exhaust N$_2$ gas line with a higher gas flow is turned on only during the HPCVD system operation. The N$_2$ gas flows are controlled with gas flow meters which are also connected to the inter-lock system.

3.3   HPCVD grown ultrathin films

In the HPCVD process film thickness is defined by a B$_2$H$_6$ flow rate and a deposition time. As a measure of the deposited material amount a product of the B$_2$H$_6$ flow rate and the deposition time, so called deposition mass, can be used. Immediately after the chamber is opened, resistance of the deposited film is measured using multimeter from corner to corner of the substrate. The resistance was found to be inversely proportional to the deposition mass over two orders of magnitude, which suggests a good connectivity of the obtained films. Initially, MgB$_2$ thin films were grown on Al$_2$O$_3$ substrates. Even the first film deposition using the newly built system was successful, and film with a T$_c$ of 34 K was achieved (see Figure 3.6(a)). A T$_c$ of grown films ranged from 33 K (15 nm) to 37 K (40 nm) with a distinct double transition for thinner films. The film surface was covered with lots of spots and particles (see Figure
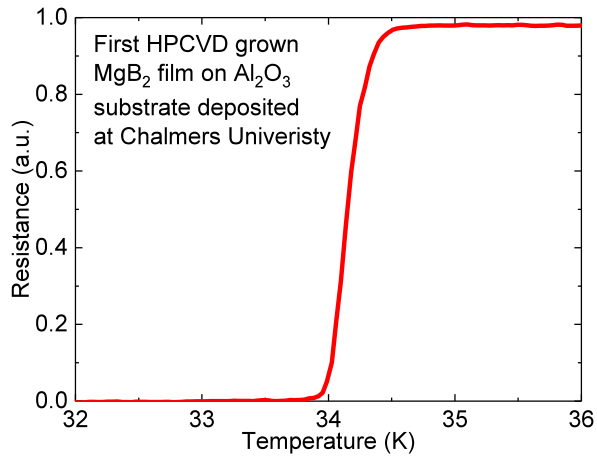
(a)
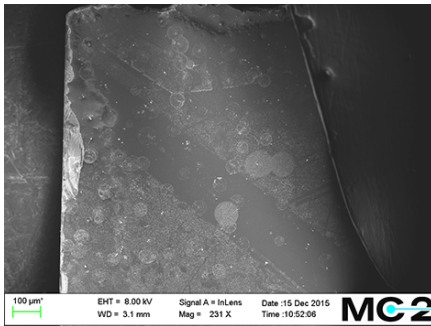
(b)
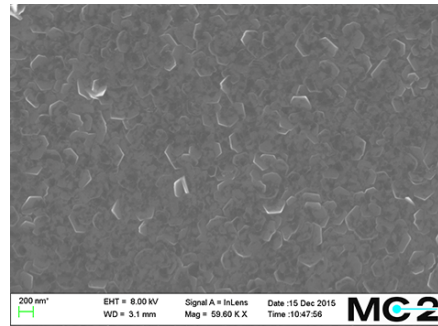
(c)

Fig. 3.6: First HPCVD grown MgB$_2$ films on Al$_2$O$_3$ substrates deposited at Chalmers University (20 sccm, 120 s, 40 Torr). (a) The resistance versus temperature curve for the first film. (b) SEM image of the second film. (c) High magnification SEM image of the second film.
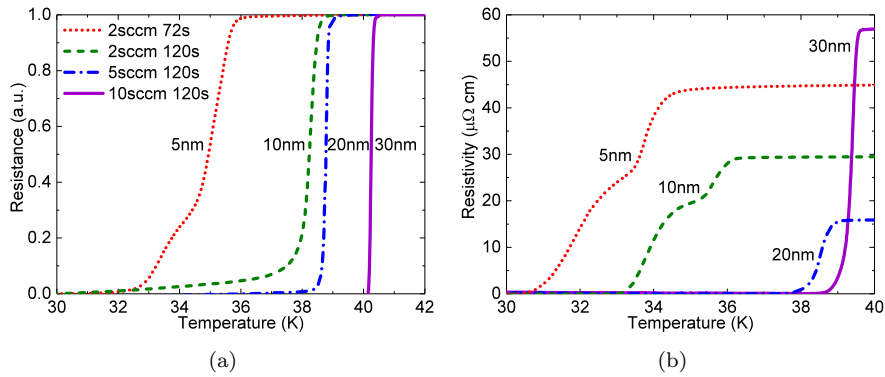
Fig. 3.7: (a) Resistance versus temperature curve for HPCVD grown MgB$_2$ films on SiC substrates after the deposition. (a) Resistivity versus temperature curve for bridges fabricated from HPCVD grown MgB$_2$ films on SiC substrates.

3.6(b)). HPCVD films are assumed to grow in a Volmer-Weber mode and large (300 nm in diameter) hexagonal crystallites corresponding to the MgB$_2$ unit cell are clearly distinguishable in scanning electron microscope (SEM) image (see Figure 3.6(c)). For MgB$_2$ films on Al$_2$O$_3$ substrates the residual resistance ratio (RRR $=$ R$_{295K}$/R$_{ons}$, where R$_{295K}$ is the room temperature resistance and R$_{ons}$ the onset resistance) was 1.5–2.5 suggesting a high defect concentration. The RRR values are much lower than value (about 10) reported previously for clean MgB$_2$ films [133].

Further deposition process development and optimisation were performed using SiC substrates. The discussed films have a T$_c$ ranging from 35 K (5 nm thick) to 41 K (30 nm thick) (see Figure 3.7(a)). The RRR of the films is ranging from 2 to 6 indicating an improvement of film quality. The film surface was also studied with atomic force microscope (AFM). The measured mean square roughness (see Figure 3.8(d)) was about 1 nm, which is lower than for previously reported HPCVD as grown ultrathin MgB$_2$ films [183]. A low roughness is one of the key characteristics affecting fabrication of micro- and nanostructures in thin films. We observed that reduction of the deposition pressure from 80 Torr to 20 Torr continuously leads to smoother film surfaces. For deposition pressures above 30 Torr a droplet formation occurs in the deposition chamber resulting in rougher films. Therefore, most of the discussed films used for HEB fabrication were grown at a pressure of 20 Torr. Film epitaxial growth is confirmed by both the transmission electron microscope image (see Figure 3.8(b)) and MgB$_2$ epitaxial response in X-ray diffractometer (XRD) scan (see Figure 3.8(c)).

Film DC parameters in patterned microstructures were studied in several batches of HEBs fabricated using either ultraviolet (UV) or electron beam (e-beam) lithography based process (see Chapter 4). Summary of DC measurement results for devices selected for THz characterisation are summarised in Table 3.1. MgB$_2$ films were covered with a 20 nm gold (Au) layer using magnetron sputtering directly after the deposition. This Au layer was used both to protect the deposited film from degradation in the atmosphere as well as
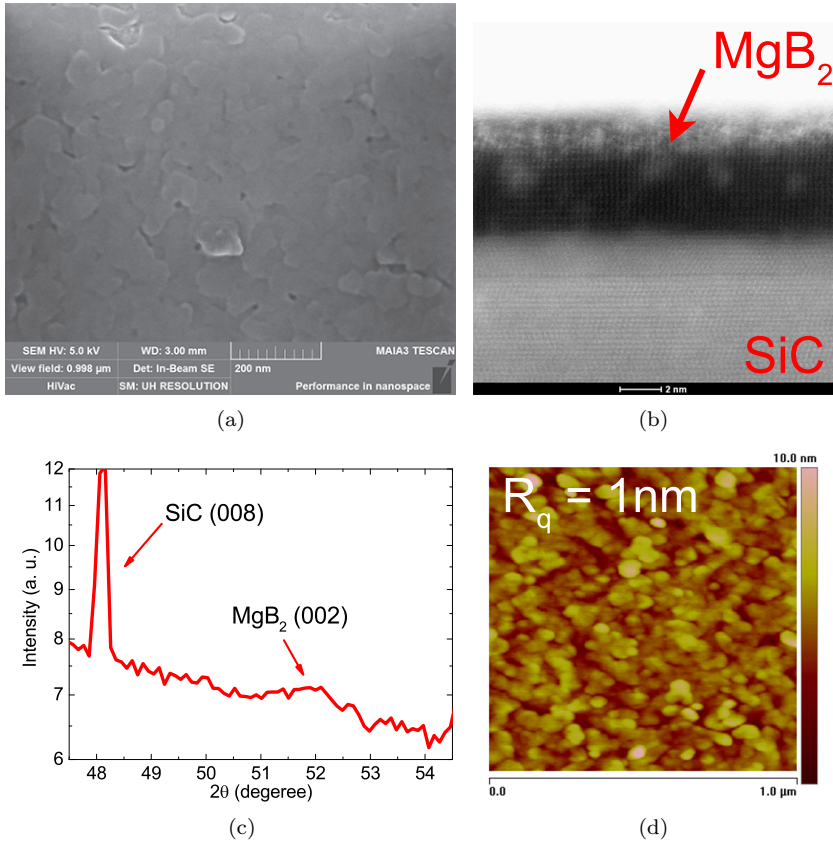
(a)

(b)

(c)

(d)

Fig. 3.8: A 5nm thick as grown MgB$_2$ film. (a) SEM image. (b) TEM image. (c) XRD scan. (d) AFM image.

to be able to use the same fabrication process previously developed for HEBs made from MBE grown films [Paper A], [Paper B]. For batches E1-E8 a 2 nm thick Ti layer was deposited prior the 20 nm Au layer deposition to improve a layer adhesion. Since batch E9 the *in-situ* precleaning with argon plasma was used to remove the native oxide, improve the Au layer adhesion, and reduce contact resistance. There was no Ti layer used in the last case.

There are several tools to measure the conductive film thickness: contact and optical surface profilometers, AFM, TEM, ellipsometer, etc. Ellipsometry is a non-invasive method, however it requires preliminary knowledge of the MgB$_2$ film optical properties. Initially, for the deposition process development, film thickness was measured both with a contact profilometer and an AFM on MgB$_2$ films etched away on a fraction of the substrate using a hydrochloric (HCl) acid. Later, selected samples have been also studied using TEM to investigate the film/substrate interface as well as to measure MgB$_2$ film thickness. All thicknesses presented in Table 3.1 were confirmed with TEM measurements, except for device E2-2 for which it was estimated from the deposition rate.
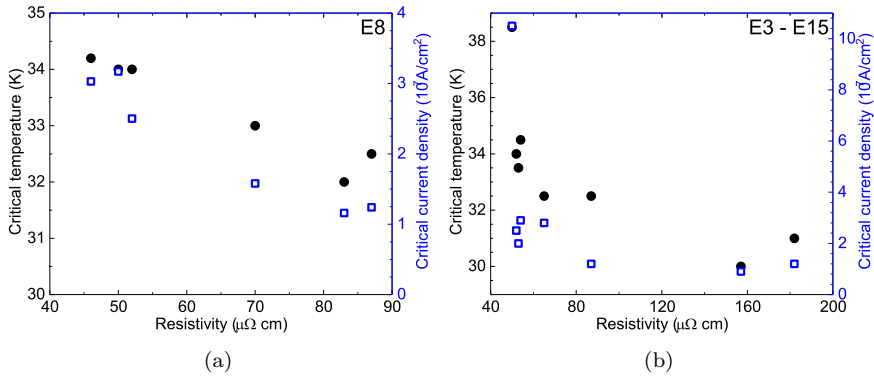
Fig. 3.9: Critical temperature and critical current density versus resistivity measured for the devices (a) from the same batch and (b) from batches of various thickness.

At room temperature sheet resistance of unpatterned films was measured with a four-point probe technique. Then by knowing the film thickness from TEM measurements the room temperature resistivity was calculated both for unpatterned films and for microstructures. These values correspond to the previously published resistivity values for films of similar thickness [180, 183–185]. The resistivity obtained from resistance of submicron size bridges (see Table 3.1) was ranging from $50\,\mu\Omega$cm (for a 20 nm thick film) till $182\,\mu\Omega$cm (for a 8 nm thick film). It is a factor of 2 higher than e.g. in Ref. [184] and [185], but much smaller bridges have been used. The high resistivity of the 30 nm thick film could be explained by a higher (40 Torr) deposition pressure, while the origin of the low resistivity in the 5 nm thick film is unclear.

The film resistivity affects design of HEB mixers. In order to provide the best performance, the impedance of HEB should be matched to the impedance of the integrated planar antenna (in our case a $100\,\Omega$ spiral antenna). With a resistivity of about 50–$100\,\mu\Omega$cm the aspect ratio of HEB (width/length) should be less than 1. Together with a requirement keeping a bolometer area small (due a limited available LO power) it will lead to the reduction of bolometer width in the design (in comparison to HEB mixers made from MBE grown MgB_2 films [Paper A], [Paper B]). That will increase the contact resistance between the HEB and the metal antenna, which subsequently increases the noise temperature.

In order to better understand the nature of the increased resistivity in thin films, the critical current density (J_c) has to be discussed. Whereas a T_c for thicker films remains the same in microbidges, for films thinner than 10 nm a T_c is reduces by a few degrees. Nevertheless, all films show excellent superconducting transition. The J_c values obtained from I-V characteristics of fabricated devices are presented in Table 3.1. For the 30 nm and 20 nm thick films the J_c is about $1\times10^8\,A/cm^2$ (at 4.2K), hence is one of the highest J_c reported so far for MgB_2 thin films. ($\approx10\%$ of the depairing current). Even for films thinner than 10 nm the J_c is $(1$–$3)\times10^7\,A/cm^2$. The same or higher resistivity and J_c of our films can possibly be explained by the lower deposition
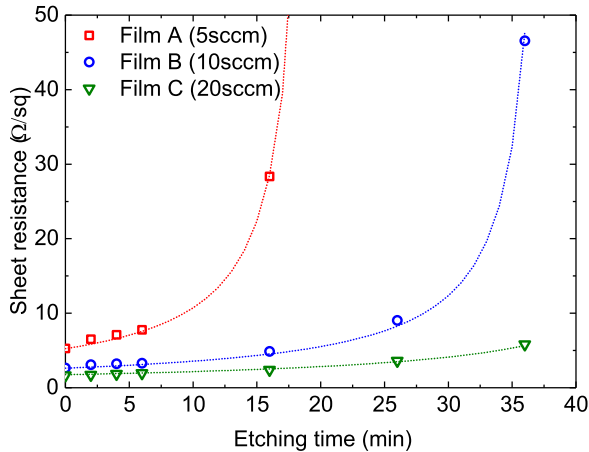
Fig. 3.10: Sheet resistance measured using four-point probe technique versus etching time. Deposition time and deposition pressure are $120\,\mathrm{s}$ and $20\,\mathrm{Torr}$, respectively.

rate in the discussed HPCVD system as compared to [184], which facilitate more uniform and homogenies MgB₂ film growth [186].

As mentioned above the J_c in submicron size bridges made from films thinner than $10\,\mathrm{nm}$ is lower than for thicker films. However, it is approximately a factor of 10 higher than for the previously reported microbidges made from MBE and HPCVD grown MgB₂ films. The high yield (above 75%) allowed for the study of correlation between the resistivity and the J_c of the submicron size bridges made from the same $10\,\mathrm{nm}$ thick film (see Figure 3.9(a)). The lower resistivity corresponds to the higher J_c. The same correlation is observed also for the T_c measured in submicron size bridges after the fabrication (see Figure 3.9(a)). The spread of parameters suggests that the $10\,\mathrm{nm}$ film is quite inhomogenies over the substrate area. The same dependance (see Figure 3.9(b)) of T_c and J_c on resistivity is observed for the devices made from films of various thickness (Table 3.1).

3.4   Films thinning down using Ar⁺ ion beam milling

Recently, argon ion (Ar⁺) beam milling was proposed as a technique for achieving ultrathin MgB₂ film from initially grown thicker films [180, 184, 185]. In order to study the effect of a thinning down on our HPCVD grown MgB₂ films, three films of various thickness were grown. The films were deposited with the same deposition parameters ($20\,\mathrm{Torr}$, $120\,\mathrm{s}$) except B₂H₆ gas flows: Film A ($5\,\mathrm{sccm}$), Film B ($10\,\mathrm{sccm}$), and Films C ($20\,\mathrm{sccm}$). The etching utilizing Oxford Ionfab 300 Ion Beam System ($2\,\mathrm{sccm}$ Ar gas flow, $13\,\mathrm{mA}$ beam current, $350\,\mathrm{V}$ beam voltage, and 30°tilt) was performed in several steps with sheet resistance measurements between them. Three steps with a duration of $2\,\mathrm{min}$ each followed by three steps with a duration of $10\,\mathrm{min}$ each. The film sheet resistance was measured with the four-point probe technique (see Figure

3.10). Due to the higher deposition mass, Film C should be approximately twice thicker than Film B and approximately four tomes thicker than Film A. Film B and Film C reach the same sheet resistance as Film A after approximately 20 min and 40 min of milling, respectively. Film A has completely gone after about 16–20 min of etching. The dependence of sheet resistance on etching time suggests that expected relations between film thicknesses based on the gas flows is correct.

Assuming that both the film resistivity and the etching rate are constant along the film vertical profile the sheet resistance is $R_s = $ r/(d–ρt), where r is the etching rate, and t the etching time. Fit to the experimental data gives the etching rate of 1–1.2 nm/min. This value corresponds to the etching rate observed during HEB fabrication. Film thicknesses for Film A, Film B, and Film C used for fitting are 20 nm, 40 nm, and 60 nm, respectively, and close to the values estimated using the deposition mass. It is still of a great interest how the milling will affect film homogeneity, film surface, and submicron structures in HPCVD grown MgB$_2$ films.

Chapter 4

MgB$_2$ HEB design and fabrication

Several batches of submicron and micrometer scale HEBs were fabricated from superconducting MgB$_2$ films grown by either MBE or HPCVD. An e-beam lithography based fabrication process was used for submicron size devices designed for noise performance characterisation, which is sensitive to the limited available LO power. For GBW characterisation micrometer scale devices were fabricated using UV lithography based process. Since GBW measurements are performed at lower frequencies (more LO power is available) and elevated bath temperatures (less LO power is needed), large size devices are acceptable.

In this chapter, the detailed description of device fabrication processes is presented.

4.1 E-beam lithography based process

The HEBs were fabricated using superconducting MgB$_2$ films either provided by NTT Basic Research Laboratories (MBE grown films) or deposited at Chalmers University of Technology (HPCVD grown films). The HEB chip design is shown in Figure 4.1. A broadband spiral antenna was chosen as the most suitable antenna type for HEB characterisation since the same device could be tested at various frequencies.

The fabrication of devices from MBE grown films was challenging. The bolometer high frequency impedance should be close to the spiral antenna impedance of $90\,\Omega$ in order to provide high efficiency coupling of THz radiation. Due to the high resistance of used MBE grown MgB$_2$ films ($\approx 1000\,\Omega/\square$ for $20\,\mathrm{nm}$ thick films) the bolometer should be short and wide to fulfill this requirement. A desirable aspect ratio is about 10:1, e.g. a $2\,\mu$m wide bolometer should be $0.2\,\mu$m in length. For such tasks the e-beam lithography allows pattern transfer with feature size down to $5\,\mathrm{nm}$ and provides more flexibility than projection UV lithography. In addition, since MgB$_2$ degrades during exposure to water and oxygen [187,188], some king of protection to preserve the quality of MgB$_2$ films during the processing should be considered, e.g. a SiN$_x$ or SiO$_2$ passivation layer. The fabrication procedure developed for MBE grown MgB$_2$
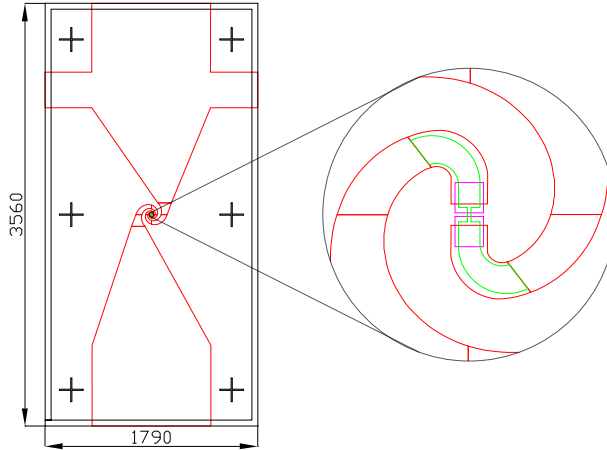
Fig. 4.1: The design of MgB$_2$ HEB mixer including alignment marks. The dimensions are given in microns.

films was also used for the fabrication of devices down to $0.3\,\mu$m in size from HPCVD grown films.

The fabrication procedure utilizing e-beam lithography, Ar$^+$ ion beam milling and lift-off process includes the following steps:

1. **Alignment marks and chip frames**: Initially, alignment marks for pattern alignment at subsequent processing steps and chip frames are fabricated. After the e-beam lithography, metal evaporation (10 nm titanium (Ti), 150 nm Au, and 30 nm Ti) and lift-off are performed (see Figure 4.2(a)). The chip frame is used both for short circuiting of bolometers and avoiding possible device damaging by the electrostatic charge; and cutting lines definition for the wafer dicing. The top Ti layer is used to protect structures during Ar$^+$ ion beam milling steps.

2. **Contact pads**: Contact pads defining the bolometer length are patterned. After the e-beam lithography, metal evaporation (10 nm Ti, 100 nm Au, and 60 nm Ti) and lift-off are performed (see Figure 4.2(b)). The top Ti layer is used to protect structures during Ar$^+$ ion beam milling steps.

3. **Spiral antenna**: The broadband planar spiral antenna is patterned. The antenna center part is overlapping with contact pads. After the e-beam lithography, metal evaporation (10 nm Ti, 270 nm Au, and 70 nm Ti) and lift-off are performed (see Figure 4.2(c)). The top Ti layer is used to protect structures during Ar$^+$ ion beam milling steps.

4. **Thin Au layer removal and passivation**: The 20 nm thick protective Au layer was etched away using Ar$^+$ ion beam milling (see Figure 4.2(d)). To prevent the degradation of the MgB$_2$ film during the rest of processing steps, immediately after the etching, the wafer was passivated with 40 nm thick SiN$_x$ film by RF magnetron sputtering process (see Figure 4.2(e)).
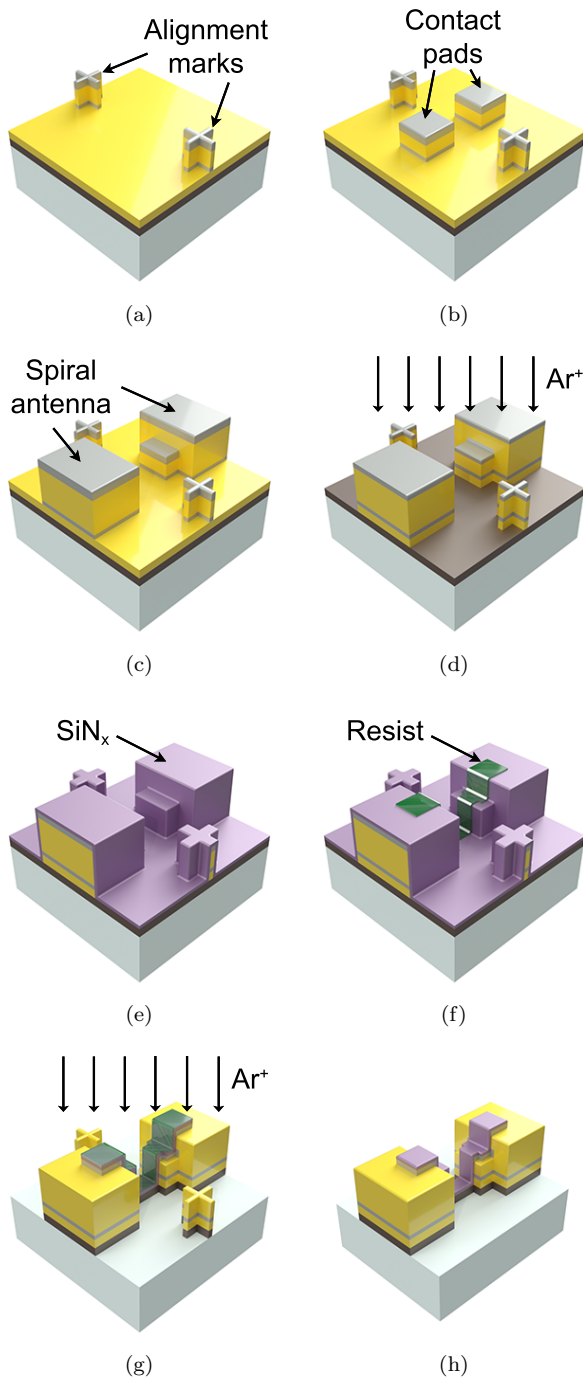
Fig. 4.2: Fabrication process sequence using e-beam lithography. (a) Alignment marks. (b) Contact pads. (c) Spiral antenna. (d) Thin Au layer removal. (e) Passivation with SiN_x. (f) Bolometer width patterning. (g) Ar^+ ion beam milling with a resist mask. (h) Final device.
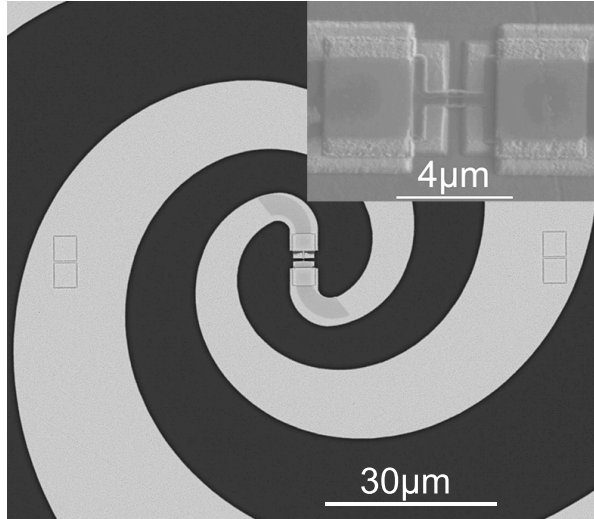
Fig. 4.3: SEM images of MgB$_2$ HEB made using e-beam lithography based fabrication process.

5. **Width definition and etching**: For the bolometer width definition etching mask was patterned using negative e-beam resist (see Figure 4.2(f)). The SiN$_x$ passivation and MgB$_2$ film were etched away except from the bolometer area protected by the resist (see Figure 4.2(g)).

6. **Dicing**: Finally, the wafer covered for mechanical protection with photoresist was cut into $1.5 \times 3.3 \, \text{mm}^2$ chips with the diamond dicing saw along the frame lines and washed in acetone to remove resist residuals(see Figure 4.2(h)).

The SEM image of the device fabricated using e-beam lithography based process is presented in Figure 4.3. The SEM picture in the inset of Figure 4.3 was done during the preparation of one of the samples for TEM analysis.

4.2   UV lithography based process

In order to acquire information about film parameters in microstructure during HPCVD process optimization faster, the UV lithography based process was used for HEB fabrication. Compared to the approximately one week required for fabrication when e-beam based process is applied, just 1-2 days are needed for UV lithography based process which involves less steps. The fabrication sequence is as following:

1. **HEB length definition**: Initially, the bolometer length and alignment marks are defined with an image reversal photoresist which provides negative slope profile (see Figure 4.4(a)). The patterning was followed by metal evaporation (10 nm Ti, 270 nm Au) and lift-off steps (see Figure 4.4(b)).
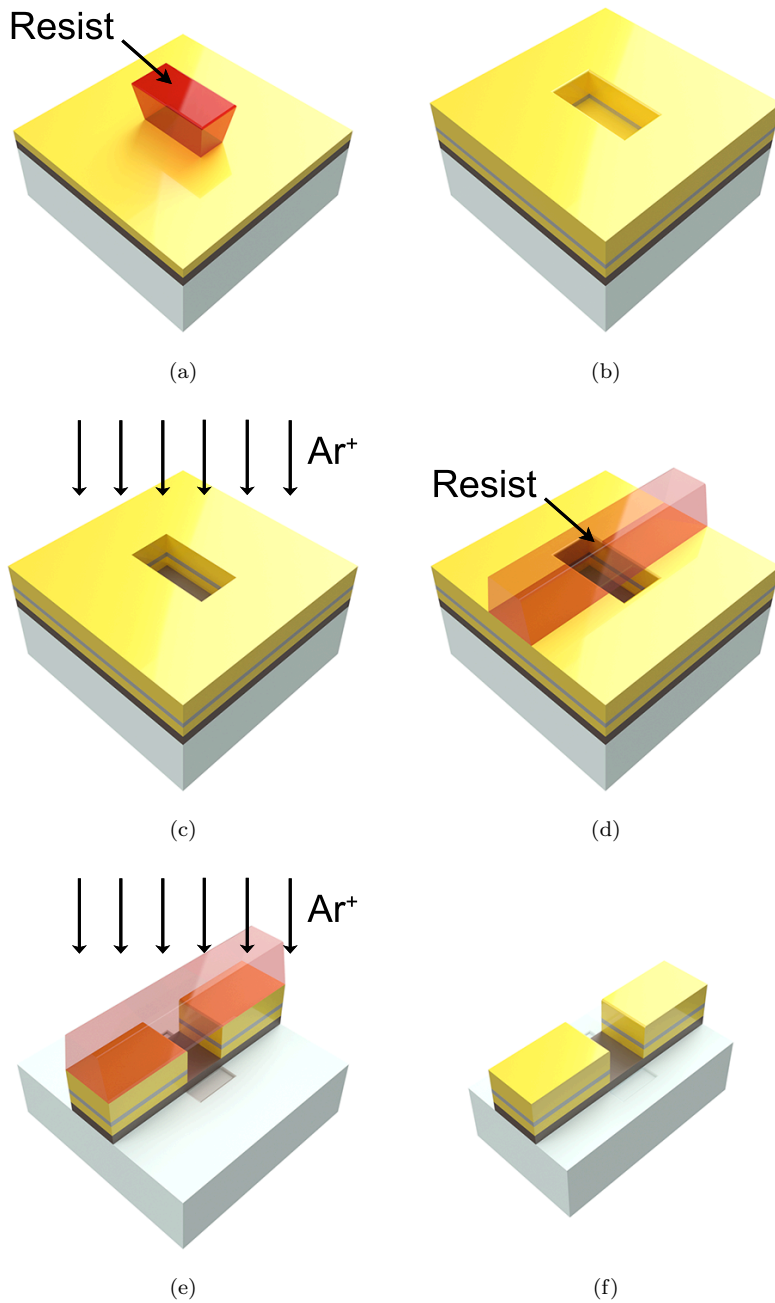
Fig. 4.4: Fabrication process sequence using UV lithography. (a) HEB length definition with resist. (b) Lift-off process. (c) Thin Au layer removal. (d) HEB width and spiral antenna definition with resist. (e) Ar$^+$ ion beam milling with a resist mask. (f) Final device.
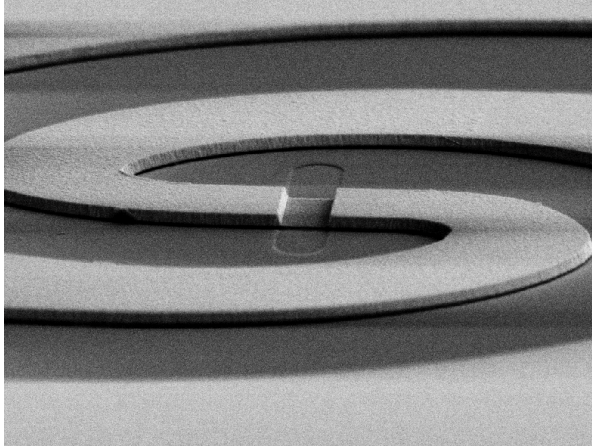
Fig. 4.5: SEM image of MgB$_2$ HEB made using UV-lithography based fabrication process [Paper A].

2. **Thin Au layer removal**: At this stage the 20 nm thick protective Au layer was etched away using Ar$^+$ ion beam milling (see Figure 4.4(c)).

3. **Spiral antenna definition**: Next, the spiral antenna with the inner part corresponding to the bolometer width and chip frames were patterned with positive photoresist (see Figure 4.4(d)). Then the developed photoresist was used as an etching mask for Ar$^+$ ion beam milling. The metal and MgB$_2$ layers were etched away down to the substrate (see Figure 4.4(e)).

4. **Dicing**: Finally, the wafer covered with photoresist for mechanical protection was cut into $1.3\times3.5\,\text{mm}^2$ chips with the diamond dicing saw along the frame lines and washed in acetone to remove resist residuals (see Figure 4.4(f)).

The SEM image of the device fabricated using UV lithography based process is presented in Figure 4.5. The UV lithography does not allow for features below $1\,\mu$m in size, so such the devices were used mostly for DC characterisation and heterodyne mixing experiments. The HPCVD grown MgB$_2$ films have lower resistance (50–200 $\Omega/\square$ for 5–10 nm thick films) compared to MBE grown films, so the required aspect ratio of device dimensions is about 1:1. The available LO power is limiting the maximum width of our HEBs to couple of microns. From another side fabrication of narrow HEBs is not desirable due to a higher contact resistance. As a result, low noise MgB$_2$ HEB mixers could be fabricated using UV lithography based process in most of the cases. However, extra fabrication step for bolometer microbridge passivation is required in order to improve device robustness.

Chapter 5

HEB mixers characterisation techniques

In order to characterise HEB mixers, fabricated chips have to be placed in a complex measurement setup which provides cooling to cryogenic temperatures, effective coupling of signal and LO radiation, voltage biasing, and readout of IF signal. The sensitivity figure of merit for mixers is a receiver input noise temperature which can be measured using the Y-factor technique. Loses and noise of measurement setup components affect measured receiver noise. Therefore, noise contribution of these components has to be analysed in order to study noise performance of HEB mixers themselves. The intrinsic mixer parameters (conversion gain and output noise temperature) can be measured with the U-factor technique using the achieved receiver noise temperature. Mixing of radiation from two sources, when the frequency of one source (LO) is fixed and the frequency of another source is tuned (signal) allows for the direct measurement of mixer GBW. However, the calibration of IF chain and tunable source output power is required.

This chapter describes techniques used for MgB_2 HEB mixers THz characterisation.

5.1 Sensitivity characterisation

In order to provide effective radiation coupling into devices, fabricated MgB_2 HEBs were mounted in a mixer block with a 5 mm elliptical Si lens (see Figure 5.1(a)). The mixer block was placed inside a cryostat (see Figure 5.2(a)) providing cooling down to LHe temperatures. A parabolic off-axis mirror was placed inside the cryostat to focus an incident radiation into the device in order to improve radiation coupling from a LO. A Zitex™ IR block filter was mounted on a 4K screen of the cryostat. A bias-T followed the mixer block to apply a voltage bias to the device and to separate an IF response (see Fig. 5.2(a)). Several amplifiers were used in the IF chain to measure the IF response. One cryogenic low-noise amplifier (LNA) was used inside the LHe cryostat (Chalmers 1.5–4.5 GHz indium phosphide (InP) LNA) in order to amplify a low power IF signal. Two room temperature LNAs were used
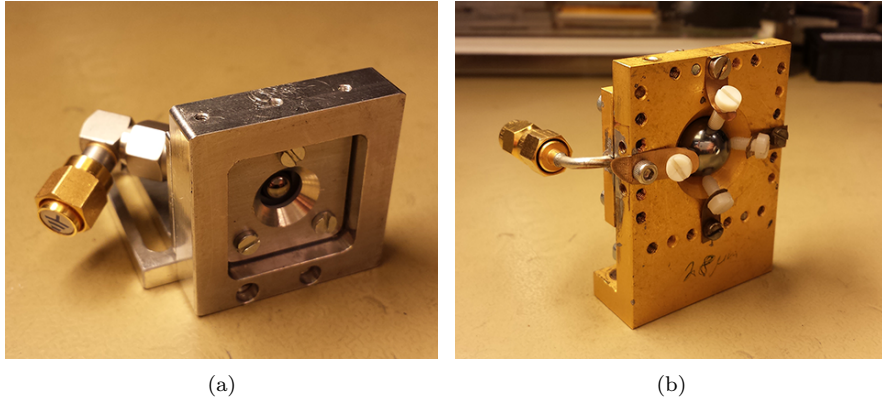
(a)   (b)

Fig. 5.1: Mixer blocks used for (a) sensitivity characterisation and (b) GBW measurements.

outside the cryostat (Chalmers 1.5–4.5 GHz Gallium arsenide (GaAs) LNA and MITEQ 0.1–10 GHz LNA) to amplify the IF signal further in order to overcome the noise floor. For the characterisation of HEBs with large noise bandwidth cryogenic and room temperature SIn1.5–4.5GHz band LNAs were substituted with a set of Chalmers 1.0–9.0 GHz InP LNAs.

The schematics of experimental setup is presented in Figure 5.2(b). A far-infrared (FIR) gas laser radiation (LO beam) was combined with signal from either hot or cold loads (Eccosorb sheets) using a Mylar® beam splitter. The emission lines of the FIR gas laser used for mixer sensitivity characterisation were 0.69 THz (formic acid (CH_2O_2) line), 1.63 THz, and 2.56 THz (difluoromethane (CH_2F_2) lines). A high-density polyethylene (HDPE) window let the incoming radiation enter the cryostat. The amplified IF signal was measured through a tunable 50 MHz band-pass YIG-filter with a powermeter. A Golay cell connected to the oscilloscope (not presented in Figure 5.2(b)) was placed behind the beam splitter to monitor the FIR gas laser output power during experiments. Various bath temperatures were used during tests. The temperature of boiling LHe under the standard conditions (4.2 K) were used as a base temperature. Pumping of helium vapour was performed to decrease a bath temperature down to 2 K. A resistive heater mounted directly on the mixer block was used for measurements at elevated bath temperatures up to 30 K (see Fig. 5.2(a)).

5.1.1   Y-factor technique

In order to measure the DSB receiver noise temperature T_{rec} the standard Y-factor technique [189] was used. Y is a ratio between receiver output powers with the hot P_{hot} and the cold P_{cold} loads (in this case 295 K and 77 K, respectively):

$$Y = \frac{P_{hot}}{P_{cold}} = \frac{2G_{tot}G_{IF}k_B(T_{rec}+T_{295K})B}{2G_{tot}G_{IF}k_B(T_{rec}+T_{77K})B} = \frac{T_{rec}+T_{295K}}{T_{rec}+T_{77K}} \qquad (5.1)$$
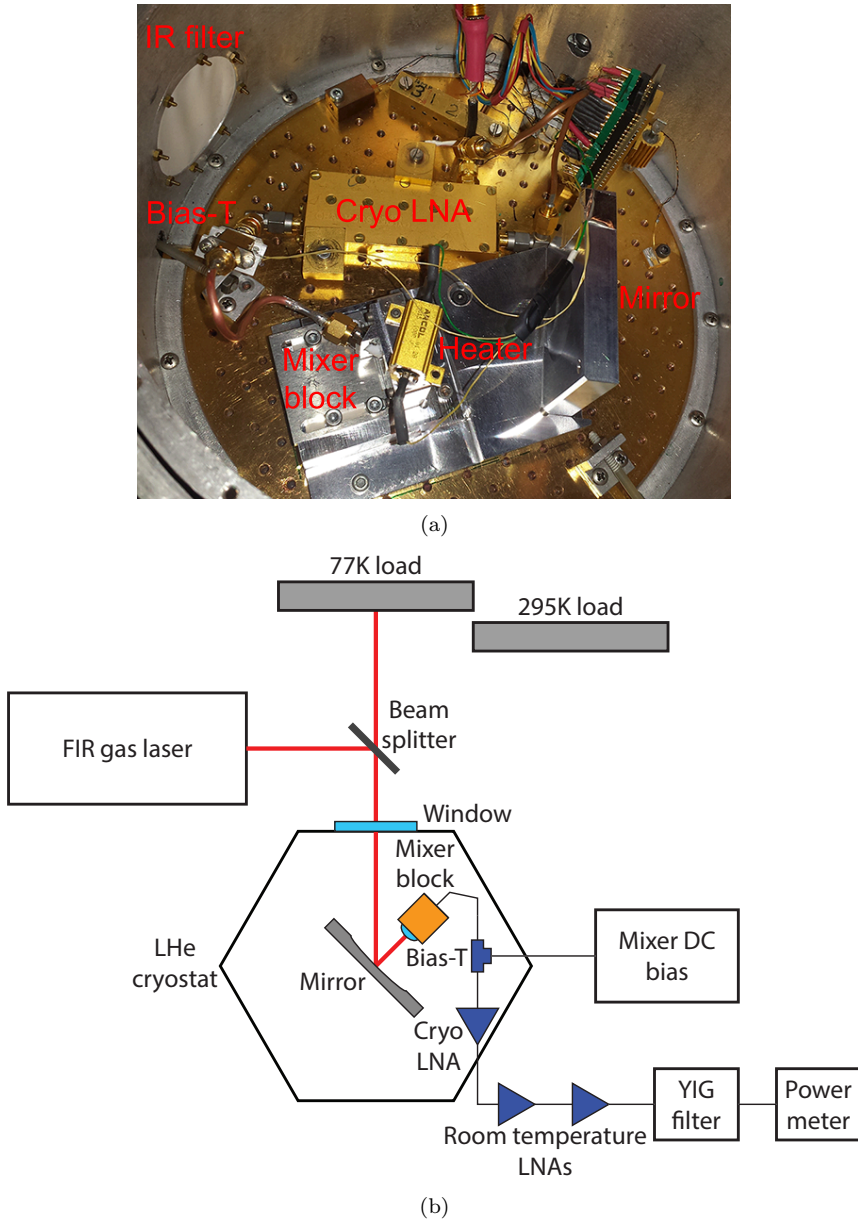
(a)

(b)

Fig. 5.2: Mixer noise and gain characterisation. (a) The cold plate of LHe cryostat. (b) The schematic of measurement setup.
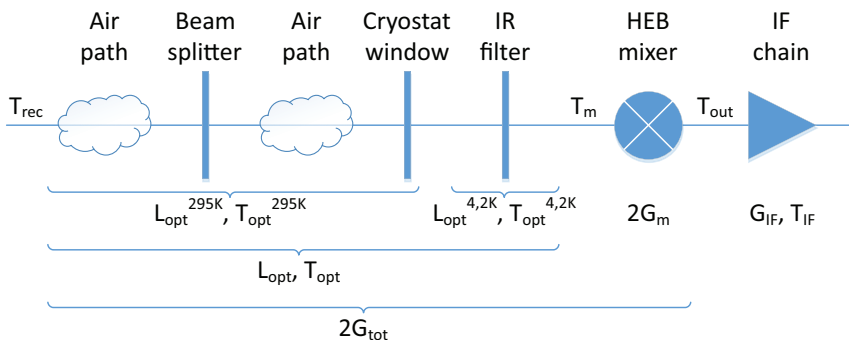
Fig. 5.3: Losses and equivalent noise temperatures of optical and electrical components in the signal path.

where G_{tot} is the total receiver gain, G_{IF} the IF chain gain, T_{IF} the IF chain input noise temperature, B the bandwidth, and T_{295K}, T_{77K} the Callen-Welton temperatures [190] of hot and cold loads. The noise temperature then could be calculated as:

$$T_{rec} = \frac{T_{295K} - Y \ T_{77K}}{Y - 1} \tag{5.2}$$

Since THz superconducting mixers (e.g. HEB mixers) are characterised in a complex set-up, both the loss and the noise contributions of optical components have to be analysed. That allows for de-embedding of the mixer input noise temperature. Figure 5.3 represents the signal path through the optical and electrical components in the receiver. A contribution of optical elements to a noise temperature can be calculated using the general formula for lossy components $T_{eq} = (L-1)T$ (where L is a component loss and T is a Callen-Welton temperature of component) and then deducted from the measured noise temperature (Table 5.1). The losses in the Si lens were treated as a part of mixer loss and was not deducted from the noise temperature. The DSB receiver noise temperature is then:

$$T_{rec} = T_{opt} + T_m \ L_{opt} + \frac{T_{IF}}{2G_{tot}} \tag{5.3}$$

where T_{opt} is the noise contribution of optical components and L_{opt} the optical losses.

5.1.2   U-factor technique

In order to measure both the mixer conversion gain and the output noise temperature, the U-factor technique [94] was applied. The U-factor is defined as a ratio between receiver output powers when the receiver is in an operating state and a reference state which can be characterised by an equivalent temperature T_{REF}. As a reference state either a superconducting state or a normal state could be used. In a superconducting state a HEB works as a microwave short and reflects all power coming from an IF chain ($T_{REF} = T_{IF}$). A normal

Table 5.1: Optical losses along the signal path at 0.69 THz (L$_{0.69THz}$) and 1.63 THz (L$_{1.63THz}$).

Component	L$_{0.69THz}$(dB)	L$_{1.63THz}$(dB)
Air path (50 cm)	0.03	0.55
Cryostat window (1 mm HDPE)	0.7	0.7
IR filter (2 Zitex™ sheets)	0.6	0.6
Si lens reflection	1	1
Total	2.33	2.85

state could be achieved by a heavy pumping of HEB with the LO. For a HEB in a normal state an output power is determined mostly by the thermal noise with an effective temperature which is equal to the electron temperature of HEB in this state (i.e. about T_c). In both reference states, an output power of the receiver is determined by a sum of the reference and the IF chain noise temperatures:

$$U = \frac{2 \ G_{tot} \ (T_{rec} + T_{295K})}{T_{IF} + T_{REF}} \tag{5.4}$$

In this case the mixer conversion gain could be calculated as:

$$G_m = G_{tot} \ L_{opt} = \frac{U \ (T_{IF} + T_{REF})}{2 \ (T_{rec} + T_{295K})} L_{opt} \tag{5.5}$$

Using Equations 2.12 and 5.3, Equation 5.4 could be rewritten as:

$$U = \frac{T_{out} + T_{IF} + 2 \ G_{tot} \ (T_{opt} + T_{295K})}{T_{IF} + T_{REF}} \tag{5.6}$$

Finally, the mixer output noise temperature becomes:

$$T_{out} = U \ (T_{IF} + T_{REF}) - T_{IF} - 2 \ G_{tot} \ (T_{opt} + T_{295K}) \tag{5.7}$$

Another way to obtain the mixer conversion gain and the output noise temperature is to calculate it directly from the IF response of HEB mixer at an operation state:

$$P_{out} = k_B \ B \ (T_{295K} + T_{rec}) \ \frac{2 \ G_m \ G_{IF}}{L_{opt}} \tag{5.8}$$

where G$_{IF}$ is an IF chain gain. If both the gain and the noise temperature of the IF chain are well known, the mixer conversion gain could be derived from Equation 5.8 as:

$$G_m = \frac{P_{out} \ L_{opt}}{2 \ k_B \ B \ (T_{295K} + T_{rec}) \ G_{IF}} \tag{5.9}$$

In this case, the mixer output noise temperature is:

$$T_{out} = \frac{P_{out} \ L_{opt}}{2 \ k_B \ B \ G_{IF}} - T_{IF} - \frac{2 \ G_m \ (T_{295K} + T_{opt})}{L_{opt}} \tag{5.10}$$
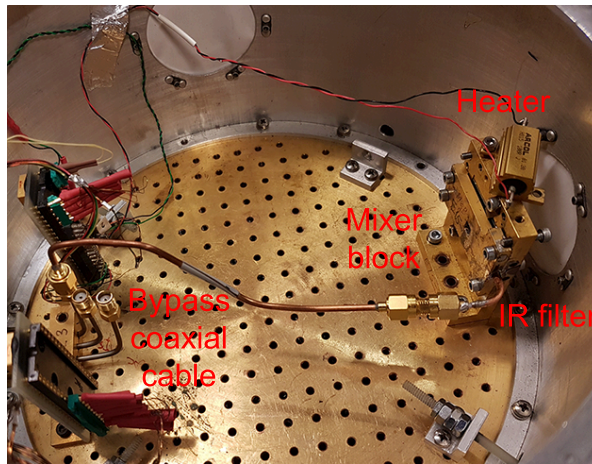
(a)
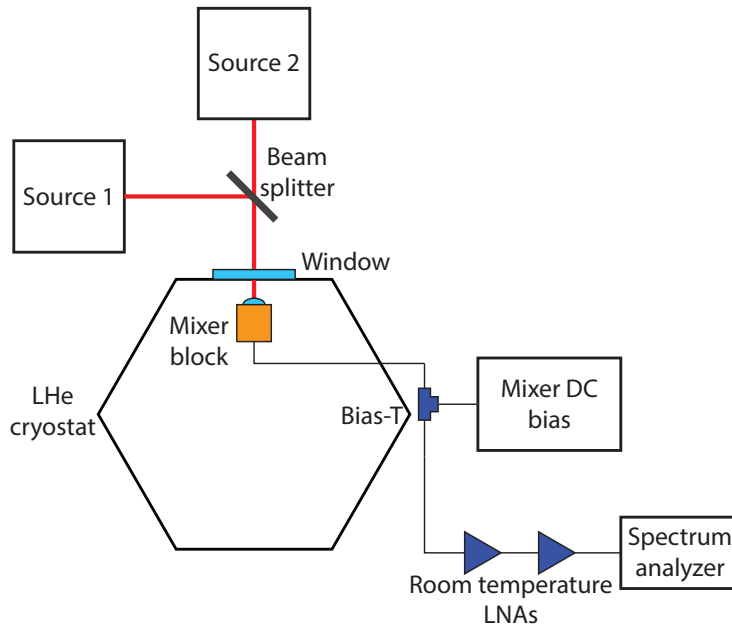
(b)

Fig. 5.4: Mixer GBW characterisation. (a) The cold plate of LHe cryostat. (b) The schematic of measurement setup.

5.2 GBW characterisation

For GBW measurements, MgB_2 HEB mixers were mounted in a mixer block with a 12 mm elliptical Si lens (see Figure 5.1(b)). The mixer block was placed in the LHe cryostat just in front the cryostat window. The mixer block output was connected directly to the cryostat output bypassing both the bias-T and the cryogenic LNA (see Figure 5.4(a)). The same resistive heater was mounted on the mixer block to perform measurements at elevated bath temperatures.

The full measurent setup schematics is presented in Figure 5.4(b). Radiation from two sources was combined using the Mylar® beam splitter. The frequency of Source 1 was fixed while the frequency of Source 2 was tuned. Either the FIR laser at 0.69 THz line or the backward wave oscillator (BWO) at 0.4 THz were used as a fixed frequency source. SD based frequency multiplier sources for corresponding frequency were used as a tunable frequency source. For GBW measurements at 0.1 THz, a Gunn diode source and a tunable high-electron-mobility transistor (HEMT) based frequency multiplier source were utilized. Signals from both sources were mixed by rectangular waveguide directional coupler with a horn antenna at the output for quasi-optical coupling of combined radiation into the receiver. Another broadband (20 kHz–45 GHz) bias-T was placed outside the cryostat to apply a voltage bias to the device and to separate the IF response. Two broadband MITEQ (0.1–20 GHz) LNAs followed the bias-T. The amplified mixing signal P_{IF} was measured with a spectrum analyser:

$$P_{IF} = P_s \; \frac{1}{L_{opt}} \; G_m \; G_{IF} \tag{5.11}$$

The gain of entire IF chain (except for the mixer unit) was measured with a noise figure analyser. Variation of tunable THz sources output power was measured both with HEB direct detection response on amplitude modulated THz signal and the Golay cell. After measurements, both calibrations were applied to recorded curves in order to obtain the IF response of HEB mixers themselves.

5.3 S/N ratio characterisation

The mixer characterisation using the Y-factor technique is practical for noise temperatures less than 10 000 K (Y = 0.1 dB). For lower Y-factor values the stability of the LO source becomes more critical. Device characterisation well outside the optimal bias regions and LO pumping levels (and at bath temperatures close to the T_c) becomes problematic without proper LO source stabilization. Therefore, heterodyne mixing was utilized in order to measure mixer signal to noise (S/N) ratio, which could be done in a broader conditions range. The experiments were performed using the FIR gas laser at 0.69 THz as an LO. The Schottky diode based frequency multiplier source was used as a signal source. The absolute power of the signal source (including mixer-to-source beam mismatch losses) was of no importance at that stage. However, the output power of the signal source was kept constant during experiments. After the cryogenic LNA, the IF signal was split into two branches outside the cryostat: 1) with the room temperature LNAs and the band-pass YIG-filter
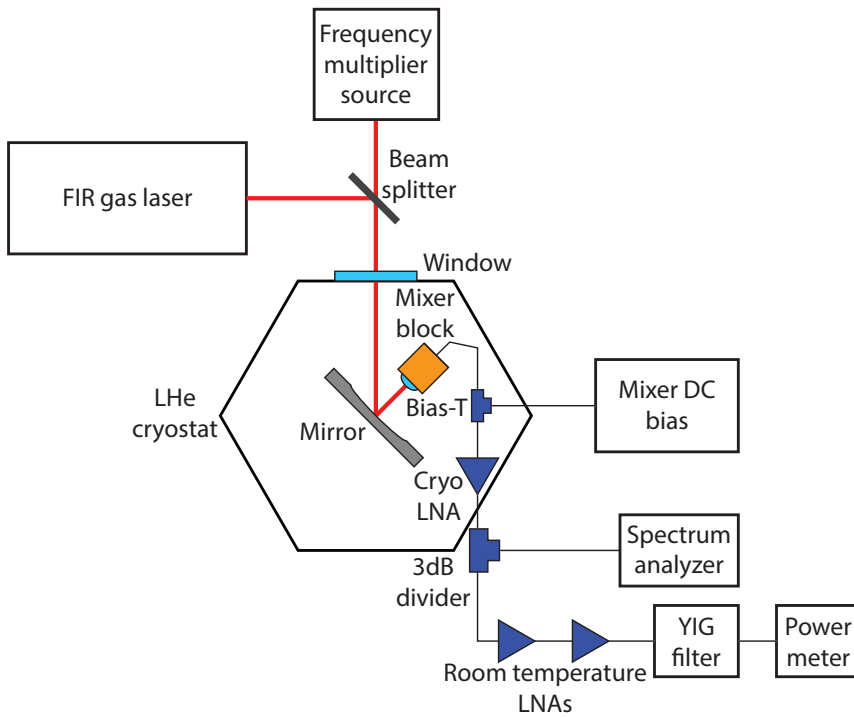
Fig. 5.5: Schematic of measurement setup for S/N ratio characterisation.

(for output noise measurements); and 2) directly fed into the spectrum analyser (for mixing signal measurements). The YIG-filter was set at 2 GHz. In order to exclude any effect from the signal source on the output noise measurements the signal source frequency was detuned by 2.5 GHz from the LO.

The mixing signal P_{IF} was recorded along with the receiver output noise power P_{out} for the same operation points. Since the incident power from the signal source, the optical losses, and the IF chain gain were constant through the experiments, variation of the P_{IF} are due to changes of the mixer gain (see Equation 5.11). Therefore, the mixer gain (in relative units) can be compared at different LO pumping levels and bath temperatures.

By using Equations 2.12 and 5.3, Equation 5.8 could be rewritten as:

$$P_{out} = k_B \ B \ (\frac{2 \ G_m \ T_{295K}}{L_{opt}} + T_{out} + \frac{T_{IF}}{G_{IF}}) \ G_{IF} \qquad (5.12)$$

In case of $T_{IF} \ll T_{out}$, the receiver output noise is mostly proportional to the mixer output noise temperature (see Equation 5.12). The S/N ratio then is calculated as:

$$S/N = \frac{P_{IF}}{P_{out}} \qquad (5.13)$$

Chapter 6

MgB$_2$ HEBs THz characterisation results

This chapter summarises the results on THz characterisation of MgB$_2$ HEB mixers fabricated from both MBE and HPCVD grown MgB$_2$ superconducting thin films. The results are presented in [Paper A], [Paper B], [Paper D], [Paper E], [Paper F], [Paper G], and [Paper H].

6.1 Devices fabricated from MBE grown films

6.1.1 DC characterisation

One device from each of the three batches B14, N1, N3 was chosen THz characterisation (see Table 6.1). HEB B14-1 discussed below was 10 nm thick and 1×1 μm^2 in size with a T$_c$ of 8.5 K. HEB N3-2 was 20 nm thick and 1×0.2 μm^2 in size with a T$_c$ of 22.5 K. HEB N1-2 was 20 nm thick and 1×0.5 μm^2 in size with a T$_c$ of 22 K. The resistance versus temperature (R-T) curves (see Figure 6.1(a)) were measured in a dip-stick for all HEBs. The devices were biased at
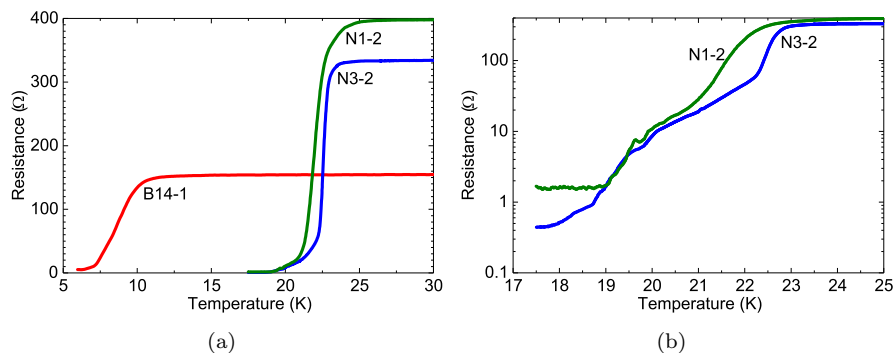

(a) (b)

Fig. 6.1: R-T curves (a) for HEBs B14-1, N1-2, and N3-2 and (b) in logarithmic scale for HEBs N1-2 and N3-2. *(Data adopted from [Paper B])*

Table 6.1: MBE MgB$_2$ HEB thickness (d), size (W×L), critical temperature (T$_c$), resistance at room temperature (R$_{295K}$), resistivity (ρ_{295K}), and critical current density (J$_c$). *(Data adopted from [Paper A] and [Paper B])*

Device	d(nm)	W×L (μm^2)	T$_c$(K)	R$_{295K}$(Ω)	ρ_{295K} ($\mu\Omega$cm)	J$_c$ (10^7A/cm^2)
B14-1	10	1×1	8.5	160	160	0.7
N1-2	20	1×0.5	22.0	400	850	5.5
N3-2	20	1×0.2	22.5	330	1650	5.0

a constant current (typically $10\,\mu$A) and cooled down from room temperature (295 K) to the LHe temperature (4.2 K). The 10 nm and 20 nm films used for device fabrication were from different batches deposited under different conditions, which affected the film quality. The presence of the double transition on R-T curves for devices N3-2 and N1-2 (see Figure 6.1(b)) suggests that the electrical contact between MgB$_2$ and Au was rather good (the proximity effect) [191]. One order of magnitude higher sheet resistance for the 20 nm thick devices could be explained by the fact that both surface roughness and film inhomogeneity start to play a significant role for devices with submicron dimensions. The resistivity measured in HEBs N3-2 and N1-2 is also one order of magnitude higher than values reported for 20 nm MBE films previously (100–200 $\mu\Omega \times cm$) [181]. Device B14-1 had much smaller critical current density than two other devices, which together with a lower T$_c$ suggests poorer film quality. The critical current density measured in device B14-1 is in the same ballpark as values reported for devices of similar size [124], while the critical current densities measured in devices N3-2 and N1-2 are of one order of magnitude higher because of the rapid annealing used for the film fabrication [181].

Results of DC measurements are very different from the data acquired with the devices fabricated from HPCVD grown films (see Chapter 3). The resistivity of these 10–20 nm films was much smaller (50–90 $\mu\Omega$cm), whereas critical current density was higher ((2–12)×10^7 A/cm^2 in submicron size bridges).

6.1.2   Direct detection characterisation

Some preliminary pumping tests of HEB N1-2 were conducted prior to the noise measurements in order to study the effect of THz radiation on the device. For pumping experiments, the cryostat was placed directly in front of the FIR gas laser front panel. The I-V curves for HEB N1-2 are given in Figure 6.2. The mixer was pumped to the I-V curve close to the optimum with the total available LO power estimated to be $\sim$100 μW in front of the cryostat (Curve 3 in Figure 6.2(a)). A high T$_c$ of 22-23 K according to the BCS theory corresponds to 8 meV σ-gap (or 1.9 THz, $2\Delta = \hbar\omega$, where $\hbar$ is the Dirac constant), where a conduction prevails for dirty samples [192,193]. However, at 1.63 THz the switching similar to the one of NbN devices under the pumping at frequencies below the superconducting gap frequency was not observed. It was demonstrated experimentally, that for the MgB$_2$ thin film in dirty limit with a T$_c$ as high as 33 K absorption of radiation occurs in a superconducting gap
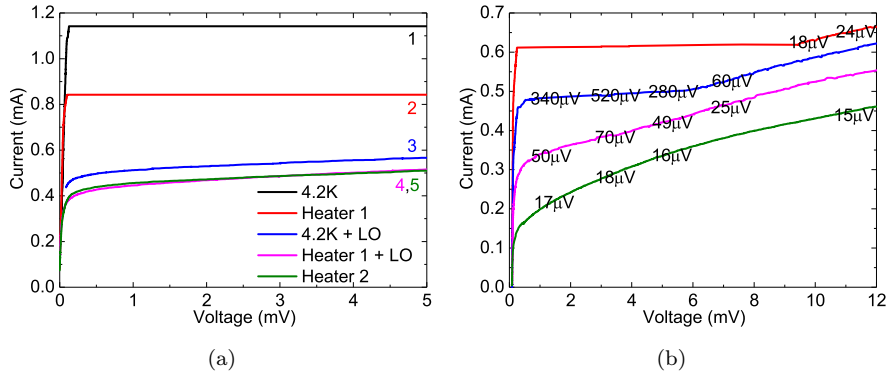
Fig. 6.2: I-V curves for HEB N1-2. (a) Curve 1: 4.2 K without LO pumping; Curve 2: Heater 1 without LO pumping; Curve 3: 4.2 K the maximum LO pumping; Curve 4: Heater 1 with the maximum LO pumping; Curve 5: Heater 2, the heating was increased until curve 5 coincided with curve 4. (b) The numbers in the field represent the voltage response on the lock-in amplifier at 1.63 THz. *(Data adopted from [Paper A])*

of 1.3 THz [194]. Curves 4 (2) correspond to the increased bath temperature with (without) LO pumping, respectively. For Curve 5 LO was switched off and a bath temperature was further increased by the resistive heater until it overlapped with Curve 4. The identity of Curves 4 and 5 demonstrate that 1.63 THz radiation has the same effect on a HEB as the rise of a bath temperature.

Direct detection experiments were performed in order to estimate which I-V curve corresponds to the HEB's maximum sensitivity to the THz radiation. The voltage response of HEB N1-2 on amplitude modulated THz radiation was recorded for a set of bath temperatures and bias points (see Figure 6.2(b)). The FIR gas laser radiation was attenuated by $\sim$20 dB to reach a small signal limit, when the THz radiation has no visible effect on I-V curves. The FIR gas laser radiation was modulated with the chopper 20 Hz. With the HEB in a current biased mode, a lock-in amplifier with a separate voltage pre-amplifier was used to measure voltage response of the HEB. The maximum responsivity was achieved at bias points ranging from 2 mV to 4 mV and from 0.3 mA to 0.5 mA, i.e. at 25-35% of the critical current at 4.2 K. Taking into account optical losses, the maximum responsivity at 1.63 THz can be estimated to be in a range of 1–2 kV/W.

6.1.3 Mixer sensitivity characterisation

HEB B14-1 had a T_c of 8.5 K, relatively low for MgB_2. Therefore, this device could be directly compared to NbN HEBs. LO pumped I-V curves of B14-1 at both 4.2 K and 2 K are presented in Figure 6.3. The minimum DSB receiver noise temperature corrected for optical losses versus the IF for device B14-1 at 4.2 K is presented in Figure 6.4(a). The I-V curves of B14-1 under LO pumping at 2 K are presented in Figure 6.3(b). The reduction of bath
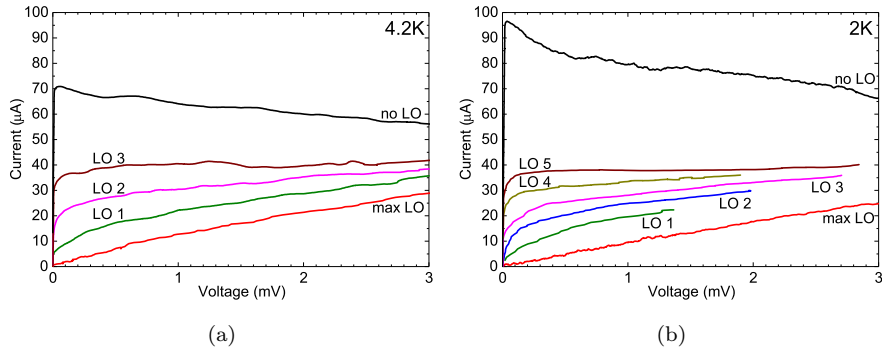
Fig. 6.3: (a) I-V curves for HEB B14-1: under 1.63 THz LO pumping (a) at 4.2 K (LO2 is an optimal I-V curve) and (b) at 2 K (LO3 is an optimal I-V curve). *(Data adopted from [Paper B])*
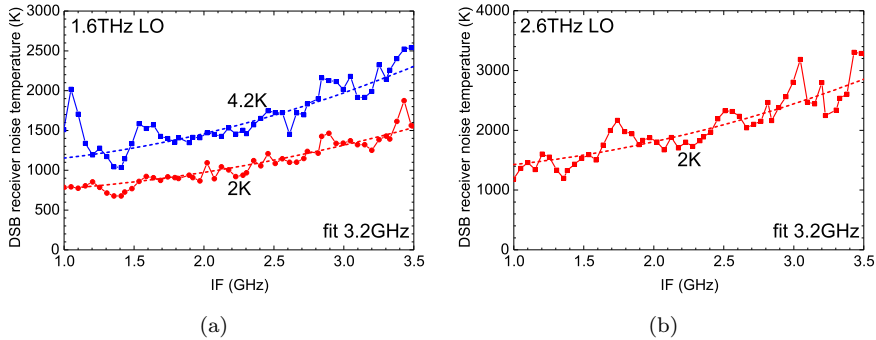

Fig. 6.4: DSB receiver noise temperature corrected for optical losses versus IF for HEB B14-1 (a) at 1.63 THz (the bias points are $U_0 = 0.8$ mV $I_0 = 28\,\mu$A at 4.2 K and $U_0 = 1.3$ mV $I_0 = 23\,\mu$A at 2 K) and (b) 2.6 THz (the bias point is $U_0 = 1.38$ mV and $I_0 = 31\,\mu$A at 2 K). *(Data adopted from [Paper B])*

temperature resulted in a ∼30% increase of the critical current and a ∼30% reduction of the receiver noise temperature (see Figure 6.4(a)). The corrected DSB noise temperature acquired with Y-factor measurements for HEB B14-1 was fitted with Equation 2.28. The values of $T_m(0)$ and f_N obtained from a fit are 1050 K and 3.2 GHz for 4.2 K; 700 K and 3.2 GHz for 2 K.

The LO power, required to reach the minimum receiver noise temperature, was calculated using the isotherm method (LO2 curve in Figure 6.3(a)) was 70 nW. The isotherm method assumes that both DC and LO powers have similar effect on HEB resistance [149]. At 2 K the required LO power was estimated to be 80 nW. The LO power required for the minimum noise is in the same ballpark as one reported for NbN HEB mixers.

The available LO power was enough to pump the device into the normal state and to perform U-factor measurements. The noise temperature of the IF chain was determined by the noise temperature of the first LNA which was

Table 6.2: Mixer conversion gains (G_m) and output noise temperatures (T_{out}) for HEB B14-1 at f_{IF} = 1.8 GHz calculated using Equations 5.5 and 5.7 with superconducting and normal reference states, and using Equations 5.9 and 5.10. *(Data adopted from [Paper B])*

	"superconducting"		"normal"		"gain"	
T_{bath}(K)	G_m(dB)	T_{out}(K)	G_m(dB)	T_{out}(K)	G_m(dB)	T_{out}(K)
4.2	-19.1	31	-19.6	27	-19.9	26
2	-18.2	21	-18.1	22	-18.9	18

mounted on the cryostat's cold plate. The gain of this LNA was 30 dB and the noise temperature was ≈2 K. For the whole IF chain the noise temperature was estimated to be not exceeding 3 K. The total gain of the IF chain, used for the gain method calculation, was 77 dB at 1.8 GHz.

At 4.2 K, at the optimal operation point of U_0 = 0.8 mV I_0 = 28 µA the U-factor was 8.2 dB for the superconducting state reference and 4.7 dB for the normal state reference. An uncorrected DSB receiver noise temperature of 2500 K and T_{REF} = 9 K were taken for calculation uzing Equations 5.5 and 5.7. At 2 K, the following values were used for the mixer conversion gain and the output noise calculation (U_0 = 1.3 mV I_0 = 23 µA bias point): U-factor for a superconducting state reference of 7.2 dBm, U-factor for a normal state reference of 4.2 dBm, a receiver noise temperature of 1500 K and T_{REF} = 9.3 K. Mixer conversion gains and output noise temperatures, calculated using all three methods, are summarized in Table 6.2. The values obtained by all three methods are very close to each other, which can be interpreted as a confirmation of reliability. While changing the bath temperature from 4.2 K to 2 K the mixer conversion gain increased by ~1 dB, whereas the mixer output noise temperature decreased by 5–10 K. Both of these facts lead to a decrease of the receiver noise temperature. It is of interest to compare this device to a NbN HEB mixer since T_cs are quite close. The reported conversion gain for NbN HEB was -12 dB with a mixer output noise temperature of about 40 K [94, 139]. The U-factor measurements for HEB B14-1 were performed at a 1.8 GHz IF which is quite close to the 3-dB roll-off frequency. Therefore, a correction of about +2 dB should be applied. The receiver noise temperatures and NBWs are in the same ballpark.

Characterisation of MgB$_2$ HEBs with a higher T_c, in a mode where LO frequency is higher than superconducting gap frequency, requires operation at higher bath temperatures or utilization of LO sources with higher frequencies. Therefore, preliminary Y-factor measurements were performed with HEB B14-1 at 2.6 THz and 2 K. The available output power from the FIR gas laser at this frequency was lower compared to 1.63 THz but still enough to pump the device. The DSB receiver noise temperature versus the IF (U_0 = 1.38 mV I_0 = 31 µA) is presented in Figure 6.4(b). The fit with Equation 2.28 gives a zero IF noise temperature of 1250 K and NBW of 3.2 GHz. At 2.6 THz, the receiver noise temperature of HEB B14-1 appeared to be higher compared to a 1.63 THz LO.

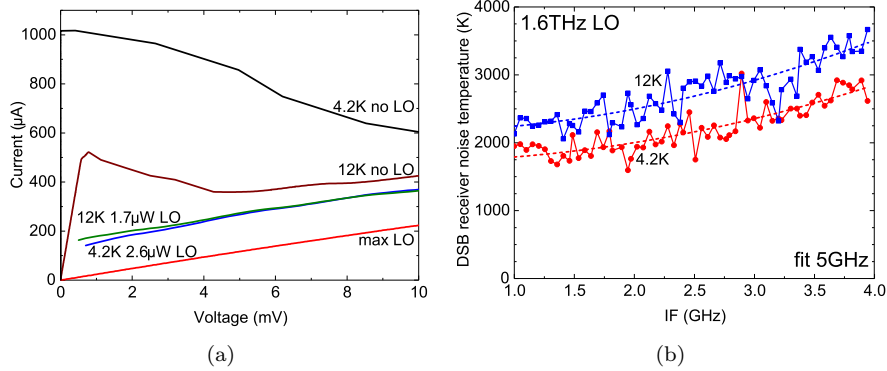The same experimental setup was used for HEB N3-2 characterisation and

(a)   (b)

Fig. 6.5: (a) I-V curves for HEB N3-2 with (without) 1.63 THz LO at 12 K and 4.2 K. (b) DSB receiver noise temperatures corrected for optical losses versus IF for HEB N3-2 at 1.63 THz and, 4.2 K(circles) and 12 K (squares). The bias points are U$_0$ = 1.6 mV I$_0$ = 180 μA and U$_0$ = 1.8 mV, I$_0$ = 200 μA, respectively. *(Data adopted from [Paper B])*

a thin plastic film was placed between the mixer block and the cryostat cold plate to minimize a LHe boiling rate during "heated" tests. The I-V curves for HEB N3-2 at 4.2 K and 12 K with and without 1.6 THz LO pumping are presented in Figure 6.5(a). At a bath temperature of about 12 K the HEB critical current has reduced to the half of its value at 4.2 K. The required LO power for the minimum noise operation at 12 K is 1.7 μW compared to 2.6 μW at 4.2 K. The measured receiver noise temperatures across a 1–4 GHz IF band for bath temperatures of 4.2 K and 12 K fitted with Equation 2.28 are presented in Figure 6.5(b). Measurements were performed at bias points of U$_0$ = 1.6 mV I$_0$ = 180 μA and U$_0$ = 1.8 mV, I$_0$ = 200 μA for 4.2 K and 12 K, respectively. At certain IFs the mixer response on a hot-cold load was unstable, which resulted in errors in noise temperature measurements (e.g. at 3.2 GHz for 12 K and 1.9 GHz, 2.9 GHz for 4.2 K). The corrected receiver noise temperature increased from 1700 K to 2150 K with an increase of bath temperature but a NBW of 5 GHz remained unchanged.

A direct measurement of GBW at frequencies >1 THz is problematic due to a low availability of coherent sources with a tunable frequency. One of the possible solutions is a use of BWOs or multiplier sources with frequencies <1 THz. For NbN HEB mixers made from ultrathin films a typical critical temperature is about 9 K. This T$_c$ gives a superconducting gap frequency of about 0.6 THz at 4.2 K. Hence, NbN devices work with mentioned power sources in the regime where the LO frequency is higher than the gap frequency. Consequently, this mixing experiments could be extrapolated to higher frequencies. For devices with a high T$_c$ (and hence, large superconducting gap) such low frequency mixing experiments can not be extrapolated to higher frequencies because of slightly different mechanism of mixer operation. In this case, low frequency THz radiation is absorbed only in a normal domain of HEB bridge where a superconducting gap is suppressed by a DC power. Instead of mixing experiments for N3-2 U-factor measurements were performed across the IF band in
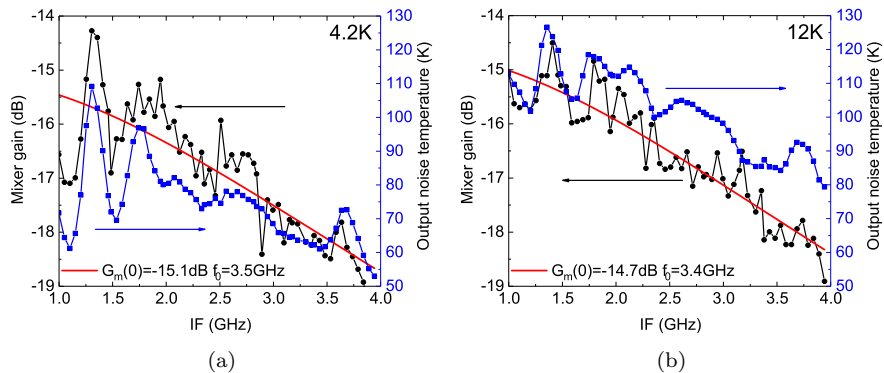
Fig. 6.6: Conversion gain (circles) and output noise temperature (squares) versus the IF for HEB N3-2 at 1.63 THz and (a) 4.2 K, $U_0 = 1.6$ mV $I_0 = 180\,\mu$A and (b) 12 K, $U_0 = 1.8$ mV, $I_0 = 200\,\mu$A. *(Data adopted from [Paper B])*

order to extract the GBW. Moreover, this method provides both the mixer conversion gain and the output noise temperature. The results of U-factor measurements for 4.2 K and 12 K are presented in Figure 6.6. Higher ripples for IFs <1.5 GHz correspond to the region of LNA's high return loss. Experimental data were fitted with Equation 2.20. The zero IF mixer conversion gain and the GBW achieved from the fit are -15.1 dB and 3.4 GHz; -14.7 dB and 3.5 GHz at 4.2 K and 12 K, respectively. The HEB shows almost the same conversion gain and GBW at both bath temperatures, but the output noise at 12 K is higher, which resulted in a higher receiver noise temperature. The similar effect of bath temperature was observed for HEB B14-1.

6.2 Devices fabricated from HPCVD grown films

6.2.1 Gain bandwidth characterisation

GBW measurements were performed at three LO frequencies of 0.1 THz, 0.4 THz, and 0.69 THz. The first two frequencies were expected to be below the superconducting gap frequency at 4.2 K, so the tested HEBs were heated up to 25–35 K in order to suppress the superconducting gap. The GBW was observed to be almost independent on both the bias voltage and the bath temperature. The higher output power of 0.1 THz LO allowed for GBW measurements of thicker devices at a wider range of bath temperatures and device sizes. Figure 6.7 presents I-V curves measured in LHe cryostat and the mixing signal at 0.1 THz for 30 nm thick HEB E2-2 with a T_c of 39.5 K. The mixing signal curves taken at different bias points and bath temperatures coincide perfectly. HEBs E3-8 (20 nm thick, $T_c = 38.5$ K) and E6-4 (12 nm thick, 33.5 K) were tested at various LO frequencies. Figure 6.8 demonstrates that the GBW of these devices is independent on the LO frequency at least in 0.1–0.69 THz range.

The summary of GBW measurements performed for the HEBs of various thickness is plotted in Figure 6.9. A GBW of 6.8 GHz was observed for HEB
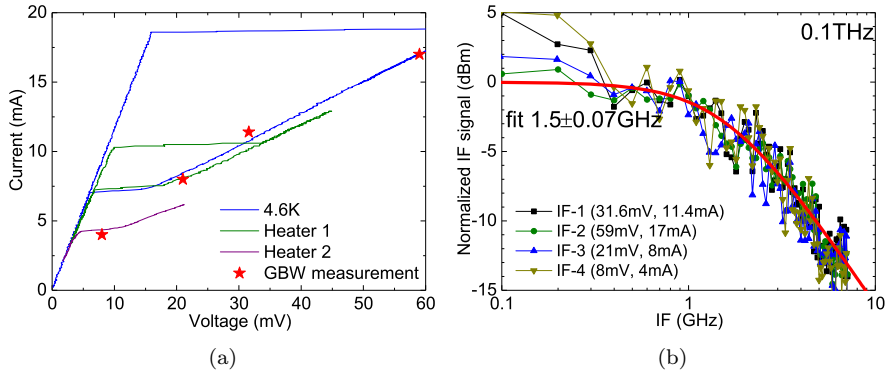
Fig. 6.7: GBW of HEB E2-2 (30 nm thick, $T_c = 39.5$ K). (a) I-V curves measured in LHe cryostat at various bath temperatures and (b) mixing signal at 0.1 THz at various bias points. *(Data adopted from [Paper E])*
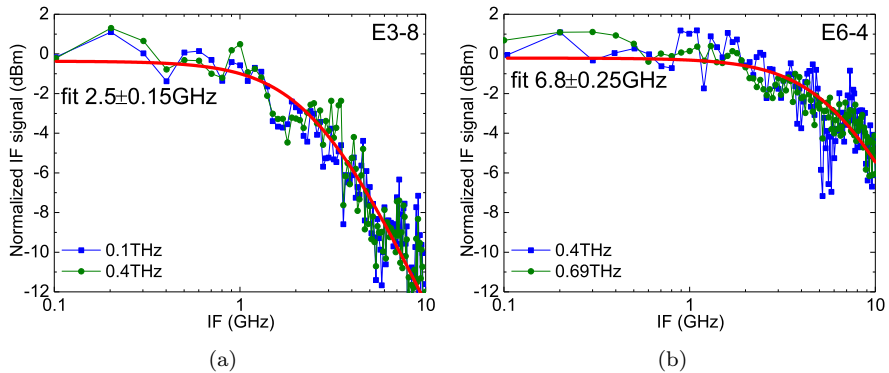

Fig. 6.8: GBW of HEBs (a) E3-8 (20 nm thick, $T_c = 38.5$ K) at 0.1 THz and 0.4 THz LOs and (b) E6-4 (12 nm thick, $T_c = 33.5$ K) at 0.4 THz and 0.69 THz.
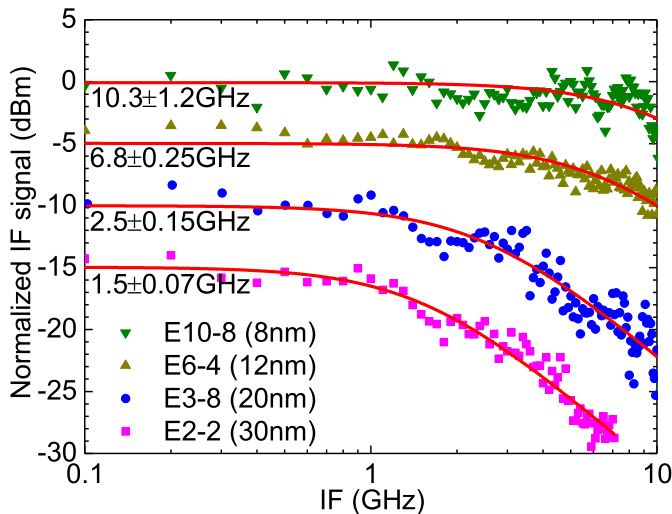
Fig. 6.9: Normalized IF signal of four MgB$_2$ HEB mixers measured at 0.1 THz (E2-2), 0.4 THz (E3-8), and 0.69 THz (E6-4, E10-8).

Table 6.3: HPCVD MgB$_2$ HEB thickness (d), critical temperature (T$_c$), GBW, time constant (τ), electron and phonon heat capacities ratio (c$_e$/c$_{ph}$) and critical current density (J$_c$)

Device	d(nm)	T$_c$(K)	GBW (GHz)	τ(ps)	c$_e$/c$_{ph}$	τ_{ep}(ps)	τ_{esc}(ps)
E2-2	30	39.5	1.5±0.1	106	0.57	3.5±1	22±2
E3-8	20	38.5	2.5±0.15	64	0.59	4±1	20±1.5
E6-4	12	33.5	6.8±0.25	24	0.73	5±0.5	5±0.5
E10-8	8	31.0	10.3±1.2	16	0.82	6±0.2	3±1

E6-4 made from the 12 nm thick MgB$_2$ film. The GBW is about 2-3 times larger than for typical phonon-cooled NbN HEB mixers made from 3–5 nm thick NbN films. The critical temperatures of the discussed HEBs were in the range of 30–40 K where similar electron-phonon interaction times are expected. Therefore, the increase of GBW for thinner films is expected to be defined mostly by the reduction of the phonon escape time.

In order to estimate these characteristic times, a fit to experimental data was done with the 2-T model (see Chapter 2) similar to Ref. [124]. The same Debye temperature (750 K) and electron specific heat (3 mJ/mol K^2) were used for fitting. The HEB parameters and the results are summarized in Table 6.3. The characteristic times follow expected trends (an increase of electron-phonon interaction time and a reduction of escape time). The estimated phonon escape times are twice shorter compared to the escape times measured for HEBs fabricated from MBE grown films [124] suggesting a better acoustic matching at a film/substrate interface. It is obvious that in order to archive more reliable results for device thinner than 10 nm measurements should be performed up
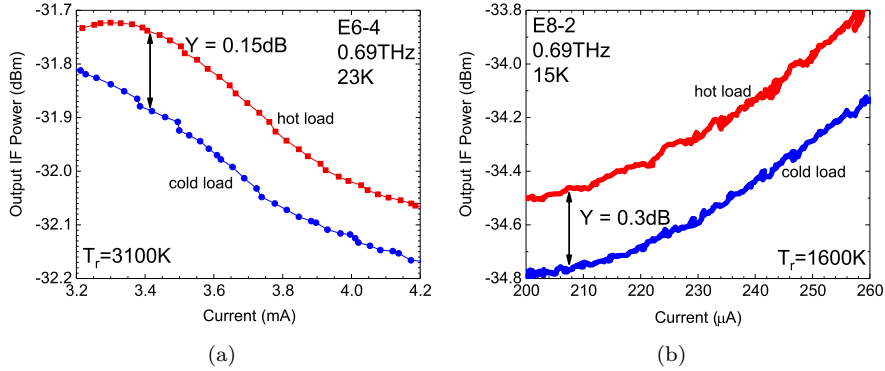
Fig. 6.10: DSB receiver noise temperature measured by Y-factor technique for HEBs (a) E6-4 and (b) E8-2. *(Data adopted from [Paper D] and [Paper F])*

to higher IFs (at least 20 GHz), which requires a fabrication of a new mixer block and a re-calibration of the whole IF chain.

6.2.2   Mixer sensitivity characterisation

6.2.2.1   Initial results

The GBW characterisation provides some useful information about potential devices performance. However, it was not the main goal of the study since the ultimate characteristics of HEB mixers are receiver noise temperature and NBW. At first stages, sensitivity characterisation was challenging. Initial devices were made from films thicker than 10 nm with high T$_c$s (close to the bulk value) and high critical current densities. For LO pumping to expected optimal I-V curves, a thick beam splitter (200 μm) with a high transmission loss was used. The available LO power was still not enough to pump the device at 4.2 K, so the bath temperature had to be raised above 20 K. The thick beam splitter and elevated bath temperatures used for device characterisation resulted in a quite high measured DSB receiver noise temperature of 6000 K (see Figure 6.10(a)) for HEB E6-4, which after applying correction for optical losses becomes 3100 K. Better results were achieved for batch E8 made from a 10 nm thick film. Corrected for optical losses DSB receiver noise temperature of 1600 K (see Figure 6.10(b)) was measured for HEB E8-2 with a T$_c$ of 32 K at 0.69 THz and 15 K. At 20 K the noise temperature increased to 2500–3000 K.

For HEB E8-7 the receiver noise temperature was measured versus the IF. Recorded I-V curves are shown in Figure 6.11(a). The I-V curve under the optimal LO power (the highest Y-factor) is IV-opt. The corresponding output IF power curve (Figure 6.11(a), PV-opt) varies with bias voltage with a maximum at about 0.5 mV. The lowest receiver noise temperature was obtained at bias voltages slightly above the maximum on the PV-opt curve (1–2 mV). In the normal state, I-V curve IV-norm is totally linear with a resistance of 50Ω equal to the resistance near the beginning of superconducting transition. The output IF power curve (PV-norm) is also bias independent indicating that the HEB is in a normal state. The noise temperature is approximately 2000 K in
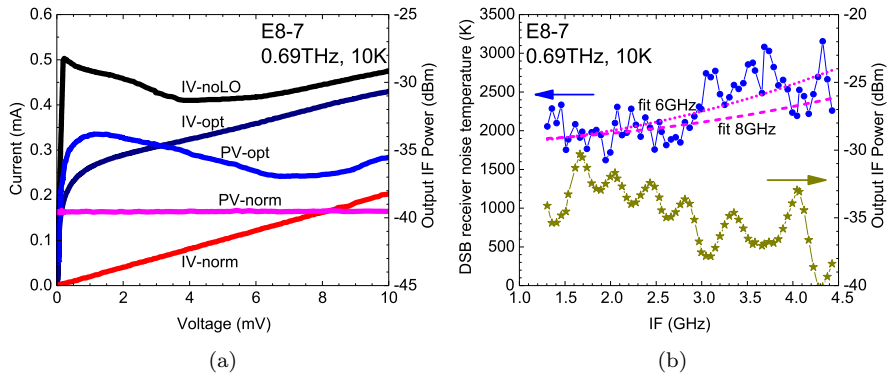
Fig. 6.11: HEB E8-7 (a) IV curves: IV-noLO - in the mixer block at 10 K; IV-opt - under the optimal LO power; IV-norm - pumped by the LO into the normal state. Output IF power versus bias voltage curves measured at 2 GHz: PV-opt corresponds to the optimal LO (IV-opt); PV-norm corresponds to the normal state (IV-norm). (b) DSB receiver noise temperature (circles) and the output power (stars) versus the IF. The dotted and dashed lines are fits for 6 GHz and 8 GHz NBWs, respectively. *(Data adopted from [Paper F])*

a 1.3–3 GHz IF range (see Figure 6.11(b)). The output IF power versus the IF curve exhibits some notches in 3–4 GHz range and at 4.3 GHz, which is also accompanied by the rise of noise temperature (see Figure 6.11(b)). It could be associated with the cryogenic LNA and leads to a reduced NBW of 6–8 GHz. For further measurements, the cryogenic LNA was replaced.

6.2.2.2 Low noise MgB$_2$ HEB mixers

Significant progress, comparing to the initial results, was achieved with MgB$_2$ HEB mixers $1\times1\mu m^2$ in size with a T$_c$ of 30 K fabricated from a 8 nm thick HPCVD grown film for which Ar$^+$ cleaning was applied (see Chapter 3). These devices had room temperature resistances of $\approx$200 Ω (see Figure 6.12). I-V curves for HEB E10-7 are given in Figure 6.13. Device E10-8 from the same batch had very similar critical current and I-V curves as for device E10-7. Therefore, further data would be given for HEB E10-7. Sheet resistance obtained from nanobridges was higher by a factor of 4 compared with sheet resistance measured on this film prior processing. The T$_c$ was reduced by 4 K. The Far Infrared (FIR) gas laser was used as a LO, with emission frequencies of 0.69 THz, 1.63 THz, and 2.56 THz. At 2.56 THz the output power was not sufficient to pump the mixer with a thin beam splitter (12.5 μm) and hence, it was only used with a mirror to record I-V curves. With the optimal LO (0.69 THz) power, I-V curves at 5 K, 15 K, and 20 K fully overlap each other, indicating that the LO power at 0.69 THz is absorbed independently of the temperature and the bias voltage (see Figure 6.13(a)). At 5 K, the shape of the IV curves did not depend on the LO frequency from 0.69 THz to 2.56 THz (see Figure 6.13(b)) suggesting that absorbtion of THz radiation occurs in the π-gap (smaller gap). The same IV curves were achieved by simply rising the bath temperature with the LO turned off. The shapes of the curves are similar
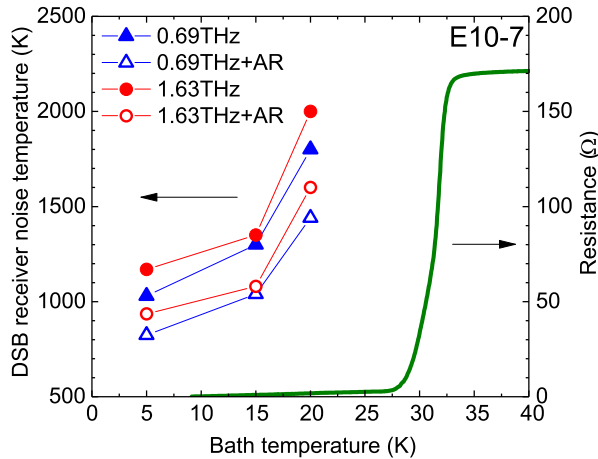
Fig. 6.12: R-T curve for HEB E10-7. Summary of the receiver noise temperature at 0.69 THz (triangles) and 1.63 THz (circles) LOs. Empty symbols are receiver noise temperatures corrected for Si lens losses. *(Data adopted from [Paper G])*

to those for NbN HEB mixers.

With the 0.69 THz LO, receiver noise temperature was measured using the Y-factor technique at various LO power levels and in a bias voltage range up to 25 mV. The corresponding set of I-V curves at 5 K (each relates to a certain LO power) is given in Figure 6.14(a). The receiver noise temperature measured along IV-3 is given in Figure 6.14(a) (filled dark blue squares, right ordinate). For a bias voltage of 7 mV the receiver noise temperature is shown as a function of bias current (magenta squares, top abscissa). The lowest noise temperature is obtained in a bias voltage range corresponding to the maximum output noise (5–10 mV). The bias point range for the lowest receiver noise temperature is marked with the red oval (IV-3 to IV-5). As the mixer temperature increases, the optimal LO power range shrinks. At 20 K the lowest receiver noise was achieved only around IV-3. For the given set of I-V curves, which excessively covers the optimal LO-bias voltage range, the mixer output noise (see Figure 6.14(b)) increases continuously as the LO power is reduced from the heavily overpumped state (IV-7) till the underpumped state (IV-1) is reached. The mixer gain starts to saturate just above IV-5, i.e. above the optimal bias zone. The resulting S/N ratio (see Figure 6.14(d)) has a maximum at curves IV-3 to IV-5. The (A-log(T_{rec})) for IV-3 is also plotted in Figure 6.14(d), where A is a fitting parameter for plotting. The logarithm of $1/T_{rec}$ follows closely the S/N ratio curve, as it is expected from Equation 5.13:

$$log(S/N) \approx log(\frac{P_{IF}}{k_B \ B \ T_{rec}}) \propto -log(T_{rec}) \qquad (6.1)$$

demonstrating that the bias voltage and LO power optimization for both S/N ratio and receiver noise temperature coincides across the I-V plane. This fact illustrates that, despite the broadband antenna is used for the HEB mixer, the direct detection effect (shift of the bias point due to the switch between hot and cold loads) does not have any impact on the choice of the mixer
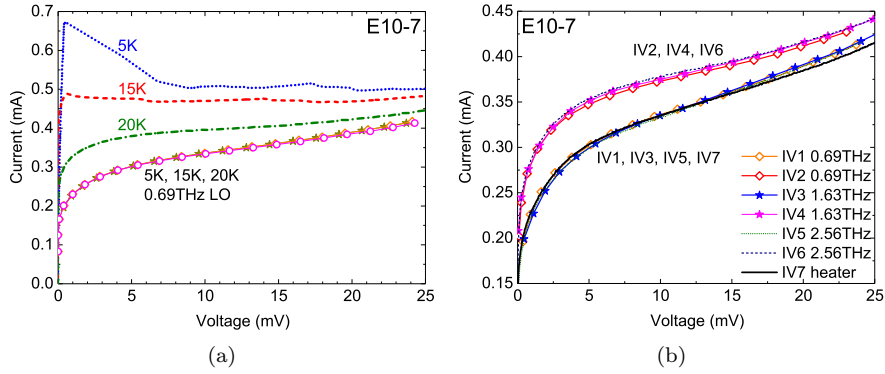
Fig. 6.13: HEB E10-7 I-V curves (a) in the cryostat at 5 K (no LO, blue solid), at 15 K (no LO, red dashed), at 20 K (no LO, green dash-dotted), three fully overlapping IV curves at the optimal LO power at 5 K, 15 K, and 20 K; (b) at different LO power levels (at 5 K): under the 0.69 THz, 1.63 THz, and 2.56 THz LO pumping, IV7 (black solid) at an elevated temperature without LO pumping. *(Data adopted from [Paper G])*
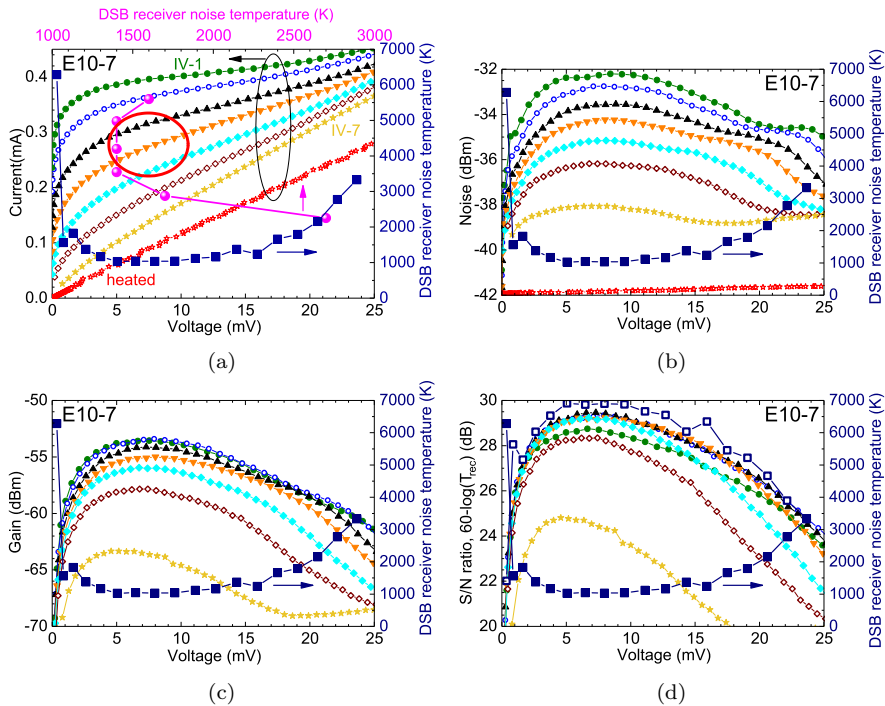
Fig. 6.14: HEB E10-7 with 0.69 THz LO pumping and at 5 K. The area of the highest S/N ratio is marked on the I-V plane. *(Data adopted from [Paper H])*
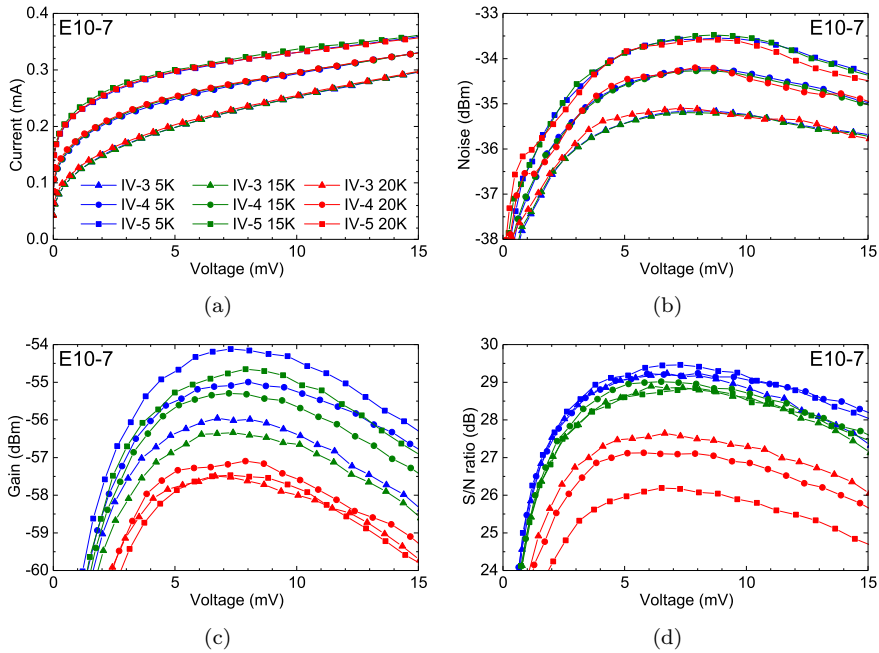
Fig. 6.15: Close comparison of the I-V, P$_{out}$-V, G-V, and S/N-V curves for HEB E10-7 (0.69 THz and 5 K, 15 K, and 20 K) at the bias voltages and LO power levels corresponding to the highest S/N ratio. *(Data adopted from [Paper H])*

operation point. In a 3 THz band, a black body at 295 K (77 K) emits $\approx$2.8 nW ($\approx$1.6 nW) in the single spatial mode [12]. This is $\approx$1% of a typical optimal LO power for NbN HEB mixers, and hence, this radiation has a significant impact on a mixer bias point especially at smaller bias voltages. For NbN HEB mixers this effect can either decrease or increase the apparent Y-factor (receiver noise temperature). However, for the discussed MgB$_2$ HEB mixers the direct detection effect is negligible.

The three sets of I-V curves at 5 K, 15 K, and 20 K (corresponding to IV-3, IV-4, and IV-5) are plotted in Figure 6.15(a). For the matching I-V curves, the output noise power versus bias voltage curves also totally overlap each other, which means that the mixer output noise temperature is independent on a bath temperature. In Figure 6.16(a), the output noise power at the same bias point (7 mV and 200 μA) is plotted as a function of bath temperature. In contrast to the output noise, mixer gain has decreased at higher temperatures (Figure 6.15(c)). The absorbed LO power was calculated using the isotherm method (see Figure 6.16(a)). The logarithm of absorbed LO power is plotted in Figure 6.16(a) (magenta diamonds) along with the mixer conversion gain (red squares). A reduction of mixer gain (by 2.5 dB) from 5 K to 20 K is proportional to a reduction of LO power (by 2.4 dB) for the given I-V curve, as it would be expected from the HEB mixer lumped element model. The logarithm of the receiver noise temperature follows exactly the same temperature trend as the S/N ratio (green triangles and filled stars in Figure 6.16(a)).
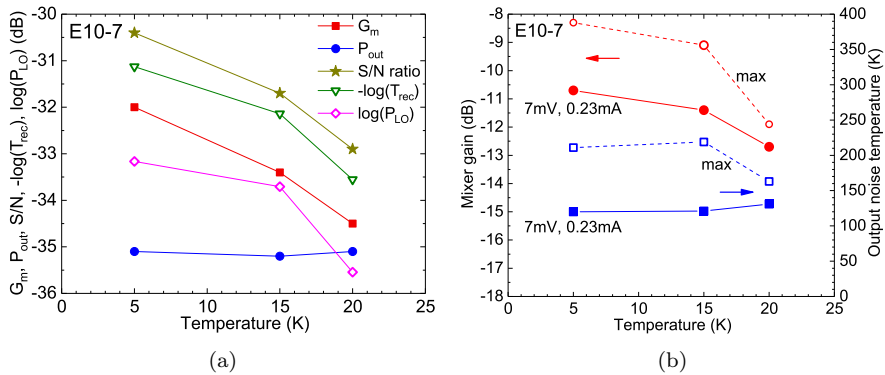
(a) (b)

Fig. 6.16: (a) Mixer gain (from mixing experiments) (red squares), mixer output noise (blue circles), S/N ratio (yellow stars), logarithm of $1/\text{T}_{rec}$ (empty green triangles), and logarithm of absorbed LO power (empty magenta diamonds) at 0.69 THz versus temperature. Mixer characteristics were measured at the same bias point (7 mV and 0.23 mA) for all bath temperatures. (b) Mixer gain and output noise temperature as a function of bath temperature (from U-factor technique). Filled symbols are at a 7 mV and 0.23 mA bias point. Open symbols are at the point of the maximum output noise temperature providing the same receiver noise temperature as at the discussed bias point. *(Data adopted from [Paper H])*

Mixer gain (filled circles) and output noise temperature (filled squares) calculated using the U-factor technique with a normal reference state are plotted in Figure 6.16(b) for 5 K, 15 K, and 20 K (all at the same bias point of 7 mV and 0.23 mA). Mixer gain is inversely proportional to the temperature, whereas output noise remains almost the same. This is also confirmed by the mixing experiment, as it can be seen in Figure 6.16(a). As follows from Figure 6.14(a) the receiver noise temperature is constant over quite a wide range of LO power. Across this range (IV5-IV3), both mixer gain and output noise vary by a factor of 2: from 120 K to 220 K and from -10.7 dB to -8.3 dB, respectively (see Figure 6.16(b)). Apart from a lower LO power, the operation at IV3 has an advantage of higher output noise. With an output noise of 220 K, the IF LNA noise becomes much less critical for the overall receiver noise temperature. This is particularly important for the broadband IF LNAs which optimization can now be focused on input matching (no need for an isolator) rather than on the noise. In Figure 6.16(b) both maximum output noise temperature and corresponding mixer gain (within the minimum receiver noise zone) are plotted for 5 K, 15 K, and 20 K mixer temperatures.

In order to obtain the HEB NBW, the noise temperature was measured across a wide IF band with a step of 50 MHz. Both 1.5–4.5 GHz and 1.0–9.0 GHz IF LNAs were used for the experiments. Measurements with the 1.5–4.5 GHz LNA were intended to verify whether HEB-LNA interference might be affecting obtained results. In Figure 6.17(a), the receiver noise temperature measured with the 1.5–4.5 GHz LNA at both 0.69 THz and 1.63 THz LOs is shown. The noise temperature increases proportionally over the whole IF range, indicating that NBW is the same at both LOs, and hence supporting
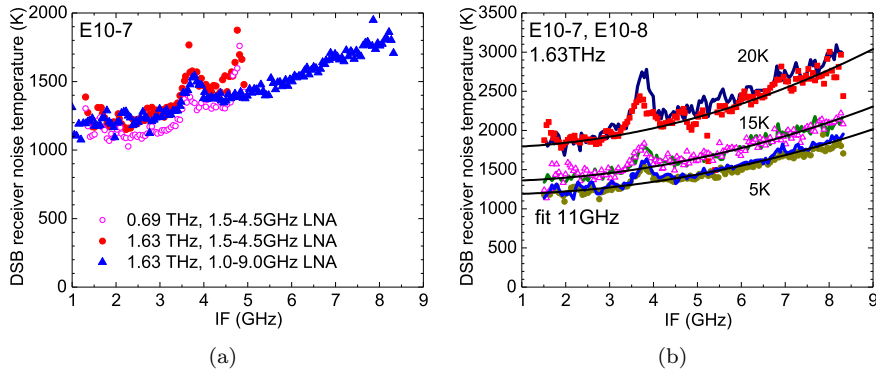
Fig. 6.17: (a) HEB E10-7 receiver noise temperature versus the IF recorded at 5 K. Filled symbols: 1.63 THz. Open symbols: 0.69 THz. Circles: 1.5–4.5 GHz LNA. Triangles: 1.0–9.0 GHz LNA. (b) The receiver noise temperature (at 1.63 THz) as a function of IF recorded at 5 K, 15 K, and 20 K. Results for HEBs E10-7 (line) and E10-8 (symbols) are shown. *(Data adopted from [Paper H])*

the idea of heterodyne response bolometric nature in discussed devices. The noise temperature at lower IFs as measured with the 1.5–4.5 GHz LNA fully overlaps with the data obtained using the 1.0–9.0 GHz LNA. The hump at 3.7 GHz is present at both data sets and originates from the bias-T used for experiments. The noise temperature spectrum at 1.63 THz was measured at 5 K, 15 K, and 20 K for both HEBs E10-7 and E10-8 (see Figure 6.17(b)). The fitting curves are for an 11 GHz NBW. The summary of measured receiver noise temperatures measured at both 0.69 THz and 1.63 THz LO frequencies is given in Figure 6.12. Considering a possible reduction of reflection losses at the Si lens by 20% with an anti-reflection coating the minimum noise temperatures at 5 K are 830 K (0.69 THz) and 930 K (1.63 THz). At 15 K, the noise temperature rises by 20% from its value at 5 K. At 20 K, the noise temperature rises by 75%. As it can be noticed, the noise temperature difference between 0.69 THz and 1.63 THz is about 12%, which is similar to the rate observed for NbN HEB mixers at higher LO frequency.

6.2.3   Further improvement

As it is demonstrated in Figure 6.16(a)), devices with a higher T$_c$ are needed in order to increase mixer gain and consequently improve noise performance at higher bath temperatures. HEB E15-7 with a T$_c$ of 33 K made from a 5 nm thick HPCVD grown MgB$_2$ film has demonstrated a lower noise temperature at 20 K compared to HEBs from batch E10 (T$_c$ = 33 K) (see Figure 6.18). For device E15-7, a significant increase of the noise temperature (2500 K) was observed only at 25 K. At 30 K, the noise temperature of 15 000 K was estimated using S/N ratio approach. In order to push further the high temperature operation of MgB$_2$ HEB mixers, devices with even higher T$_c$ have to be utilized. Most likely, it would be possible to achieve only by increasing the film thickness, which would lead to a NBW reduction. Another direction to improve
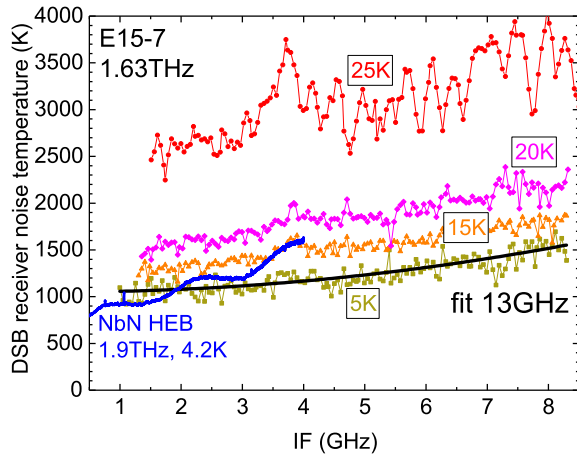
Fig. 6.18: HEB E15-7 receiver noise temperature (at 1.63 THz) versus the IF recorded at 5 K, 15 K, 20 K, and 25 K. The NbN HEB mixer data is from Ref. [32].
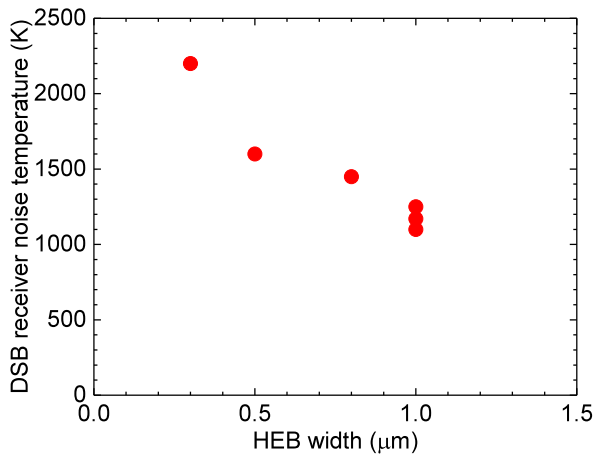
Fig. 6.19: MgB$_2$ HEB DSB receiver noise temperature versus HEB width.

MgB$_2$ HEB mixer noise performance is to decrease the contact resistance between the film and Au antenna. The observed dependence of noise temperature on device width (see Figure 6.19) suggests that the contact resistance has a significant contribution. The contact resistance might be reduced either by increasing HEB width, which will, unfortunately, lead to increase of required LO power, or by changing the fabrication procedure to improve the film/antenna contact.

However, MgB$_2$ HEB mixer already demonstrate noise performance comparable with state-of-the-art NbN HEB mixers but with a three times larger NBW (see Figure 6.18). Despite NbN HEB mixers can have lower noise temperature than the discussed MgB$_2$ HEB mixers at IFs below 1 GHz, the noise temperatures averaged over the IF bandwidth are in the same ballpark.

Chapter 7

Conclusion and future outlook

In this thesis, study of the novel HEB mixers for THz frequencies based on MgB_2 thin films have been discussed. **MgB_2 HEBs of submicron sizes were fabricated and characterised at THz frequencies.** Transition to submicron sizes has reduced LO power requirements and allowed for the pumping of MgB_2 HEBs to optimal I-V curves at the LHe temperature using available FIR gas laser. **Study of HEBs made from MBE grown MgB_2 films shows that both the output noise temperature and the conversion gain of HEB mixers are proportional to the T_c.** This is valid for the optimal operation conditions: optimal LO power and DC bias. At the same time, utilization of films with a higher T_c results in a broader NBW. Already having reached a T_c of 22 K, HEB mixers can operate above 12 K with only a 25% increase of the noise temperature, compared to that at 4.2 K. **MgB_2 HEB mixers can have a noise temperature as low as 700 K.** Three different methods for mixer conversion gain estimation: the gain method and U-factor methods with superconducting and normal reference states, were applied and compared. Good agreement with an error margin of ± 0.5 dB was demonstrated, which indicates the reliability of methods.

An HPCVD system was constructed and launched at Chalmers University of Technology. It is applicable for ultrathin film deposition down to 5 nm without a need for post-processing. Both the low resistivity of 50–90 $\mu\Omega$cm and the high J_c of up to 1.2×10^8 A/cm^2 indicate a rather good quality of the achieved films. The micron and submicron size HEB mixers can be fabricated from these films with a high yield (above 75%). The best deposited films that were used in fabrication of HEBs, were only 5 nm thick with a T_c of 33 K and a J_c of $(1–3) \times 10^8$ A/cm^2.

MgB_2 HEB mixers possess a unique combination of low noise, wide noise bandwidth, and high operation temperature when 5–8 nm thick superconducting MgB_2 films are used with a T_c of 30–33 K. It was demonstrated that compared to the gain bandwidth (GBW) of NbN HEB mixer ($\approx$3GHz), **the GBW for HEBs made from 8 nm thick HPCVD grown MgB_2 films was 10 GHz.** The GBW was inversely proportional to the film thickness and independent on both the bias voltage, the bath temperature, and LO fre-

quency (from 0.1 THz to 0.69 THz), which simplifies device characterisation. **A NBW of 11 GHz with a minimum receiver noise temperature of 930 K at 1.63 THz and 5 K was achieved.** At 15 K and 20 K, the noise temperature was 1100 K and 1600 K, respectively. From 0.69 THz to 1.63 THz the noise has increased by only 12%. The minimum noise temperature was achieved in a quite large range of bias voltages (5–10 mV) and LO power. **A similar noise temperature of $\approx$1000 K and a larger NBW of 13 GHz were achieved with HEB mixers with a T_c of 33 K made from 5 nm thick films.** Such devices have demonstrated a better noise performance at 20 K (1500 K), and operation at 25 K with a noise temperature of 2500 K. At 30 K the noise temperature was estimated to be 15 000 K.

Previously, a receiver noise temperature of 1600 K and a NBW of 6–8 GHz was measured for a 10 nm thick devices. An improvement of sensitivity and NBW was due to a larger bolometer width (lower contact resistance), applied in-situ contact cleaning, and a smaller film thickness. An increase of noise temperature at elevated bath temperatures is determined by a reduction of mixer conversion gain (less LO power is absorbed in the bolometer), while output noise of the HEB remains the same. A high output noise temperature (210 K), compared to values reported for NbN HEB mixers (60 K), lowers demands for the low noise IF chain. Instead of cryogenic LNAs at LHe temperature, LNAs at room temperature or LNAs mounted on higher stages of cryocooling system might be used. In this case crycoolers with a smaller cold plate and lower cooling power can be utilized, which is important for spaceborne telescopes where resources are always limited. Fabricated devices with a SiN_x passivation demonstrated high robustness and did not lose their properties after continuous storage in a nitrogen atmosphere. However, for a space applications special reliability tests would be required.

Good sensitivity and a large bandwidth as well as operation at elevated bath temperature have been achieved in HEBs from several batches. A combination of these parameters in one device would provide a perfect instrument for the sub-mm wave astronomy. MgB_2 HEB mixers have shown a potential to substitute current NbN (NbTiN) HEB mixers in certain applications, e.g. observation of wide doppler broadened emission from extra-galactic objects or operation on spaceborne satellite based telescopes utilizing light weight closed cycle cryocoolers. For utilization in future space missions, further investigation is required. The following steps in MgB_2 HEB mixer development should be performed:

- Despite a small increase of noise temperature was demonstrated when LO frequency increased from 0.69 THz to 1.63 THz, the low noise performance should still be demonstrated at higher frequencies, up to 5 THz.

- HPCVD process should be improved in order to reduce degradation of T_c with the film thickness reduction in order to achieve low noise operation at bath temperatures >20 K.

- Simultaneously, further development of the process is needed to be able to change the T_c of MgB_2 films without changing other film parameters, e.g. in order to lower the T_c to reduce LO power requirements.

- Modification of fabrication process is required in order to improve the

antenna/film contact and consequently to reduce contact resistance without increasing bolometer width.

- Currently used SiC substrates do not provide a possibility of HEB fabrication on thin membranes for realization of waveguide receivers. Other substrate materials should be tested, e.g. thin SiC on Si substrate.

- Stability of MgB_2 HEB mixers should be investigated by measuring Allan variance. Possibly, the development of receivers utilizing balanced HEB mixers scheme would be required.

Chapter 8

Summary of appended papers

Paper A

MgB$_2$ hot-electron bolometer mixers at terahertz frequencies

Submicron size HEBs were fabricated with no degradation of the initial film T$_c$ from a 20 nm MgB$_2$ MBE grown film with a T$_c$ of 22 K. In the direct detection mode, the maximum voltage responsivity was in the range of 1–2 kV/W at 1.63 THz and the optimal bias current is around 1/4-1/3 of the I$_c$ at 4.2 K. 1.63 THz radiation has the same effect on the HEB's IV-curve as a rise in temperature indicating that the response of the device is bolometric.

Contribution: Device layout design. Fabrication process development. Fabrication and responsivity characterisation of HEBs with a higher T$_c$. Co-writing of the paper.

Paper B

Effect of the critical and operational temperatures on the sensitivity of MgB$_2$ HEB mixers

Results of the noise and gain bandwidth investigation of HEB mixers made from 10 nm thick MgB$_2$ films with a T$_c$ of 8.5 K and 20 nm thick MgB$_2$ film with a T$_c$ of 22.5 K are presented. At an LO frequency of 1.63 THz the minimum reciever noise temperature was 700 K with a NBW of 3.5 GHz and a gain of -18 dB for a device with a T$_c$ of 8.5 K. For a device with a T$_c$ of 22.5 K the corresponding values were 1700 K, 5 GHz and -15 dB. For the latter device the Tr was 2150 K at a bath temperature of 12 K, which is not achievable with Nb-compound based HEB mixers. Different methods for measurements of the HEB mixer gain and the output noise are presented and compared.

Contribution: Device layout design. Fabrication process development. Fabrication of the HEB with a higher T$_c$, part of THz characterisation of HEBs with low and high Tc. Writing of the paper.

Paper C

Study of MgB$_2$ ultrathin films in submicron size bridges

A custom built HPCVD system for MgB$_2$ ultrathin film deposition: construction, deposition process development, and optimization are discussed. Achieved films on SiC substrates have a T$_c$ ranging from 35 K (10 nm thick films) to 41 K (40 nm thick films). The 20 nm thick unpatterned film had a room temperature resistivity of 13 $\mu\Omega$cm, whereas it becomes 50 $\mu\Omega$cm in submicron size bridges with a J$_c$ (4.2 K) up to 1.2×10^8 A/cm^2. The lower value of resistivity corresponds to the higher of both T$_c$ and J$_c$. The surface roughness, measured with an AFM, is approximately 1.5 nm. Possibility of thinning down of MgB$_2$ film by Ar$^+$ ion-beam milling is studied.

Contribution: Participation in designing and construction of the HPCVD system. Thin film characterisation during optimization of film deposition process. Layout design. Fabrication process development. Fabrication of submicron size bridges. DC characterisation of nanobridges. SEM and AFM scans. Writing of the paper.

Paper D

MgB$_2$ hot electron bolometer mixers for THz heterodyne instruments

Experimental investigation of the MgB$_2$ HEB mixers for low noise mixing at terahertz frequencies is presented. The GBW measured by mixing of two THz sources is inversely proportional to the film thickness and it is at least 6 GHz for 15 nm thick devices. Performance of MgB$_2$ HEBs was compared to performance of one of the NbN HEB mixers made for the Herschel Space Observatory (one of the flight units), for which both the GBW and the NBW was measured. MgB$_2$ HEB mixers show a GBW at least a factor of three broader compared to the NbN HEB measured in the same set-up.

Contribution: Device layout design. Fabrication process development. Fabrication of HEBs. DC and part of THz characterisation of HEBs.

Paper E

Wideband THz HEB mixers using HPCVD MgB2 thin films

Results of experimental study of the GBW of MgB$_2$ HEB mixers at 0.1 THz and 0.4 THz are presented. Antenna integrated 0.25–1.5 um^2 area devices were made from thin MgB2 films deposited with a custom made HPCVD system. The GBW was found to be independent on the bias conditions, the bath temperature, and the LO frequency. At 0.69 THz and 23 K the noise temperature of this mixer was 3000 K (corrected for optical losses).

Contribution: Device layout design. Fabrication process development. Fabrication of HEBs. DC and part in THz characterisation of HEBs. Writing of the paper.

Paper F

Broadband MgB$_2$ Hot-Electron Bolometer THz Mixers operating up to 20 K

Performance of submicron size HEB mixers made from thin MgB$_2$ superconducting films is discussed. With a superconducting transition temperature of about 30 K, such THz mixers can operate with high sensitivity at temperatures up to 20 K. Due to very small dimensions LO power requirements are rather low. In the IF band of 1–3 GHz the double sideband receiver noise temperature is 1600 K at 10 K operation temperature, 2000 K at 15 K, 2500–3000 K at 20 K. The NBW is estimated to be 6–8 GHz.

Contribution: Device layout design. Fabrication process development. Fabrication of HEBs. DC and part in THz characterisation of HEBs. Co-writing of the paper.

Paper G

Low noise terahertz MgB2 hot-electron bolometer mixers with an 11 GHz bandwidth

THz HEB mixers with a low noise temperature, a wide NBW, and a high operation temperature made from an 8 nm thick superconducting MgB$_2$ film are presented. A NBW of 11 GHz with a minimum noise temperature of 930 K at 1.63 THz and 5 K are obtained. At 15 K and 20 K, the noise temperature is 1100 K and 1600 K, respectively. From 0.69 THz to 1.63 THz the receiver noise increases by only 12%. Device current-voltage characteristics are identical when pumped with LOs from 0.69 THz up to 2.56 THz, and match well with IV curves at elevated temperatures. Therefore, the effect of the THz waves on the mixer is totally thermal, due to absorption in the π conduction band of MgB$_2$.

Contribution: Device layout design. Fabrication process development. Fabrication of HEBs. DC and part in THz characterisation of HEBs. Co-writing of the paper.

Paper H

Gain and noise in THz MgB2 hot-electron bolometer mixers with a 30 K critical temperature

The detailed study of HEB mixers made from an 8 nm thick superconducting MgB$_2$ film is presented. Variation of the mixer characteristics such as noise temperature, gain, output noise, and LO power at 5 K, 15 K, and 20 K, and at 0.69 THz and 1.63 THz LO frequencies is investigated. The low noise performance is achieved in quite wide bias point range (5–10 mV). The main reason for the noise temperature to rise at higher temperatures is a reduction of the mixer gain, which occurs proportionally to the LO power reduction. On contrary, the output noise remains constant (for the same bias point). The mixer gain and output noise temperature are in the range of -(8–11) dB and 120–220 K, respectively.

Contribution: Device layout design. Fabrication process development. Fabrication of HEBs. DC and part in THz characterisation of HEBs. Co-writing of the paper.

Acknowledgment

This work would never be done without people I have worked with during my PhD studies.

First and foremost, I would like to express my deep gratitude to my supervisor Assoc. Prof. Sergey Cherednichenko for guidance, discussions and help with measurements and data analysis, which made this work possible.

My sincere thanks to my examiner Prof. Jan Stake for his support and for giving me the possibility to do the PhD at the Terahertz and Millimetre Wave Laboratory. Many special thanks to my ex-colleague Dr. Stella Bevilacqua for the fruitful discussions, for guidance and help in the process lab and for assisting me in the measurement lab. In addition, I want to thank Vladimir Drakinskiy for helpful discussions, teaching me in the process lab and giving me lots of hints about the processing.

Prof. Hiroyuki Shibata from KITAMI Institute of Technology, Prof. Yasuhiro Tokura from University of Tsukuba, and NTT Basic Research Laboratories, are acknowledged for the MBE MgB_2 films providing.

Prof. Xiaoxing Xi and Prof. Ke Chen from Temple University, are acknowledged for valuable discussions on HPCVD MgB_2 film technology.

Kiryl Kustanovich, Dr. Tomas Bryllert, and Dr. Andrei Gorodetsky are acknowledged for the help with the thesis proofreading.

I want to thank all the staff of the Nanofabrication Laboratory. In particular, Henrik Frederiksen for the great help with the construction of the HPCVD system.

Special thanks to my parents and friends for encouraging me and their support.

Bibliography

[1] A. Rogalski and F. Sizov, "Terahertz detectors and focal plane arrays," *Opto-Electronics Review*, vol. 19, no. 3, pp. 346–404, September 2011.

[2] R. A. Lewis, "A review of terahertz sources," *Journal of Physics D: Applied Physics*, vol. 47, no. 37, p. 374001, September 2014.

[3] P. Siegel, "Terahertz technology in biology and medicine," *IEEE Transactions on Microwave Theory and Techniques*, vol. 52, no. 10, pp. 2438–2447, October 2004.

[4] M. C. Kemp, P. F. Taday, B. E. Cole, J. A. Cluff, A. J. Fitzgerald, and W. R. Tribe, "Security applications of terahertz technology," *Procedeengs of SPIE*, vol. 5070, pp. 44–52, 2003.

[5] M. Fitch and R. Osiander, "Terahertz waves for communications and sensing," *Johns Hopkins APL Technical Digest (Applied Physics Laboratory)*, vol. 25, no. 4, pp. 348–355, 2004.

[6] T. Phillips and J. Keene, "Submillimeter astronomy," *Proceedings of the IEEE*, vol. 80, no. 11, pp. 1662–1678, November 1992.

[7] G. Stacey, "THz Low Resolution Spectroscopy for Astronomy," *IEEE Transactions on Terahertz Science and Technology*, vol. 1, no. 1, pp. 241–255, September 2011.

[8] P. Ubertini, N. Gehrels, I. Corbett, P. de Bernardis, M. Machado, M. Griffin, M. Hauser, R. K. Manchanda, N. Kawai, S.-N. Zhang, and M. Pavlinsky, "Future of space astronomy: A global road map for the next decades," *Advances in space research*, vol. 50, no. 1, pp. 1–55, July 2012.

[9] J. Zmuidzinas and P. Richards, "Superconducting detectors and mixers for millimeter and submillimeter astrophysics," *Proceedings of the IEEE*, vol. 92, no. 10, pp. 1597–1616, October 2004.

[10] H.-W. Hübers, "Terahertz heterodyne receivers," *IEEE Journal of Selected Topics in Quantum Electronics*, vol. 14, no. 2, pp. 378–391, Mar-Apr 2008.

[11] I. Mehdi, J. V. Siles, C. Lee, and E. Schlecht, "THz diode technology: status, prospects, and applications," *Proceedings of the IEEE*, January 2017.

[12] A. R. Kerr, S. K. Pan, and W. G. Lyons, "The genesis of SIS mixers - the legacy of John Tucker in radio astronomy," in *2015 IEEE MTT-S International Microwave Symposium*, May 2015.

[13] A. Shurakov, Y. Lobanov, and G. Gol'tsman, "Superconducting hot-electron bolometer: From the discovery of hot-electron phenomena to practical applications," *Superconductor Science and Technology*, vol. 29, no. 2, p. 023001, December 2016.

[14] E. Gershenzon, G. Gol´tsman, I. Gogidze, Y. Gusev, A. Elantev, B. Karasik, and A. Semenov, "Millimeter and submillimeter range mixer based on electronic heating of superconductive films in the resistive state," *Superconductivity*, vol. 10, no. 3, pp. 1582–1597, October 1990.

[15] E. Gershenzon, M. Gershenzon, G. Gol'tsman, A. Semyonov, and A. Sergeev, "Heating of electrons in superconductor in the resistive state due to electromagnetic radiation," *Solid State Communications*, vol. 50, no. 3, pp. 207–212, 1984.

[16] K. Zhou, W. Miao, Z. Lou, J. Hu, S. Li, W. Zhang, S. Shi, R. Lefevre, Y. Delorme, and T. Vacelet, "A 1.4 THz quasi-optical NbN superconducting HEB mixer developed for the DATE5 telescope," *IEEE Transactions on Applied Superconductivity*, vol. 25, no. 3, p. 2300805, June 2015.

[17] W. Zhang, P. Khosropanah, J. Gao, T. Bansal, T. Klapwijk, W. Miao, and S. Shi, "Noise temperature and beam pattern of an NbN hot electron bolometer mixer at 5.25 THz," *Journal of Applied Physics*, vol. 108, no. 9, p. 093102, March 2010.

[18] D. Marrone, R. Blundell, E. Tong, S. Paine, D. Loudkov, J. Kawamura, D. Lühr, and C. Barrientos, "Observations in the 1.3 and 1.5 THz Atmospheric Windows with the Receiver Lab Telescope," in *16th International Symposium on Space Terahertz Technology*, May 2005, pp. 64–67.

[19] D. Meledin, A. Pavolotsky, V. Desmaris, I. Lapkin, C. Risacher, V. Perez, D. Henke, O. Nystrom, E. Sundin, D. Dochev, M. Pantaleev, M. Fredrixon, M. Strandberg, B. Voronov, G. Goltsman, and V. Belitsky, "A 1.3-THz balanced waveguide HEB mixer for the APEX telescope," *IEEE Transactions on Microwave Theory and Techniques*, vol. 57, no. 1, pp. 89–98, January 2009.

[20] C. Risacher, D. Meledin, V. Belitsky, and P. Bergman, "First 1.3 THz Observations at the APEX Telescope," in *20th International Symposium on Space Terahertz Technology*, April 2009, pp. 54–61.

[21] T. de Graauw et al., "The Herschel-Heterodyne Instrument for the Far-Infrared (HIFI)," *Astronomy & Astrophysics*, vol. 518, p. L6, July-August 2010.

[22] P. Goldsmith and D. Lis, "Early Science Results From the Heterodyne Instrument for the Far Infrared (HIFI) on the Herschel Space Observatory," *Terahertz Science and Technology, IEEE Transactions on*, vol. 2, no. 4, pp. 383–392, July 2012.

[23] M. Suttiwong, M. Birk, G. Wagner, M. Krocka, M. Wittkamp, P. Haschberger, P. Vogt, and F. Geiger, "Development and characterization of the balloon borne instrument TELIS (TEerahertz and submm LImb Sounder): 1.8 THz receiver," in *19th ESA Symposium on European Rocket and Balloon Programmes and Related Research*, June 2009.

[24] M. Birk, G. Wagner, G. de Lange, A. de Lange, B. N. Ellison, M. Harman, A. Murk, H. Oelhaf, G. Maucher, and C. Sartorius, "TELIS: TEerahertz and submmw LImb Sounder - Project summary after first successful flight," in *21th International Symposium on Space Terahertz Technology*, March 2010, pp. 195–200.

[25] C. Walker, C. Kulesa, P. Bernasconi, H. Eaton, N. Rolander, C. Groppi, J. Kloosterman, T. Cottam, D. Lesser, C. Martin, A. Stark, D. Neufeld, C. Lisse, D. Hollenbach, J. Kawamura, P. Goldsmith, W. Langer, H. Yorke, J. Sterne, A. Skalare, I. Mehdi, S. Weinreb, J. Kooi, J. Stutzki, U. Graf, M. Brasse, C. Honingh, R. Simon, M. Akyilmaz, P. Puetz, and M. Wolfire, "The Stratospheric THz Observatory (STO)," *Proceedings of SPIE*, vol. 7733, p. 77330N, July 2010.

[26] Kawamura, J. and Skalare, A. and Stern, J. and Tong, E., "A 1.5THz waveguide heb mixer using silicon-on-insulator substrates for the Stratospheric Terahertz Observatory," in *21th International Symposium on Space Terahertz Technology*, March 2010, p. 217.

[27] Brasse, M. and Graf, U.U. and Honingh, C.E. and Jacobs, K. and Justen, M. and Pütz, P. and Schultz, M. and Stutzki, J., "Receiver optics and 1.9 THz HEB mixers for STO," in *22th International Symposium on Space Terahertz Technology*, April 2011.

[28] D. Hayton, J. Kloosterman, Y. Ren, T. Kao, J. Gao, T. Klapwijk, Q. Hu, C. Walker, and J. Reno, "A 4.7THz heterodyne receiver for a balloon borne telescope," *Proceedings of SPIE*, vol. 9153, p. 91531R, July 2014.

[29] Young, A. and Walker, C. and Kulesa, C. and Bernasconi, P. and Dominguez, R. and Siles, J. and Hayton, D. and Gao, J.R. and Peters, W. and Goldsmith, P., "Stratospheric Terahertz Observatory 2016, Suborbital flight from McMurdo, Antarctica," in *22th International Symposium on Space Terahertz Technology*, March 2017.

[30] S. Heyminck, U. U. Graf, R. Güsten, J. Stutzki, H. W. Hübers, and P. Hartogh, "GREAT: the SOFIA high-frequency heterodyne instrument," *Astronomy & Astrophysics*, vol. 542, p. L1, June 2012.

[31] D. Büchel, P. Pütz, K. Jacobs, M. Schultz, U. Graf, C. Risacher, H. Richter, O. Ricken, H. Hübers, R. Güsten, C. Honingh, and J. Stutzki, "4.7-THz superconducting hot electron bolometer waveguide mixer," *IEEE Transactions on Terahertz Science and Technology*, vol. 5, no. 2, pp. 207–214, March 2015.

[32] C. Risacher, R. Güsten, J. Stutzki, H. Hübers, D. Büchel, U. Graf, S. Heyminck, C. Honingh, K. Jacobs, B. Klein, T. Klein, C. Leinz,

P. Pütz, N. Reyes, O. Ricken, H. Wunsch, P. Fusco, and S. Rosner, "First Supra-THz heterodyne array receivers for astronomy with the SOFIA observatory," *IEEE Transactions on Terahertz Science and Technology*, vol. 6, no. 2, pp. 199–211, March 2016.

[33] L. Jiang, S. Shiba, T. Shiino, K. Shimbo, N. Sakai, T. Yamakura, Y. Irimajiri, P. Ananthasubramanian, H. Maezawa, and S. Yamamoto, "Development of 1.5 THz waveguide NbTiN superconducting hot electron bolometer mixers," *Superconductor Science and Technology*, vol. 23, no. 4, p. 045025, March 2010.

[34] T. Shiino, L. Jiang, R. Furuya, T. Yamaguchi, S. Shiba, T. Sakai, N. Sakai, Y. Watanabe, O. Ohguchi, H. Maezawa, T. Yamakura, Y. Irimajiri, and S. Yamamoto, "Development of the 1.3–1.5 THz band superconducting HEB mixer receivers for ASTE 10m telescope," April 2011, p. 146.

[35] K. M. Zhou, W. Miao, S. Shi, R. Lefevre, and Y. Delorme, "Noise temperature and IF bandwidth of a 1.4 THz superconducting HEB mixer," in *2016 URSI Asia-Pacific Radio Science Conference (URSI AP-RASC 2016)*, August 2016, pp. 2010–2012.

[36] N. Manago, H. Ozeki, and M. Suzuki, "Band selection study for the sub-mm limb sounder SMILES-2," in *IEEE Geoscience and Remote Sensing Symposium 2014*, July 2014, pp. 4153–4156.

[37] M. Suzuki, N. Manago, H. Ozeki, S. Ochiai, and P. Baron, "Sensitivity study of SMILES-2 for chemical species," p. 96390M, October 2015.

[38] "Gussto." [Online]. Available: http://www.as.arizona.edu/gussto

[39] W. Wild et al., "Millimetron - a large Russian-European submillimeter space observatory," *Experimental Astronomy*, vol. 23, no. 1, pp. 221–244, March 2009.

[40] A. V. Smirnov, A. M. Baryshev, P. de Bernardis, V. F. Vdovin, G. N. Gol'tsman, N. S. Kardashev, L. S. Kuz'min, V. P. Koshelets, A. N. Vystavkin, Y. V. Lobanov, S. A. Ryabchun, M. I. Finkel, and D. R. Khokhlov, "The current stage of development of the receiving complex of the Millimetron Space Observatory," *Radiophysics and Quantum Electronics*, vol. 54, no. 8, pp. 557–568, January 2012.

[41] D. Rigopoulou, M. Caldwell, B. Ellison, C. Pearson, E. Caux, A. Cooray, J. D. Gallego, M. Gerin, J. R. Goicoechea, P. Goldsmith, C. Kramer, D. C. Lis, S. Molinari, V. Ossenkopf-Okada, G. Savini, B. K. Tan, X. Tielens, S. Viti, M. Wiedner, and G. Yassin, "The Far Infrared Spectroscopic Explorer (FIRSPEX): probing the lifecycle of the ISM in the universe," *Proceedings of SPIE*, vol. 9904, p. 99042K, July 2016.

[42] "Origins   space   telescope."   [Online].   Available: http://asd.gsfc.nasa.gov/firs/

[43] A. F. Loenen, S. Lord, P. Morris, and T. G. Phillips, "Excitation of the molecular gas in the nuclear region of M82," *Astronomy & Astrophysics*, vol. 521, p. L2, October 2010.

[44] A. R. Kerr, "Low-noise room-temperature and cryogenic mixers for 80–120 GHz," *IEEE Transactions on Microwave Theory and Techniques*, vol. 23, no. 10, pp. 781–787, October 1975.

[45] E. Carlson, M. Schneider, and T. McMaster, "Subharmonically pumped millimeter-wave mixers," *IEEE Transactions on Microwave Theory and Techniques*, vol. 26, no. 10, pp. 706–715, October 1978.

[46] P. Siegel, R. Dengler, I. Mehdi, J. Oswald, W. Bishop, T. Crowe, and R. Mattauch, "Measurements on a 215-GHz subharmonically pumped waveguide mixer using planar back-to-back air-bridge Schottky diodes," *IEEE Transactions on Microwave Theory and Techniques*, vol. 41, no. 11, pp. 1913–1921, November 1993.

[47] I. Mehdi, T. Lee, D. Humphrey, S. Martin, R. Dengler, J. Oswald, A. Pease, R. Smith, and P. Siegel, "600 GHz planar-Schottky-diode subharmonic waveguide mixers," in *1996 IEEE MTT-S International Microwave Symposium Digest*, vol. 1, June 1996, pp. 377–380.

[48] I. Mehdi, T. Lee, R. Dengler, A. Pease, J. Oswald, D. Humphrey, S. Martin, R. Smith, and P. Siegel, "200 GHz waveguide based subharmonically-pumped mixers with planar Schottky diodes," in *7th International Symposium on Space Terahertz Technology (ISSTT 1996)*, March 1996, pp. 450–461.

[49] P. Marsh, K. Hong, and D. Pavlidis, "InGaAs-based mm-wave integrated subharmonic mixer exhibiting low input power requirement and low noise characteristics," in *8th International Conference on Indium Phosphide and Related Materials*, April 1996, pp. 57–60.

[50] A. L. Betz and R. T. Boreiko, "A practical Schottky mixer for 5 THz (Part II)," in *7th International Symposium on Space Terahertz Technology (ISSTT 1996)*, March 1996, pp. 503–510.

[51] R. Boreiko and A. Betz, "Heterodyne Spectroscopy of the 63 μm OI Line in M42," *The Astrophysical Journal Letters*, vol. 464, no. 1, p. L83, June 1996.

[52] J. Hesler, T. Crowe, W. Bishop, R. Weikle, R. Bradley, and S.-K. Pan, "The development of planar Schottky diode waveguide mixers at submillimeter wavelengths," in *1997 IEEE MTT-S International Microwave Symposium Digest*, vol. 2, June 1997, pp. 953–956.

[53] I. Mehdi, S. Marazita, D. Humphrey, L. T.-H., R. Dengler, J. Oswald, A. Pease, S. Martin, W. Bishop, T. Crowe, and P. Siegel, "Improved 240-GHz subharmonically pumped planar Schottky diode mixers for spaceborne applications," *IEEE Transactions on Microwave Theory and Techniques*, vol. 46, no. 12, pp. 2036–2042, December 1998.

[54] S. Marazita, J. Hesler, R. Feinaugle, W. Bishop, and T. Crowe, "Planar Schottky mixer development to 1 THz and beyond," in *9th International Symposium on Space Terahertz Technology (ISSTT 1998)*, March 1998, pp. 501–510.

[55] P. Siegel, R. Smith, M. Graidis, and S. Martin, "2.5-THz GaAs monolithic membrane-diode mixer," *IEEE Transactions on Microwave Theory and Techniques*, vol. 47, no. 5, pp. 596–604, May 1999.

[56] K. Huber, H. Brand, and L.-P. Schmidt, "A broadband low noise heterodyne receiver at 2.5 THz," in *8th International Conference on Terahertz Electronics*, September 2000.

[57] S. Marazita, W. Bishop, J. Hesler, K. Hui, W. E. Bowen, and T. W. Crowe, "Integrated GaAs Schottky mixers by spin-on-dielectric wafer bonding," *IEEE Transactions on Electron Devices*, vol. 47, no. 6, pp. 1152–1157, June 2000.

[58] B. Thomas, A. Maestrini, and G. Beaudin, "A low-noise fixed-tuned 300–360-GHz sub-harmonic mixer using planar Schottky diodes," *IEEE Microwave and Wireless Components Letters*, vol. 15, no. 12, pp. 865–867, December 2005.

[59] E. Schlecht, J. Gill, R. Dengler, R. Lin, R. Tsang, and I. Mehdi, "A unique 520–590 GHz biased subharmonically-pumped Schottky mixer," *IEEE Microwave and Wireless Components Letters*, vol. 17, no. 12, pp. 879–881, December 2007.

[60] J. Hesler, H. Xu, A. Brissette, and W. Bishop, "Development and characterization of THz planar Schottky diode mixers and detectors," in *19th International Symposium on Space Terahertz Technology (ISSTT 2008)*, April 2008, pp. 224–225.

[61] B. Thomas, A. Maestrini, J. Gill, C. Lee, R. Lin, I. Mehdi, and P. de Maagt, "A broadband 835–900-GHz fundamental balanced mixer based on monolithic GaAs membrane Schottky diodes," *IEEE Transactions on Microwave Theory and Techniques*, vol. 58, no. 7, pp. 1917–1924, July 2010.

[62] P. Sobis, N. Wadefalk, A. Emrich, and J. Stake, "A broadband, low noise, integrated 340 GHz Schottky diode receiver," *IEEE Microwave and Wireless Components Letters*, vol. 22, no. 7, pp. 366–368, July 2012.

[63] H. Zhao, V. Drakinskiy, P. Sobis, J. Hanning, T. Bryllert, A.-Y. Tang, and J. Stake, "Development of a 557 GHz GaAs monolithic membrane-diode mixer," in *2012 International Conference on Indium Phosphide and Related Materials*, August 2012, pp. 102–105.

[64] B. Thomas, M. Brandt, A. Walber, M. Philipp, H. Gibson, H. Czekala, T. Rose, and V. Kangas, "Submillimetre-wave receiver developments for ICI onboard MetOP-SG and ice cloud remote sensing instruments," in *2012 IEEE International Geoscience and Remote Sensing Symposium*, July 2012, pp. 1278–1281.

[65] S. A. Retzloff, A. Young, and J. Hesler, "A 1.46 THz Schottky receiver at cryogenic temperatures," in *39th International Conference on Infrared, Millimeter, and Terahertz waves (IRMMW-THz 2014)*, September 2014.

[66] E. Schlecht, J. Siles, C. Lee, R. Lin, B. Thomas, G. Chattopadhyay, and I. Mehdi, "Schottky diode based 1.2 THz receivers operating at room-temperature and below for planetary atmospheric sounding," *IEEE Transactions on Terahertz Science and Technology*, vol. 4, no. 6, pp. 661–669, November 2014.

[67] J. Treuttel, L. Gatilova, A. Maestrini, D. Moro-Melgar, F. Yang, F. Tamazouzt, T. Vacelet, Y. Jin, A. Cavanna, J. Mateos, A. Feret, C. Chaumont, and C. Goldstein, "A 520–620-GHz Schottky receiver front-end for planetary science and remote sensing with 1070 K–1500 K DSB noise temperature at room temperature," *IEEE Transactions on Terahertz Science and Technology*, vol. 6, no. 1, pp. 148–155, January 2016.

[68] T. Reck, A. Zemora, E. Schlecht, R. Dengler, W. Deal, and G. Chattopadhyay, "A 230 GHz MMIC-based sideband separating receiver," *IEEE Transactions on Terahertz Science and Technology*, vol. 6, no. 1, pp. 141–147, January 2016.

[69] P. J. Sobis, V. Drakinskiy, N. Wadefalk, P.-A. Nilsson, D. Nyberg, A. Hammar, T. Bryllert, H. Zhao, A. Emrich, J. Grahn, and J. Stake, "Ultra low noise 600/1200 GHz and 874 GHz GaAs Schottky receivers for SWI and ISMAR," in *27th International Symposium on Space Terahertz Technology (ISSTT 2016)*, April 2016.

[70] M. Justen, M. Schultz, T. Tils, R. Teipen, S. Glenz, P. Pütz, C. Honingh, and K. Jacobs, "SIS flight mixers for Band 2 of the HIFI instrument of the Herschel Space Observatory," in *Conference Digest of the Joint Infrared and Millimeter Waves 29th International Conference on Infrared and Millimeter Waves and 12th International Conference on Terahertz Electronics*, September 2004, pp. 437–438.

[71] A. Karpov, D. Miller, F. Rice, J. Stern, B. Bumble, H. LeDuc, and J. Zmuidzinas, "Low noise NbTiN 1.25 THz SIS mixer for Herschel Space Observatory," in *16th International Symposium on Space Terahertz Technology (ISSTT 2005)*, May 2005, p. 450.

[72] A. Baryshev, F. Mena, J. Adema, R. Hesper, B. Jackson, G. Gerlofsma, M. Bekema, K. Keizer, H. Schaeffer, J. Barkhof, C. Lodewijk, D. Ludkov, T. Zijlstra, E. van Zeijl, T. Klapwijk, and W. Wild, "ALMA Band 9 cartridge," in *19th International Symposium on Space Terahertz Technology (ISSTT 2008)*, April 2008, pp. 258–262.

[73] Y. Sekimoto, Y. Iizuka, N. Satou, T. Ito, K. Kumagai, M. Kamikura, M. Naruse, and W. Shan, "Development of ALMA Band 8 (385–500 GHz) cartridge," in *19th International Symposium on Space Terahertz Technology (ISSTT 2008)*, April 2008, pp. 253–257.

[74] S. Asayama, S. Kawashima, H. Iwashita, T. Takahashi, M. Inata, Y. Obuchi, T. Suzuki, and T. Wada, "Design and development of ALMA Band 4 cartridge receiver," in *19th International Symposium on Space Terahertz Technology (ISSTT 2008)*, April 2008, pp. 244–249.

[75] B. Billade, O. Nystrom, D. Meledin, E. Sundin, I. Lapkin, M. Fredrixon, V. Desmaris, H. Rashid, M. Strandberg, S. Ferm, A. Pavolotsky, and V. Belitsky, "Performance of the first ALMA Band 5 production cartridge," *IEEE Transactions on Terahertz Science and Technology*, vol. 2, no. 2, pp. 208–214, March 2012.

[76] S. Mahieu, D. Maier, B. Lazareff, A. Navarrini, G. Celestin, J. Chalain, D. Geoffroy, F. Laslaz, and G. Perrin, "The ALMA Band-7 cartridge," *IEEE Transactions on Terahertz Science and Technology*, vol. 2, no. 1, pp. 29–39, January 2012.

[77] A. Kerr, S. Pan, S. Claude, P. Dindo, A. Lichtenberger, J. Effland, and E. Lauria, "Development of the ALMA Band-3 and Band-6 sideband-separating SIS mixers," *IEEE Transactions on Terahertz Science and Technology*, vol. 4, no. 2, pp. 201–212, March 2014.

[78] J. Kooi, R. Chamberlin, R. Monje, A. Kovacs, F. Rice, H. Yoshida, B. Force, K. Cooper, D. Miller, M. Gould, D. Lis, B. Bumble, R. LeDuc, J. Stern, and T. Phillips, "Performance of the Caltech Submillimeter Observatory dual-color 180–720 GHz balanced SIS receivers," *IEEE Transactions on Terahertz Science and Technology*, vol. 4, no. 2, pp. 149–164, March 2014.

[79] T. Kojima, K. Kuroiwa, T. Takahashi, Y. Fujii, Y. Uzawa, S. Asayama, and T. Noguchi, "Design and performance of mass-produced sideband separating SIS mixers for ALMA Band 4 receivers," *Superconductor Science and Technology*, vol. 28, no. 9, p. 094001, July 2015.

[80] T. Tamura, T. Noguchi, Y. Sekimoto, W. Shan, N. Sato, Y. Iizuka, K. Kumagai, Y. Niizeki, M. Iwakuni, and T. Ito, "Performance and uniformity of mass-produced SIS mixers for ALMA Band 8 receiver cartridges," *IEEE Transactions on Applied Superconductivity*, vol. 25, no. 3, p. 2400305, June 2015.

[81] S. Montazeri, P. K. Grimes, C.-Y. E. Tong, W.-T. Wong, and J. C. Bardin, "Direct integration of an SIS mixer with a high-impedance SiGe low noise amplifier," in *26th International Symposium on Space Terahertz Technology (ISSTT 2015)*, March 2015, pp. P–30.

[82] C. Tong, P. Grimes, J. Weintroub, and R. Blundell, "Ultra-wide IF bandwidth - The next frontier for SIS receivers," in *2015 IEEE MTT-S International Microwave Symposium (IMS 2015)*, May 2015.

[83] M. Yao, D. Liu, J. Hu, J. Li, and S. Shi, "Study of the input RF noise of a THz superconductor-insulator-superconductor receiver," in *2015 Asia-Pacific Microwave Conference (APMC 2015)*, vol. 2, December 2015.

[84] A. Khudchenko, A. Baryshev, K. Rudakov, P. Dmitriev, R. Hesper, L. de Jong, and V. Koshelets, "High-gap Nb-AlN-NbN SIS junctions for frequency band 790–950 GHz," *IEEE Transactions on Terahertz Science and Technology*, vol. 6, no. 1, pp. 127–132, January 2016.

[85] J. Chenu, A. Navarrini, Y. Bortolotti, G. Butin, A. Fontana, S. Mahieu, D. Maier, F. Mattiocco, P. Serres, M. Berton, O. Garnier, Q. Moutote, M. Parioleau, B. Pissard, and J. Reverdy, "The front-end of the NOEMA interferometer," *IEEE Transactions on Terahertz Science and Technology*, vol. 6, no. 2, pp. 223–237, March 2016.

[86] S. Montazeri, P. Grimes, C. Tong, and J. C. Bardin, "A 220-GHz SIS mixer tightly integrated with a sub-hundred-microwatt SiGe IF amplifier," *IEEE Transactions on Terahertz Science and Technology*, vol. 6, no. 1, pp. 133–140, January 2016.

[87] Y. Uzawa, Y. Fujii, M. Kroug, K. Makise, A. Gonzalez, K. Kaneko, T. Kojima, A. Miyachi, S. Saito, H. Terai, and Z. Wang, "Development of superconducting THz receivers for radio astronomy," in *41st International Conference on Infrared, Millimeter, and Terahertz waves (IRMMW-THz 2016)*, September 2016.

[88] A. Khudchenko, R. Hesper, A. Baryshev, J. Barkhof, and F. Mena, "Modular 2SB SIS receiver for 600-720 GHz: Performance and characterization methods," *IEEE Transactions on Terahertz Science and Technology*, vol. 7, no. 1, pp. 2–9, January 2017.

[89] S. Montazeri, P. Grimes, C. Tong, and J. Bardin, "A wide-band high-gain compact SIS receiver utilizing a 300-μW SiGe IF LNA," *IEEE Transactions on Applied Superconductivity*, vol. 27, no. 4, p. 1500605, June 2017.

[90] Y. Fujii, T. Kojima, A. Gonzalez, S. Asayama, M. Kroug, K. Kaneko, H. Ogawa, and Y. Uzawa, "Low-noise integrated balanced SIS mixer for 787–950 GHz," *Superconductor Science and Technology*, vol. 30, no. 2, p. 024001, November 2017.

[91] R. Wyss, B. Karasik, W. McGrath, B. Bumble, and H. LeDuc, "Noise and bandwidth measurements of diffusion-cooled Nb hot-electron bolometer mixers at frequencies above the superconductive energy gap," in *10th International Symposium on Space Terahertz Technology (ISSTT 1999)*, March 1999, pp. 215–228.

[92] J. Kawamura, R. Blundell, C. Tong, D. Papa, T. Hunter, S. Paine, F. Patt, G. Gol'tsman, S. Cherednichenko, B. Voronov, and E. Gershenzon, "Superconductive hot-electron-bolometer mixer receiver for 800-GHz operation," *IEEE Transactions on Microwave Theory and Techniques*, vol. 48, no. 4, pp. 683–689, April 2000.

[93] M. Kroug, S. Cherednichenko, H. Merkel, E. Kollberg, B. Voronov, G. Gol'tsman, H. Huebers, and H. Richter, "NbN hot electron bolometric mixers for terahertz receivers," *IEEE Transactions on Applied Superconductivity*, vol. 11, no. 1, pp. 962–965, March 2001.

[94] S. Cherednichenko, M. Kroug, H. Merkel, P. Khosropanah, A. Adam, E. Kollberg, D. Loudkov, G. Gol'tsman, B. Voronov, H. Richter, and H.-W. Hübers, "1.6 THz heterodyne receiver for the far infrared space telescope," *Physica C: Superconductivity*, vol. 372-376, no. 1, pp. 427–431, August 2002.

[95] T. Klapwijk, R. Barends, J. Gao, M. Hajenius, and J. Baselmans, "Improved superconducting hot-electron bolometer devices for the THz range," *Proceedings of SPIE*, vol. 5498, pp. 129–139, October 2004.

[96] J. Stern, B. Bumble, J. Kawamura, and A. Skalare, "Fabrication of terahertz frequency phonon cooled HEB mixers," *IEEE Transactions on Applied Superconductivity*, vol. 15, no. 2, pp. 499–502, June 2005.

[97] P. Khosropanah, J. Gao, W. Laauwen, M. Hajenius, and T. Klapwijk, "Low noise NbN hot electron bolometer mixer at 4.3 THz," *Applied Physics Letters*, vol. 91, no. 22, p. 221111, November 2007.

[98] S. Cherednichenko, V. Drakinskiy, T. Berg, P. Khosropanah, and E. Kollberg, "Hot-electron bolometer terahertz mixers for the Herschel Space Observatory," *Review of Scientific Instruments*, vol. 79, no. 3, p. 034501, March 2008.

[99] J. Schultz, D. Herald, H. Xu, L. Liu, R. Bass, R. Weikle, and A. Lichtenberger, "The design, fabrication and test results of a 1.6 THz superconducting hot electron bolometer mixer on SOI," *IEEE Transactions on Applied Superconductivity*, vol. 19, no. 3, pp. 297–300, June 2009.

[100] L. Jiang, S. Shiba, K. Shimbo, N. Sakai, T. Yamakura, M. Sugimura, P. Ananthasubramanian, H. Maezawa, Y. Irimajiri, and S. Yamamoto, "Development of THz waveguide NbTiN HEB mixers," *IEEE Transactions on Applied Superconductivity*, vol. 19, no. 3, pp. 301–304, June 2009.

[101] W. Zhang, P. Khosropanah, J. Gao, E. Kollberg, K. Yngvesson, T. Bansal, R. Barends, and T. Klapwijk, "Quantum noise in a terahertz hot electron bolometer mixer," *Applied Physics Letters*, vol. 96, no. 11, p. 111113, March 2010.

[102] Y. Lobanov, C. Tong, A. Hedden, R. Blundell, B. Voronov, and G. Gol'tsman, "Direct measurement of the gain and noise bandwidths of HEB mixers," *IEEE Transactions on Applied Superconductivity*, vol. 21, no. 3, pp. 645–648, June 2011.

[103] H. Maezawa, T. Yamakura, T. Shiino, S. Yamamoto, S. Shiba, N. Sakai, Y. Irimajiri, L. Jiang, N. Nakai, M. Seta, A. Mizuno, T. Nagahama, and Y. Fukui, "Stability of a quasi-optical superconducting NbTiN hot-electron bolometer mixer at 1.5 THz frequency band," *IEEE Transactions on Applied Superconductivity*, vol. 21, no. 3, pp. 640–644, June 2011.

[104] I. Tretyakov, S. Ryabchun, M. Finkel, A. Maslennikova, N. Kaurova, A. Lobastova, B. Voronov, and G. Gol'tsman, "Low noise and wide bandwidth of NbN hot-electron bolometer mixers," *Applied Physics Letters*, vol. 98, no. 3, p. 033507, January 2011.

[105] P. Pütz, C. Honingh, K. Jacobs, M. Justen, M. Schultz, and J. Stutzki, "Terahertz hot electron bolometer waveguide mixers for GREAT," *Astronomy & Astrophysics*, vol. 542, p. L2, June 2012.

[106] F. Boussaha, J. Kawamura, J. Stern, A. Skalare, and V. White, "A low noise 2.7 THz waveguide-based superconducting mixer," *IEEE Transactions on Terahertz Science and Technology*, vol. 2, no. 3, pp. 284–289, May 2012.

[107] S. Shiba, Y. Irimajiri, T. Yamakura, H. Maezawa, N. Sekine, I. Hosako, and S. Yamamoto, "3.1-THz heterodyne receiver using an NbTiN hot-electron bolometer mixer and a quantum cascade laser," *IEEE Transactions on Terahertz Science and Technology*, vol. 2, no. 1, pp. 22–28, January 2012.

[108] Y. Irimajiri, A. Kawakami, I. Morohashi, N. Sekine, S. Ochiai, S. Tanaka, I. Hosako, and M. Yasui, "Development of a low noise heterodyne receiver at 3 THz," in *37th International Conference on Infrared, Millimeter, and Terahertz Waves (IRMMW-THz 2012)*, September 2012.

[109] L. Jiang, C. Li, T. Shiino, and S. Yamamoto, "Intrinsic mixing behavior of superconducting NbTiN hot electron bolometer mixers based on in situ technique," *Physica C: Superconductivity*, vol. 485, pp. 120–124, February 2013.

[110] J. Kloosterman, D. Hayton, Y. Ren, T. Kao, J. Hovenier, J. Gao, T. Klapwijk, Q. Hu, C. Walker, and J. Reno, "Hot electron bolometer heterodyne receiver with a 4.7-THz quantum cascade laser as a local oscillator," *Applied Physics Letters*, vol. 102, no. 1, p. 011123, January 2013.

[111] F. Boussaha, J. Kawamura, J. Stern, and C. Jung-Kubiak, "2.7 THz balanced waveguide HEB mixer," *IEEE Transactions on Terahertz Science and Technology*, vol. 4, no. 5, pp. 545–551, September 2014.

[112] W. Miao, W. Zhang, Z. Lou, Y. Ren, S. Li, K. Zhang, Q. Yao, T. Kao, Q. Hu, and S. Shi, "A 3.7 THz third-order distributed feedback quantum cascade laser as the local oscillator of a superconducting hot electron bolometer receiver," in *31th URSI General Assembly and Scientific Symposium (URSI GASS 2014)*, August 2014.

[113] P. Pütz, D. Büchel, K. Jacobs, M. Schultz, and C. Honingh, "1.9 THz waveguide HEB mixers for the upGREAT low frequency array," in *26th International Symposium on Space Terahertz Technology (ISSTT 2015)*, March 2015, pp. M2–3.

[114] W. Miao, Z. Lou, G.-Y. Xu, J. Hu, S.-L. Li, W. Zhang, K.-M. Zhou, Q.-J. Yao, K. Zhang, W.-Y. Duan, S.-C. Shi, R. Colombelli, B. H.E., and

R. D.A., "Demonstration of a fully integrated superconducting receiver with a 2.7 THz quantum cascade laser," *Optics Express*, vol. 23, no. 4, pp. 4453–4458, February 2015.

[115] T. Shiino, R. Furuya, T. Soma, Y. Watanabe, T. Sakai, L. Jiang, H. Maezawa, T. Yamakura, N. Sakai, and S. Yamamoto, "Low-noise 1.5 THz waveguide-type hot-electron bolometer mixers using relatively thick NbTiN superconducting film," *Japanese Journal of Applied Physics*, vol. 54, no. 3, p. 033101, February 2015.

[116] A. Kawakami, Y. Irimajiri, Y. Uzawa, S. Tanaka, S. Ochiai, and I. Hosako, "Fabrication of 3 THz superconducting hot electron bolometer mixers," in *26th International Symposium on Space Terahertz Technology (ISSTT 2015)*, March 2015, pp. P–18.

[117] K. Zhou, W. Miao, J. Hu, S. Li, R. Lefevre, Y. Delorme, and S. Shi, "Performance of a 1.3-THz twin-slot antenna superconducting HEB mixer integrated with different elliptical lenses," in *2015 Asia-Pacific Microwave Conference (APMC 2015)*, December 2015.

[118] S. Jiang, X. Jia, B. Jin, L. Kang, W. Xu, J. Chen, and P. Wu, "Superconducting detectors for terahertz imaging," in *40th International Conference on Infrared, Millimeter, and Terahertz waves (IRMMW-THz 2015)*, August 2015.

[119] W. Zhang, W. Miao, K. M. Zhou, X. H. Guo, J. Q. Zhong, and S. C. Shi, "High sensitive THz superconducting hot electron bolometer mixers and transition edge sensors," *Proceedings of SPIE*, vol. 10030, p. 1003009, November 2016.

[120] I. Tret'yakov, N. Kaurova, B. Voronov, V. Anfert'ev, L. Revin, V. Vaks, and G. Gol'tsman, "The influence of the diffusion cooling on the noise band of the superconductor NbN hot-electron bolometer operating in the terahertz range," *Technical Physics Letters*, vol. 42, no. 6, pp. 563–566, July 2016.

[121] W. Miao, W. Zhang, K. Zhou, H. Gao, K. Zhang, W. Duan, Q. Yao, S. Shi, Y. Delorme, and R. Lefevre, "Investigation of the performance of NbN superconducting HEB Mixers of different critical temperatures," *IEEE Transactions on Applied Superconductivity*, vol. 27, no. 4, p. 2200304, June 2017.

[122] S. Cherednichenko, V. Drakinskiy, K. Ueda, and M. Naito, "Terahertz mixing in MgB_2 microbolometers," *Applied Physics Letters*, vol. 90, no. 2, January 2007.

[123] S. Bevilacqua, S. Cherednichenko, V. Drakinskiy, J. Stake, H. Shibata, and Y. Tokura, "Low noise mgb$_2$ terahertz hot-electron bolometer mixers," *Applied Physics Letters*, vol. 100, no. 3, p. 033504, January 2012.

[124] S. Bevilacqua, S. Cherednichenko, V. Drakinskiy, H. Shibata, Y. Tokura, and J. Stake, "Study of IF bandwidth of MgB_2 phonon-cooled hot-electron bolometer mixers," *IEEE Transactions on Terahertz Science and Technology*, vol. 3, no. 4, pp. 409–415, July 2013.

[125] D. Cunnane, J. Kawamura, M. Wolak, N. Acharya, T. Tan, X. Xi, and B. Karasik, "Characterization of MgB$_2$ superconducting hot electron bolometers," *Applied Superconductivity, IEEE Transactions on*, vol. 25, no. 3, p. 2300206, June 2015.

[126] D. Cunnane, J. H. Kawamura, M. A. Wolak, N. Acharya, X. X. Xi, and B. S. Karasik, "Optimization of parameters of MgB$_2$ hot-electron bolometers," *Applied Superconductivity, IEEE Transactions on*, vol. 27, no. 4, p. 2301104, June 2017.

[127] J. Nagamatsu, N. Nakagawa, T. Muranaka, Y. Zenitani, and J. Akimitsu, "Superconductivity at 39K in magnesium diboride," *Nature*, vol. 410, no. 6824, pp. 63–64, March 2001.

[128] W. N. Kang, H.-J. Kim, E.-M. Choi, C. U. Jung, and S.-I. Lee, "MgB$_2$ superconducting thin films with a transition temperature of 39 Kelvin," *Science*, vol. 292, no. 5521, pp. 1521–1523, May 2001.

[129] X. Zeng, A. Pogrebnyakov, A. Kotcharov, J. Jones, X. Xi, E. Lysczek, J. Redwing, X. Shengyong, Q. Li, J. Lettieri, D. Schlom, W. Tian, X. Pan, and Z.-K. Liu, "In situ epitaxial MgB$_2$ thin films for superconducting electronics," *Nature Materials*, vol. 1, no. 1, pp. 35–38, September 2002.

[130] K. Ueda and M. Naito, "In situ growth of superconducting MgB$_2$ thin films by molecular-beam epitaxy," *Journal of Applied Physics*, vol. 93, no. 4, pp. 2113–2120, February 2003.

[131] S. Bevilacqua, S. Cherednichenko, V. Drakinskiy, H. Shibata, A. Hammar, and J. Stake, "Investigation of MgB$_2$ HEB mixer gain bandwidth," in *IRMMW-THz 2011 - 36th International Conference on Infrared, Millimeter, and Terahertz Waves*, October 2011.

[132] D. Cunnane, J. Kawamura, B. Karasik, M. Wolak, and X. Xi, "Development of hot-electron THz bolometric mixers using MgB$_2$ thin films," *Proceedings of SPIE*, vol. 9153, p. 91531Q, July 2014.

[133] X. Xi, A. Pogrebnyakov, S. Xu, K. Chen, Y. Cui, E. Maertz, C. Zhuang, Q. Li, D. Lamborn, J. Redwing, Z. Liu, A. Soukiassian, D. Schlom, X. Weng, E. Dickey, Y. Chen, W. Tian, X. Pan, S. Cybart, and R. Dynes, "MgB$_2$ thin films by hybrid physical-chemical vapor deposition," *Physica C: Superconductivity*, vol. 456, no. 1-2, pp. 22–37, June 2007.

[134] F. Arams, C. Allen, B. Peyton, and E. Sard, "Millimeter mixing and detection in bulk InSb," *Proceedings of the IEEE*, vol. 54, no. 4, pp. 612–622, April 1966.

[135] N. Chi-Anh, H.-J. Shin, K.-T. Kim, Y.-H. Han, and S. Moon, "Characterization of uncooled bolometer with vanadium tungsten oxide infrared active layer," *Sensors and Actuators A: Physical*, vol. 123-124, pp. 87–91, September 2005.

[136] A. J. Miller, A. Luukanen, and E. N. Grossman, "Micromachined antenna-coupled uncooled microbolometers for terahertz imaging arrays," *Proceedings of SPIE*, vol. 5411, pp. 18–24, September 2004.

[137] T. G. Phillips and K. B. Jefferts, "A low temperature bolometer heterodyne receiver for millimeter wave astronomy," *Review of Scientific Instruments*, vol. 44, no. 8, pp. 1009–1014, August 1973.

[138] Y. P. Gousev, G. N. Gol'tsman, A. D. Semenov, E. M. Gershenzon, R. S. Nebosis, M. A. Heusinger, and K. F. Renk, "Broadband ultrafast superconducting NbN detector for electromagnetic radiation," *Journal of Applied Physics*, vol. 75, no. 7, April 1994.

[139] S. Cherednichenko, P. Khosropanah, E. Kollberg, M. Kroug, and H. Merkel, "Terahertz superconducting hot-electron bolometer mixers," *Physica C: Superconductivity*, vol. 372-376, no. 1, pp. 407–415, August 2002.

[140] D. E. Prober, "Superconducting terahertz mixer using a transition-edge microbolometer," *Applied Physics Letters*, vol. 62, no. 17, pp. 2119–2121, April 1993.

[141] A. Semenov, G. Gol'tsman, and R. Sobolewski, "Hot-electron effect in superconductors and its applications for radiation sensors," *Superconductor Science and Technology*, vol. 15, no. 4, pp. R1–R16, March 2002.

[142] N. Perrin and C. Vanneste, "Response of superconducting films to a periodic optical irradiation," *Phys. Rev. B*, vol. 28, pp. 5150–5159, November 1983.

[143] J. S. Blakemore, *Solid State Physics (2nd ed)*.   Cambridge, UK: University press, 1985.

[144] J.-L. Luo, J. Zhang, Z.-J. Chen, H.-Y. Bai, Y.-P. Wang, J.-B. Meng, D. Jin, R. Z.-A., G.-C. Che, and Z.-X. Zhao, "Low temperature specific heat of superconducting MgB_2," *Chinese Physics Letters*, vol. 18, no. 6, pp. 820–821, 2001.

[145] H. Merkel, P. Khosropanah, P. Yagoubov, and E. Kollberg, "A hot-spot mixer model for phonon-cooled NbN hot electron bolometric mixers," *Applied Superconductivity, IEEE Transactions on*, vol. 9, no. 2, pp. 4201–4204, June 1999.

[146] H. Merkel, P. Khosropanah, D. Wilms Floet, P. Yagoubov, and E. Kollberg, "Conversion gain and fluctuation noise of phonon-cooled hot-electron bolometers in hot-spot regime," *Microwave Theory and Techniques, IEEE Transactions on*, vol. 48, no. 4, pp. 690–699, April 2000.

[147] H. Merkel, P. Khosropanah, S. Cherednichenko, K. Yngvesson, A. Adam, and E. Kollberg, "A two-dimensional hot-spot mixer model for phonon-cooled hot electron bolometers," *Applied Superconductivity, IEEE Transactions on*, vol. 11, no. 1, pp. 179–182, March 2001.

[148] B. S. Karasik and A. Elantev, "Analysis of the noise performance of a hot-electron superconducting bolometer mixer," in *6th International Symposium on Space Terahertz Technology*, March 1995, pp. 229–246.

[149] H. Ekström, B. Karasik, E. Kollberg, and K. Yngvesson, "Conversion gain and noise of niobium superconducting hot-electron-mixers," *IEEE Transactions on Microwave Theory and Techniques*, vol. 43, no. 4, pp. 938–947, April 1995.

[150] S. Bevilacqua, E. Novoselov, S. Cherednichenko, H. Shibata, and Y. Tokura, "Wideband MgB_2 hot-electron bolometer mixers: IF impedance characterisation and modeling," *IEEE Transactions on Applied Superconductivity*, vol. 26, no. 3, pp. 1–5, April 2016.

[151] J. W. Kooi, J. J. A. Baselmans, M. Hajenius, J. R. Gao, T. M. Klapwijk, P. Dieleman, A. Baryshev, and G. de Lange, "IF impedance and mixer gain of NbN hot electron bolometers," *Journal of Applied Physics*, vol. 101, no. 4, p. 044511, February 2007.

[152] H. Merkel, P. Yagoubov, P. Khosropanah, and E. Kollberg, "An accurate calculation method of the absorbed LO power in hot electron bolometric mixers," in *1998 IEEE Sixth International Conference on Terahertz Electronics Proceedings (THZ 98)*, September 1998, pp. 145–148.

[153] P. Khosropanah, H. Merkel, S. Yngvesson, A. Adam, S. Cherednichenko, and E. Kollberg, "A distributed device model for phonon-cooled HEB mixers predicting IV characteristics, gain, noise and IF bandwidth," in *11th International Symposium on Space Terahertz Technology*, May 2000, pp. 474–488.

[154] J. C. Mather, "Bolometer noise: nonequilibrium theory," *Appl. Opt.*, vol. 21, no. 6, pp. 1125–1129, March 1982.

[155] B. S. Karasik and A. I. Elantiev, "Noise temperature limit of a superconducting hot electron bolometer mixer," *Applied Physics Letters*, vol. 68, no. 6, pp. 853–855, February 1996.

[156] R. Nebosis, A. Semenov, Y. Gousev, and K. Renk, "Rigorous analysis of a superconducting hot-electron bolometer mixer: Theory and comparison with experiment," in *7th International Symposium on Space Terahertz Technology (ISSTT 1996)*, March 1996, pp. 601–613.

[157] S. Cherednichenko, V. Drakinskiy, J. Baubert, B. Lecomte, F. Dauplay, J.-M. Krieg, Y. Delorme, A. Feret, H.-W. Hübers, A. D. Semenov, and G. N. Gol'tsman, "2.5 THz multipixel heterodyne receiver based on NbN HEB mixers," *Proceedings of SPIE*, vol. 6275, p. 62750I, June 2006.

[158] E. Gerecht, D. Gu, X. Zhao, J. Nicholson, F. Rodriguez-Morales, and S. Yngvesson, "Development of NbN terahertz HEB mixers coupled through slot-ring antennas," in *15th International Symposium on Space Terahertz Technology (ISSTT 2004)*, April 2004, pp. 33–40.

[159] E. Gerecht, C. Musante, H. Jian, Y. Zhuang, K. Yngvesson, J. Dickinson, T. Goyette, J. Waldman, P. Yagoubov, G. Gol'tsman, B. Voronov, and E. Gershenzon, "Improved characteristics of NbN HEB mixers integrated with log-periodic antennas," in *10th International Symposium on Space Terahertz Technology (ISSTT 1999)*, March 1999, pp. 200–207.

[160] E. Grossman, "Lithographic antennas for submillimeter and infrared frequencies," in *Proceedings of International Symposium on Electromagnetic Compatibility*, August 1995, pp. 102–107.

[161] H.-W. Hübers, J. Schubert, A. Krabbe, M. Birk, G. Wagner, A. Semenov, G. Gol'tsman, B. Voronov, and E. Gershenzon, "Parylene antireflection coating of a quasi-optical hot-electron-bolometric mixer at teraherz frequencies," *Infrared Physics & Technology*, vol. 42, no. 1, pp. 41–47, February 2001.

[162] Y. Xu, M. Khafizov, L. Satrapinsky, P. Kus, A. Plecenik, and R. Sobolewski, "Time-resolved photoexcitation of the superconducting two-gap state in MgB_2 thin films," *Physical Review Letters*, vol. 91, no. 19, p. 197004, November 2003.

[163] Y. Naidyuk, I. Yanson, L. Tyutrina, N. Bobrov, P. Chubov, W. Kang, H.-J. Kim, E.-M. Choi, and S.-I. Lee, "Superconducting energy gap distribution in c-axis oriented MgB_2 thin film from point contact study," *Journal of Experimental and Theoretical Physics Letters*, vol. 75, no. 5, pp. 238–241, March 2002.

[164] B. Jin, T. Dahm, C. Iniotakis, A. Gubin, E.-M. Choi, H. Kim, L. S.-I., W. Kang, S. Wang, Y. Zhou, A. Pogrebnyakov, J. Redwing, X. Xi, and N. Klein, "Dependence of penetration depth, microwave surface resistance and energy gap of MgB_2 thin films on their normal-state resistivity," *Superconductor Science and Technology*, vol. 18, no. 1, p. L1, November 2005.

[165] R. Cubitt, M. R. Eskildsen, C. D. Dewhurst, J. Jun, S. M. Kazakov, and J. Karpinski, "Effects of two-band superconductivity on the flux-line lattice in magnesium diboride," *Physical Review Letters*, vol. 91, p. 047002, July 2003.

[166] C. Eom, M. Lee, J. Choi, L. Belenky, X. Song, L. Cooley, M. Naus, S. Patnaik, J. Jiang, M. Rikel, A. Polyanskii, A. Gurevich, X. Cai, S. Bu, S. Babcock, E. Hellstrom, D. Larbalestier, N. Rogado, K. Regan, M. Hayward, T. He, J. Slusky, K. Inumaru, M. Haas, and R. Cava, "High critical current density and enhanced irreversibility field in superconducting mgb_2 thin films," *Nature*, vol. 411, no. 6837, pp. 558–560, May 2001.

[167] Z.-K. Liu, D. Schlom, Q. Li, and X. Xi, "Thermodynamics of the Mg-B system: Implications for the deposition of MgB_2 thin films," *Applied Physics Letters*, vol. 78, no. 23, pp. 3678–3680, June 2001.

[168] K. Ueda and M. Naito, "As-grown superconducting MgB$_2$ thin films prepared by molecular beam epitaxy," *Applied Physics Letters*, vol. 79, no. 13, pp. 2046–2048, September 2001.

[169] A. Saito, A. Kawakami, H. Shimakage, and Z. Wang, "As-grown MgB$_2$ thin films deposited on Al$_2$O$_3$ substrates with different crystal planes," *Superconductor Science and Technology*, vol. 15, no. 9, pp. 1325–1329, 2002.

[170] H. Shimakage, A. Saito, K. A., and Z. Wang, "Optimizing preparation of as-grown MgB$_2$ thin films made using the co-evaporation method," *Physica C: Superconductivity*, vol. 392-396, Part 2, pp. 1291–1295, 2003.

[171] S. D. Bu, D. M. Kim, J. H. Choi, J. Giencke, E. E. Hellstrom, D. C. Larbalestier, S. Patnaik, L. Cooley, C. B. Eom, J. Lettieri, D. G. Schlom, W. Tian, and X. Q. Pan, "Synthesis and properties of c-axis oriented epitaxial MgB$_2$ thin films," *Applied Physics Letters*, vol. 81, no. 10, pp. 1851–1853, November 2002.

[172] Y. Zhang, Z. Lin, Q. Dai, D. Li, Y. Wang, Y. Zhang, Y. Wang, and Q. Feng, "Ultrathin MgB$_2$ films fabricated on Al$_2$O$_3$ substrate by hybrid physical-chemical vapor deposition with high T$_c$ and J$_c$," *Superconductor Science and Technology*, vol. 24, no. 1, p. 015013, January 2011.

[173] Z.-J. Liu, S. Zhou, X. Xi, and Z.-K. Liu, "Thermodynamic reactivity of the magnesium vapor with substrate materials during MgB$_2$ deposition," *Physica C: Superconductivity*, vol. 397, no. 3-4, pp. 87–94, October 2003.

[174] H. Shibata, T. Maruyama, T. Akazaki, H. Takesue, T. Honjo, and Y. Tokura, "Photon detection and fabrication of MgB$_2$ nanowire," *Physica C: Superconductivity*, vol. 468, no. 15-20, pp. 1992–1994, September 2008.

[175] H. Shimakage, M. Tatsumi, and Z. Wang, "Ultrathin MgB$_2$ films fabricated by the co-evaporation method at high Mg evaporation rates," *Superconductor Science and Technology*, vol. 21, no. 9, p. 095009, July 2008.

[176] Y. Wang, C. Zhuang, X. Sun, X. Huang, Q. Fu, Z. Liao, D. Yu, and Q. Feng, "Ultrathin epitaxial MgB$_2$ superconducting films with high critical current density and T$_c$ above 33 K," *Superconductor Science and Technology*, vol. 22, no. 12, p. 125015, October 2009.

[177] C. Zhang, Y. Wang, D. Wang, Y. Zhang, Z.-H. Liu, Q.-R. Feng, and G. Z.-Z., "Suppression of superconductivity in epitaxial MgB$_2$ ultrathin films," *Journal of Applied Physics*, vol. 114, no. 2, p. 023903, July 2013.

[178] H. Shibata, T. Akazaki, and Y. Tokura, "Fabrication of MgB$_2$ Nanowire Single-Photon Detector with Meander Structure," *Applied Physics Express*, vol. 6, no. 2, p. 023101, February 2013.

[179] D. Cunnane, E. Galan, K. Chen, and X. X. Xi, "Planar-type MgB$_2$ SQUIDs utilizing a multilayer process," *Applied Physics Letters*, vol. 103, no. 21, p. 212603, November 2013.

[180] M. A. Wolak, N. Acharya, D. P. Cunnane, B. S. Karasik, and X. X. Xi, "Ultrathin MgB_2 films for hot electron bolometer mixers fabricated by HPCVD and ion milling," in *26th International Symposium on Space Terahertz Technology*, March 2015, pp. P–43.

[181] H. Shibata, T. Akazaki, and Y. Tokura, "Ultrathin MgB_2 films fabricated by molecular beam epitaxy and rapid annealing," *Superconductor Science and Technology*, vol. 26, no. 3, p. 035005, March 2013.

[182] C. G. Zhuang, S. Meng, C. Y. Zhang, Q. R. Feng, Z. Z. Gan, H. Yang, Y. Jia, H. H. Wen, and X. X. Xi, "Ultrahigh current-carrying capability in clean MgB_2 films," *Journal of Applied Physics*, vol. 104, no. 1, p. 013924, May 2008.

[183] M. Wolak, N. Acharya, T. Tan, D. Cunnane, B. Karasik, and X. Xi, "Fabrication and characterization of ultrathin MgB_2 films for hot-electron bolometer applications," *Applied Superconductivity, IEEE Transactions on*, vol. 25, no. 3, pp. 1–5, June 2015.

[184] N. Acharya, M. Wolak, T. Tan, N. Lee, A. Lang, M. Taheri, D. Cunnane, B. Karasik, and X. Xi, "MgB_2 ultrathin films fabricated by hybrid physical chemical vapor deposition and ion milling," *APL Materials*, vol. 4, no. 8, p. 086114, August 2016.

[185] N. Acharya, M. Wolak, T. Melbourne, D. Cunnane, B. Karasik, and X. Xi, "As-grown versus ion-milled MgB_2 ultrathin films for THz sensor applications," *IEEE Transactions on Applied Superconductivity*, vol. 27, no. 4, p. 2300304, June 2017.

[186] C. Zhuang, K. Chen, J. Redwing, Q. Li, and X. Xi, "Surface morphology and thickness dependence of the properties of MgB_2 thin films by hybrid physical-chemical vapor deposition," *Superconductor Science and Technology*, vol. 23, no. 5, p. 055004, April 2010.

[187] Y. Cui, J. Jones, A. Beckley, R. Donovan, D. Lishego, E. Maertz, A. Pogrebnyakov, P. Orgiani, J. Redwing, and X. Xi, "Degradation of MgB_2 thin films in water," *IEEE Transactions on Applied Superconductivity*, vol. 15, no. 2, pp. 224–227, June 2005.

[188] R. K. Singh, Y. Shen, R. Gandikota, J. M. Rowell, and N. Newman, "Effect of stoichiometry on oxygen incorporation in MgB_2 thin films," *Superconductor Science and Technology*, vol. 21, no. 1, p. 015018, January 2008.

[189] W. Mumford and E. Scheibe, *Noise performance factors in communication systems.*   Dedham, MA: Horizon House-Microwave, 1968.

[190] H. Callen and T. Welton, "Irreversibility and generalized noise," *Physical Review*, vol. 83, pp. 34–40, July 1951.

[191] G. Reppel and E. Saur, "Superconducting proximity effect of NbN," *Journal of Low Temperature Physics*, vol. 17, no. 3-4, pp. 287–293, November 1974.

[192] I. Mazin, O. Andersen, O. Jepsen, O. Dolgov, J. Kortus, A. Golubov, A. Kuz'menko, and D. M. van der, "Superconductivity in MgB$_2$: Clean or dirty?" *Physical Review Letters*, vol. 89, no. 10, p. 107002, September 2002.

[193] M. Putti, V. Braccini, E. Galleani, F. Napoli, I. Pallecchi, A. S. Siri, P. Manfrinetti, and A. Palenzona, "Two-band effects in the transport properties of MgB$_2$," *Superconductor Science and Technology*, vol. 16, no. 2, pp. 188–192, February 2003.

[194] J. H. Jung, K. W. Kim, H. J. Lee, M. W. Kim, T. W. Noh, W. N. Kang, H.-J. Kim, E.-M. Choi, C. U. Jung, and S.-I. Lee, "Far-infrared transmission studies of a c-axis-oriented superconducting MgB$_2$ thin film," *Phys. Rev. B*, vol. 65, p. 052413, January 2002.